Norwegian University
of Life Sciences

Master's Thesis 2023 30 ECTS
Faculty of Science and Technology

Investigations of Crustal Loading Effects on Vertical GPS Time Series in the Hardangervidda Region: A Comparative Analysis

Tobias Arnell
Department of Geomatics

Tobias Arnell

Investigations of Crustal Loading Effects on Vertical GPS Time Series in the Hardangervidda Region: A Comparative Analysis

Master's thesis in Geomatics

Supervisors: Kristian Breili and Halfdan Pascal Kierulf
May 2023

Norwegian University of Life Sciences
Faculty of Science and Technology
Department of Geomatics

Abstract

This master's thesis seeks to ascertain if the vertical seasonal variations observed at permanent GPS stations (PGS) can be attributed to mass load deformations. The study focuses on seven PGSs in or around a highland region in south Norway. The mass loads examined include hydrological loads in the region and those related to water level fluctuations in nearby reservoirs. The study compares and corrects the vertical positions of a PGS against modelled vertical deformation resulting from mass displacement. Common mode filtering is employed on the GPS time series to minimise network errors. The findings reveal no direct connection between vertical displacements and the modelled hydrological mass load, as they exhibit phase shifts. Adjusting the observed PGSs' time series for the local effect and implementing a common mode filtering will significantly diminish the seasonal signal, although not entirely. This implies that either an unmodelled deformation signal influences certain PGSs in the study area or that these PGSs are subject to a similar error. Additionally, the study demonstrates that nearby water reservoirs contribute to the seasonal variation to a limited extent and do not cause substantial deformation at an adjacent PGS, particularly in comparison with other hydrological deformations.

Preface

This thesis signifies the conclusion of my academic journey at the Norwegian University of Life Sciences, which has proven to be enlightening, engaging, and intriguing in equal measure. Above all, I have felt privileged to have had the opportunity to undertake this educational journey. My gratitude is particularly extended to the faculty within the Department of Geomatics. Their commitment to their respective fields, coupled with an ability to clarify even the most intricate subjects with remarkable ease, has played an instrumental role in this journey.

This thesis stands as a testament to the support and guidance I have received from numerous individuals to whom I owe a debt of gratitude. I sincerely appreciate my supervisors, Kristian Breili and Halfdan Pascal Kierulf. Their unwavering support, constructive advice, and encouragement have been invaluable. I am deeply indebted to Brian Bramanto for his assistance with the hydrological data from NVE. I also wish to express my gratitude to Oddvar Tangen at the NMA, who generously dedicated his time to acquaint me with the Bernese software and patiently addressed all my queries. My heartfelt thanks go to my parents, Kristina and Anders Arnell, for their linguistic support, which has undoubtedly enriched this thesis. Lastly, I must acknowledge the unending support from Anette Dale throughout this journey. Her constant encouragement has been a source of strength and motivation.

Oslo, 14 May 2023
Tobias Arnell

Contents

Abstract **i**

Preface **ii**

Contents **v**

List of Figures **v**

List of Tables **xi**

Abbreviations **xvii**

1 Introduction **1**

1.1 Background 1

1.2 Problem statement 3

1.3 Thesis structure 4

2 Theory **6**

2.1 Global Navigation Satellite System 6

2.2 Crustal deformation due to mass loading 12

2.3 Common Mode Error 19

2.4 The Hydrological model 21

3 Methodology and Data **22**

3.1 Software . . . 22

3.2 Permanent GNSS stations . . . 22

3.3 Time series . . . 22

3.4 Time series analysis . . . 25

3.5 Land Grid . . . 26

3.6 Acquiring hydrological data . . . 28

3.7 Water reservoirs . . . 29

3.8 Distance . . . 31

3.9 Earth model . . . 31

3.10 Elastic loading signals . . . 32

3.11 Common Mode filtering and removal of elastic loading signals . . . 33

4 Results and Interpretation **35**

4.1 Analysing the elastic loading signals . . . 35

4.2 Analysing the GPS time series . . . 43

4.3 Results on PGS . . . 64

4.4 Summary of results . . . 74

5 Discussion **76**

5.1 Loading models . . . 76

5.2 PGS Network . . . 77

5.3 GPS time series . . . 78

5.4 Common Mode filtering . . . 79

5.5 Further work . . . 80

6 Conclusions **82**

References **84**

Appendices: **88**

A **89**

B **93**

List of Figures

2.1 Multipath implies that the satellite signals take an indirect route as they bounce off surrounding surfaces, thus increasing the length of the path. Consequently, estimating the distance between the satellite and the receiver becomes inaccurate as the signal travels through multiple paths, arriving at different times and angles at the receiver. 11

2.2 The impact of elastic loading, which can cause displacement of a permanent GNSS station (red dot). The station remains stationary in the absence of a load signal, as shown in panel (a). However, panel (b) displays the impact of an elastic load signal on the station, leading to deformation and displacement in both vertical and horizontal directions. Finally, panel (c) demonstrates the dissipation of the load effect and the crust's immediate rebound, resulting in the station's return to its original position. 13

2.3 The figure illustrates the angular distances (ψ) between two designated points, (A) and (B), on the surface of a spherical earth. 15

3.1 The map displays the southern region of Norway and identifies the permanent GNSS stations selected for this study, particularly emphasising the station labelled as MAUC. The surrounding stations, represented by black dots, comprise the network that will serve as the foundation for computing the common mode error. 23

3.2 Missing observations for the permanent GNSS station MAUC 2010-2022. 24

3.3 Missing observations for the permanent GNSS station MAUC 2017-2022 and discrepancy in missing observations between the two processing software Bernese and Gamit/Globk. 25

3.4 The uncorrected height estimations obtained from Bernese. As depicted in the graph, a trend is present in the time series, and certain data points could be identified as outliers. 26

3.5 Similar as Fig. 3.4, but the height estimates have undergone detrending, outlier detection, and elimination of outliers. 26

3.6 Various grid cells adopted in this research. The grid cells within a range of approximately two kilometres from the stations and the surrounding area have a size of 100 x 100 meters. Conversely, the grid cells outside this region have a size of 1 x 1 kilometre. This approach aims to eliminate the load influence of the proximate grid cell to the PGS to avoid singularity but also enables to more accurate capture of local effects within a ca. two km from the PGS. (Topografisk Norgeskart gråtone, 2017) 27

3.7 The above images illustrate the process of determining the area of water reservoirs. The left image displays an aerial photograph capturing low water levels. The right image presents the photograph's interpretation, wherein the points represent the centre of 100 x 100-meter squares. Volume estimation is limited to low water level boundaries. (Norge i Bilder)(Topografisk Norgeskart gråtone, 2017) 30

3.8 Temporal volume changes in Sysenvatnet from 2017 to 2022 (NVE). . 30

3.9 Normalized surface vertical displacement PREM-model 32

4.1 Modelled deformation caused by snow load at the PGS MAUC from 2017 to 2022. 36

4.2 Modelled deformation caused by groundwater load at the PGS MAUC from 2017 to 2022. 37

4.3 Modelled deformation caused by soil moisture content load at the PGS MAUC during the period from 2017 to 2022. 37

4.4 The temporal volume changes in the Sysenvatnet from 2017 to 2022 (NVE). 38

4.5 The modelled deformation caused by Sysenvatnet load at the PGS MAUC during the period from 2017 to 2022 (NVE). 38

4.6 The total hydrological and water reservoir load at the PGS MAUC during the period from 2017 to 2022. (NVE) 38

4.7 The modelled deformation caused by the atmospheric load at the PGS MAUC during the period from 2017 to 2022. 39

4.8 The modelled deformation caused by the total hydrological, atmospherical and water reservoir load at the PGS MAUC during the period from 2017 to 2022. 39

4.9 GPS observations, the regression line, and the total elastic loading signal derived from the hydrological and the water reservoir loading. As seen in the graph, there is a phase shift between the elastic loading signal and the regression line of the GPS observations. 40

4.10 GPS observations, the regression line, and the total elastic loading signal derived from the hydrological, the atmospherical, and the water reservoir loading. As seen in the graph, there is a phase shift between the elastic loading signal and the regression line of the GPS observations. 40

4.11 GPS observations, the regression line, and the total elastic loading signal derived from the water reservoir loading. As seen in the graph, there is a phase shift between the elastic loading signal and the regression line of the GPS observations. 41

4.12 GPS observations, the regression line, and the seasonal smoothed regression line for the ATML. The graph shows that the seasonal smoothed regression line for the ATML corresponds well with the uplift of the GPS observations during the winter months. 41

4.13 The locations of the permanent GNSS PGSs that were utilized in this study. The locations of the PGSs are depicted as black dots on the map. (Topografisk Norgeskart gråtone, 2017) 42

4.14 The GPS observations at DGLS and the regression line. H_{GNSS} represents the unfiltered time series, whereas $H_{\mathrm{GNSS}} - L$ corresponds to the unfiltered time series with the loading effect subtracted. H_{CM} refers to the common mode-filtered time series based on H_{GNSS}, and $H_{\mathrm{CM,L}}$ refers to the common mode-filtered time series applied to $H_{\mathrm{GNSS}} - L$. 67

4.15 The GPS observations at HAUC and the regression line. H_{GNSS} represents the unfiltered time series, whereas $H_{\mathrm{GNSS}} - L$ corresponds to the unfiltered time series with the loading effect subtracted. H_{CM} refers to the common mode-filtered time series based on H_{GNSS}, and $H_{\mathrm{CM,L}}$ refers to the common mode-filtered time series applied to $H_{\mathrm{GNSS}} - L$. 68

4.16 The GPS observations at LOFT and the regression line. H_{GNSS} represents the unfiltered time series, whereas $H_{\mathrm{GNSS}} - L$ corresponds to the unfiltered time series with the loading effect subtracted. H_{CM} refers to the common mode-filtered time series based on H_{GNSS}, and $H_{\mathrm{CM,L}}$ refers to the common mode-filtered time series applied to $H_{\mathrm{GNSS}} - L$. 69

4.17 The GPS observations at OSTC and the regression line. H_{GNSS} represents the unfiltered time series, whereas $H_{\mathrm{GNSS}} - L$ corresponds to the unfiltered time series with the loading effect subtracted. H_{CM} refers to the common mode-filtered time series based on H_{GNSS}, and $H_{\mathrm{CM,L}}$ refers to the common mode-filtered time series applied to $H_{\mathrm{GNSS}} - L$. 70

4.18 The GPS observations at RAUC and the regression line. H_{GNSS} represents the unfiltered time series, whereas $H_{\mathrm{GNSS}} - L$ corresponds to the unfiltered time series with the loading effect subtracted. H_{CM} refers to the common mode-filtered time series based on H_{GNSS}, and $H_{\mathrm{CM,L}}$ refers to the common mode-filtered time series applied to $H_{\mathrm{GNSS}} - L$. 71

4.19 The GPS observations at VSSC and the regression line. H_{GNSS} represents the unfiltered time series, whereas $H_{\mathrm{GNSS}} - L$ corresponds to the unfiltered time series with the loading effect subtracted. H_{CM} refers to the common mode-filtered time series based on H_{GNSS}, and $H_{\mathrm{CM,L}}$ refers to the common mode-filtered time series applied to $H_{\mathrm{GNSS}} - L$. 72

4.20 The GPS observations at MAUC and the regression line. H_{GNSS} represents the unfiltered time series, whereas $H_{\mathrm{GNSS}} - L$ corresponds to the unfiltered time series with the loading effect subtracted. H_{CM} refers to the common mode-filtered time series based on H_{GNSS}, and $H_{\mathrm{CM,L}}$ refers to the common mode-filtered time series applied to $H_{\mathrm{GNSS}} - L$. 73

B1 The graphs show the modelled deformation effects for DGLS from above: SWE, GWT, SMC, Total hydrological deformation, and ATML. 94

B2 The graphs show the modelled deformation effects for DGLS from above: Total hydrological deformation + ATML; Total hydrological deformation together with GPS observations, and the regression line derived from the GPS observations; Total hydrological deformation + ATML together with GPS observations, and the regression line derived from the GPS observations; LWS GEOS-FPIT. 95

B3 The graphs show the modelled deformation effects for HAUC from above: SWE, GWT, SMC, Water reservoir, and Total hydrological deformation. 96

B4 The graphs show the modelled deformation effects for HAUC from above: ATML; Total hydrological deformation + ATML; Total hydrological deformation together with GPS observations, and the regression line derived from the GPS observations; Total hydrological deformation + ATML together with GPS observations, and the regression line derived from the GPS observations; LWS GEOS-FPIT. . 97

B5 The graphs show the modelled deformation effects for LOFT from above: SWE, GWT, SMC, Total hydrological deformation, and ATML. 98

B6 The graphs show the modelled deformation effects for LOFT from above: Total hydrological deformation + ATML; Total hydrological deformation together with GPS observations, and the regression line derived from the GPS observations; Total hydrological deformation + ATML together with GPS observations, and the regression line derived from the GPS observations; LWS GEOS-FPIT. 99

B7 The graphs show the modelled deformation effects for MAUC from above: SWE, GWT, SMC, Water reservoir, and Total hydrological deformation. 100

B8 The graphs show the modelled deformation effects for MAUC from above: ATML; Total hydrological deformation + ATML; Total hydrological deformation together with GPS observations, and the regression line derived from the GPS observations; Total hydrological deformation + ATML together with GPS observations, and the regression line derived from the GPS observations; LWS GEOS-FPIT. . 101

B9 The graphs show the modelled deformation effects for OSTC from above: SWE, GWT, SMC, Water reservoir, and Total hydrological deformation. 102

B10 The graphs show the modelled deformation effects for OSTC from above: ATML; Total hydrological deformation + ATML; Total hydrological deformation together with GPS observations, and the regression line derived from the GPS observations; Total hydrological deformation + ATML together with GPS observations, and the regression line derived from the GPS observations; LWS GEOS-FPIT. . 103

B11 The graphs show the modelled deformation effects for RAUC from above: SWE, GWT, SMC, Water reservoir, and Total hydrological deformation. 104

B12 The graphs show the modelled deformation effects for RAUC from above: ATML; Total hydrological deformation + ATML; Total hydrological deformation together with GPS observations, and the regression line derived from the GPS observations; Total hydrological deformation + ATML together with GPS observations, and the regression line derived from the GPS observations; LWS GEOS-FPIT. . 105

B13 The graphs show the modelled deformation effects for VSSC from above: SWE, GWT, SMC, Total hydrological deformation, and ATML.106

B14 The graphs show the modelled deformation effects for DGLS from above: Total hydrological deformation + ATML; Total hydrological deformation together with GPS observations, and the regression line derived from the GPS observations; Total hydrological deformation + ATML together with GPS observations, and the regression line derived from the GPS observations; LWS GEOS-FPIT. 107

List of Tables

2.1 UERE computation 9

3.1 Differences between the software Bernese and GAMIT/GLOBK. E represents the elevation angle. Lesser elevation angle represents that the software includes satellites closer to the horizon. 23

3.2 A table of PGSs that have water reservoirs in their proximity and the water reservoirs connected to each station. 29

4.1 The table shows the average relative values from Table 4.2. 45

4.2 The Bernese solution for all PGSs within the network, with L denoting the loading signal derived from hydrological and water reservoir loadings. Displayed are the annual RMSE, amplitude, and amplitude's standard deviation. The variations in RMSE and amplitude are relative to H_{GNSS}. H_{GNSS} represents the unfiltered time series, whereas $H_{\mathrm{GNSS}} - L$ corresponds to the unfiltered time series with the loading effect subtracted. H_{CM} refers to the common mode-filtered time series based on H_{GNSS}, and $H_{\mathrm{CM,L}}$ refers to the common mode-filtered time series applied to $H_{\mathrm{GNSS}} - L$. 46

4.3 The average relative values from Table 4.4. 47

4.4 The Bernese solution for all PGSs within the network, with L denoting the loading signal derived from water reservoir loadings. Displayed are the annual RMSE, amplitude, and amplitude's standard deviation. The variations in RMSE and amplitude are relative to H_{GNSS}. H_{GNSS} represents the unfiltered time series, whereas $H_{\mathrm{GNSS}} - L$ corresponds to the unfiltered time series with the loading effect subtracted. H_{CM} refers to the common mode-filtered time series based on H_{GNSS}, and $H_{\mathrm{CM,L}}$ refers to the common mode-filtered time series applied to $H_{\mathrm{GNSS}} - L$. 48

4.5 The average relative values from Table 4.6. 49

4.6 The Bernese solution for all PGSs within the network, with L denoting the loading signal derived from atmospheric, hydrological, and water reservoir loadings. Displayed are the annual RMSE, amplitude, and amplitude's standard deviation. The variations in RMSE and amplitude are relative to H_{GNSS}. H_{GNSS} represents the unfiltered time series, whereas $H_{\mathrm{GNSS}} - L$ corresponds to the unfiltered time series with the loading effect subtracted. H_{CM} refers to the common mode-filtered time series based on H_{GNSS}, and $H_{\mathrm{CM,L}}$ refers to the common mode-filtered time series applied to $H_{\mathrm{GNSS}} - L$. 50

4.7 The average relative values from Table 4.8. 51

4.8 The Bernese solution for all PGSs within the network, with L denoting the loading signal derived from atmospheric and water reservoir loadings. Displayed are the annual RMSE, amplitude, and amplitude's standard deviation. The variations in RMSE and amplitude are relative to H_{GNSS}. H_{GNSS} represents the unfiltered time series, whereas $H_{\mathrm{GNSS}} - L$ corresponds to the unfiltered time series with the loading effect subtracted. H_{CM} refers to the common mode-filtered time series based on H_{GNSS}, and $H_{\mathrm{CM,L}}$ refers to the common mode-filtered time series applied to $H_{\mathrm{GNSS}} - L$. 52

4.9 The table shows the average relative values from Table 4.10. 53

4.10 The Bernese solution for all PGSs within the network except the PGS DGLS, with L denoting the loading signal derived from hydrological and water reservoir loadings. Displayed are the annual RMSE, amplitude, and amplitude's standard deviation. The variations in RMSE and amplitude are relative to H_{GNSS}. H_{GNSS} represents the unfiltered time series, whereas $H_{\mathrm{GNSS}} - L$ corresponds to the unfiltered time series with the loading effect subtracted. H_{CM} refers to the common mode-filtered time series based on H_{GNSS}, and $H_{\mathrm{CM,L}}$ refers to the common mode-filtered time series applied to $H_{\mathrm{GNSS}} - L$. 54

4.11 The average relative values from Table 4.12. 55

4.12 The Bernese solution for all PGSs within the network except the PGS DGLS, with L denoting the loading signal derived from water reservoir loadings. Displayed are the annual RMSE, amplitude, and amplitude's standard deviation. The variations in RMSE and amplitude are relative to H_{GNSS}. H_{GNSS} represents the unfiltered time series, whereas $H_{\mathrm{GNSS}} - L$ corresponds to the unfiltered time series with the loading effect subtracted. H_{CM} refers to the common mode-filtered time series based on H_{GNSS}, and $H_{\mathrm{CM,L}}$ refers to the common mode-filtered time series applied to $H_{\mathrm{GNSS}} - L$. 56

4.13 The table shows the average relative values from Table 4.14. 57

4.14 The GAMIT/GLOBK solution for all PGSs within the network except the PGS DGLS, with L denoting the loading signal derived from hydrological and water reservoir loadings. Displayed are the annual RMSE, amplitude, and amplitude's standard deviation. The variations in RMSE and amplitude are relative to H_{GNSS}. H_{GNSS} represents the unfiltered time series, whereas $H_{\mathrm{GNSS}} - L$ corresponds to the unfiltered time series with the loading effect subtracted. H_{CM} refers to the common mode-filtered time series based on H_{GNSS}, and $H_{\mathrm{CM,L}}$ refers to the common mode-filtered time series applied to $H_{\mathrm{GNSS}} - L$. 58

4.15 The table shows the average relative values from Table 4.16. 59

4.16 The GAMIT/GLOBK solution for all PGSs within the network except the PGS DGLS, with L denoting the loading signal derived from water reservoir loadings. Displayed are the annual RMSE, amplitude, and amplitude's standard deviation. The variations in RMSE and amplitude are relative to H_{GNSS}. H_{GNSS} represents the unfiltered time series, whereas $H_{\mathrm{GNSS}} - L$ corresponds to the unfiltered time series with the loading effect subtracted. H_{CM} refers to the common mode-filtered time series based on H_{GNSS}, and $H_{\mathrm{CM,L}}$ refers to the common mode-filtered time series applied to $H_{\mathrm{GNSS}} - L$. 60

4.17 P-values for the Bernese, L1 solution are represented. 'True' signifies a value below 0.05, while 'False' signifies a value exceeding 0.05. "True" suggests a statistically significant disparity between the time series. . 61

4.18 Similar to Table 4.17, but for GAMIT, L1 62

4.19 The table provides a comparison of the solutions derived from different software, specifically concentrating on the PGS MAUC. The values presented are drawn from Tables 4.10 and 4.14. L denoting the loading signal derived from hydrological and water reservoir loadings. Displayed are the annual RMSE, amplitude, and amplitude's standard deviation. The variations in RMSE and amplitude are relative to H_{GNSS}. H_{GNSS} represents the unfiltered time series, whereas $H_{\mathrm{GNSS}} - L$ corresponds to the unfiltered time series with the loading effect subtracted. H_{CM} refers to the common mode-filtered time series based on H_{GNSS}, and $H_{\mathrm{CM,L}}$ refers to the common mode-filtered time series applied to $H_{\mathrm{GNSS}} - L$. 63

5.1 The Bernese solution for a network solution focused on the best possible solution for MAUC regarding reducing the amplitude, only including PGSs MAUC, DGLS, and OSTC. L denoting the loading signal derived from water reservoir loadings. Displayed are the annual RMSE, amplitude, and amplitude's standard deviation. The variations in RMSE and amplitude are relative to H_{GNSS}. H_{GNSS} represents the unfiltered time series, whereas $H_{\mathrm{GNSS}} - L$ corresponds to the unfiltered time series with the loading effect subtracted. H_{CM} refers to the common mode-filtered time series based on H_{GNSS}, and $H_{\mathrm{CM,L}}$ refers to the common mode-filtered time series applied to $H_{\mathrm{GNSS}} - L$. 78

5.2 A comparison between two GAMIT/GLOBK solutions processed either through an unweighted linear regression or the Hector software, with added white and flicker noise. H_{GNSS} represents unfiltered GPS time series, (WH) denotes White noise, and (FL) denotes Flicker noise. 79

A1 Love numbers, Loaded surfaces PREM Earth model. The table, derived from (Pagiatakis, 1990) 90

A2 Green's function for vertical displacement is presented in the table. The second column displays values from Pagiatakis (1990), while the third column exhibits values calculated for this thesis. The fourth column illustrates the differences between these values. All values have been normalised $G_{ur} * 10^{12}(R * \Psi)$, where Ψ is in radians. 91

Abbreviations

List of all abbreviations in alphabetic order:

- ATL: Atmospheric Tidal Loads
- ATML: Atmospheric Mass Loading
- CME: Common Mode Error
- DGLS: Dagali
- ECEF: Earth-centered, Earth-fixed
- GB: Guttenberg-Bullen
- GNNS: Global Navigation Satellite System
- GPS: Global Positioning System
- GWE: Groundwater Equivalent
- GWT: Groundwater Table
- HAUC: Haukeli
- HBV: Hydrologiska Byråns Vattenbalansavdelning
- HYDL: Hydrological Loading
- ICA: Independent Component Analysis
- LOFT: Lofthus

- MAUC: Maurset
- NMA: Norwegian Mapping Authority
- NTOL: Non-Tidal Ocean Loading
- NVE: The Norwegian Water Resources and Energy Directorate
- OSTC: Østerbø
- OTL: Ocean Tide Loads
- PCA: Principal Component Analysis
- PGS: Permanent GPS/GNSS station
- PPP: Precise Point Positioning
- PREM: Preliminary Reference Earth Model
- RAUC: Rauland
- RMSE: Root Mean Square Error
- RTK: Real-Time Kinematic
- SMC: Soil Moisture Content
- SWC: Soil Water Content
- SWE: Snow Water Equivalent
- UERE: User Equivalent Range Error
- VMF: Vienna Mapping Function
- VSSC: Voss
- WC: Water Column
- WRES: Water Reservoir
- WS: Water in the Soil

Chapter 1

Introduction

This thesis investigates if vertical displacements observed in time series from a permanent GNSS station (PGS) derive from deformations due to mass loads. It is written on behalf of the Norwegian Mapping Authority (NMA).

1.1 Background

The advent of global satellite navigation systems (GNSS) enables precise determination of a receiver's horizontal and vertical position. GNSS employs an Earth-Centered, Earth-Fixed (ECEF) coordinate system, a three-dimensional cartesian coordinate system originating at the earth's centre of mass. This type of reference frame makes it possible to monitor the earth's surface changes with exceptional precision.

With enhanced precision follows increased susceptibility to external factors, such as tidal forces and mass load deformations. Both phenomena are products of the crust of the earth being not solid but elastic. This means it can change shape due to external forces, whether gravitational forces from celestial bodies or mass changes on the surface. This responsiveness to external forces or mass changes means that the surface continuously changes shape, and due to the crust's elastic features, once the force dissipates, the surface instantaneously rebounds to its original state. Detecting such changes can be challenging or even impossible when all reference points are situated on the surface, as these deformations impact vast expanses of the surface. For instance, earth tides, which occur daily, have the potential to cause vertical deformations of up to 50 cm. These fluctuations are not discernible on the deformed

surface, given that all reference points experience the same deformation. Since GPS and other satellite-based navigation systems utilise an ECEF reference frame and operate with high precision, these effects are measurable. Effects like solid earth tides have to be corrected to give a precise receiver position. In addition to tidal effects, mass redistribution on the earth's surface causes load mass deformations. Compared to tidal effects, these are subtle and often amount to just up to a couple of centimetres. With their high precision and susceptibility, GNSS are a tool that can be used to observe geodynamic processes.

When utilising PGSs, these effects can often be observed in time series as noise, but if the mass load is substantial and related to seasonal changes, it can be in the form of periodic seasonal fluctuations. If the PGS is utilised to be part of the regional reference frame or a part of a navigation service like Real-Time Kinematic (RTK), these fluctuations can, in extreme instances, impact the reliability of the PGS. Some PGSs in Norway show this kind of behaviour, i.e. periodically fluctuating vertical positions. Especially PGSs near large water reservoirs have shown large annual variations in their vertical position. Are these fluctuations due to mass changes connected to the water level in the reservoirs, or are they induced by other hydrological loading effects like snow or groundwater variations? To determine if the mass load effect is causing the vertical displacement, the load effect of the water reservoir and other hydrological sources needs to be determined through the loading theory. The loading theory makes it possible to determine a mass's deformation effect on a position at a certain distance. So to determine the deformation effect at a point, two inputs are needed the mass in the area and the distance from the point of interest. This method of determining the deformation due to mass load was first introduced by Farrell (1972).

The practice of correcting GNSS time series for mass load deformations by modelling the load effects is not novel and has been previously explored by scholars such as van Dam and Wahr (1998) and Nordman et al. (2009). These investigations are primarily focused on extensive loading effects influencing vast areas, not minor local loading effects as seen with reservoirs. Consequently, this study draws its methodological approach from Kierulf et al. (2022), who demonstrated that merely assessing the impact of the mass load on the GNSS time series is insufficient, as the time series may be influenced by systematic errors stemming from inaccurate satellite orbit modelling, reference frames realisation, and modelling of atmospheric conditions. These systematic errors are consistent across all stations for a regional network, implying that similar errors are present at each station. By employing

common mode filtering, it is feasible to ascertain the magnitude of these errors and subsequently correct the observations accordingly. Thus, a common mode filtering is required to ascertain the impact of the local mass load deformations at a millimetre level.

1.2 Problem statement

One PGS exhibiting seasonal fluctuations is MAUC, located at Maurset in southwest Norway, a mere two kilometres from the Sysenvatnet reservoir. The question arises whether these fluctuations are associated with water level changes at Sysenvatnet or other hydrological shifts, or a combination of both.

Questions to be analysed:

- Do the elevation fluctuations at MAUC or other PGSs result from mass load deformation?
- How severe is the deformation of the mass loads related to water reservoirs, and should PGSs be located in the proximity of reservoirs, as Sysenvatnet?

To answer these questions, the GNSS time series from MAUC needs to be corrected for deformations due to mass load and common mode errors. The subsequent procedure was employed to establish this. GPS time series from MAUC and adjacent PGSs were obtained. These adjacent PGSs form the basis for determining the common mode error. To assert the study's validity, the time series are derived from two software packages for precise GPS analysis: Bernese and GAMIT/GLOBK. The GPS time series were delivered and processed by NMA. The only GNSS used in this thesis is GPS. This is because the current version of the software Bernese (version 5.2), which is used to determine the position of the PGSs, is only fully compatible with GPS and GLONASS (Dach et al., 2007, p. 20). Only a GPS solution is included due to computational intensity restrictions.

Hydrological data from the regional run-off model obtained from the Norwegian Water Resources and Energy Directorate (NVE) served as the basis for determining the hydrological mass load in a region representing the southern part of Norway, with a resolution of one square kilometre. The data regarding water reservoirs in the proximity of any PGSs included in the study was also obtained from NVE. The

modelled deformation effect due to hydrological and water reservoirs was determined by using Green's function for crust deformation (Farrell, 1972).

To correct GPS time series for mass load deformation and other error sources, the following procedure is employed:

- Detrend the time series and remove all outliers.
- Subtract the estimated loading effects from the filtered time series.
- Apply a common mode filter to the load-corrected time series.

These corrected time series are then compared with the outlier-free, detrended time series to assess whether the loading and common mode corrections enhance the time series, i.e., reduce scatter and the amplitude of the seasonal signal. The primary objective is to explore whether it is possible to determine if mass load deformations are the cause of the vertical fluctuations observed in certain PGSs or, if so, to what degree. This study examines the PGS MAUC and the PGSs nearby rather than a wider region. This approach is predicated on the fact that all the PGSs incorporated in the study necessitate the correction for the specific mass load they are subjected to. Given that determining the impact of the mass load is computationally intensive and thus time-consuming, a decision was made to confine the scope of the study to a limited geographical area. Moreover, this study primarily intends to ascertain if the mass fluctuations attributable to hydrological factors or water reservoirs can trigger vertical crustal deformations of the magnitude observed in the GPS time series. It does not seek to investigate other potential causes for these vertical displacements.

1.3 Thesis structure

This thesis is structured into six chapters, supplemented with an appendix for additional reference.

Chapter 2 lays the foundation for the thesis by providing an in-depth understanding of the core theoretical principles that underpin this thesis. This includes an explanation of the GNSS, an explanation of the loading theory, and an introduction to common mode filtering.

Chapter 3 delineates the methodological framework and the data sources employed

for this study. It details the approach undertaken to carry out the study, describing the processes and techniques used.

Chapter 4 delivers the findings, presenting a detailed account of the results. Additionally, it includes an interpretation of the results.

Chapter 5 critically evaluates the study's limitations and their impact on the study. This chapter also suggests potential further work.

Chapter 6 presents the conclusion.

The Appendix serves as a supplemental section, providing additional material and resources.

Chapter 2

Theory

2.1 Global Navigation Satellite System

Satellite-based positioning implies that satellites orbiting the earth work as reference points that send out signals with certain intervals, thus making it possible to determine the receiver's position by intercepting this signal. The four global satellite-based positioning systems in use as of 2023 are GPS, GLONASS, Galileo and BeiDou, collectively known as Global Navigations Satellite Systems (GNSS). The GNSS term thus describes all four individual systems. This subchapter will describe the primary approach of determining the receiver's position by satellites as reference points, discuss the different ways to interpret the signal, biases and error sources, and ways to avoid or reduce the impact of bias or uncertainties.

2.1.1 The basic concept of satellite-based positioning

The fundamentals of determining the receiver's position are that the receiver picks up the signals sent by visible GNSS satellites and establishes the rough distance between the receiver and the satellites by interpreting the time difference from the transmitted to the received signal. The signal also incorporates a broadcast message that includes the ephemeris parameters, i.e., information about the satellite's position at a specific time - allowing the receiver to compute the geocentric coordinates of the satellite. The time difference multiplied by the speed of light between the transmitted and the received signal determines the distance between the satellite and the receiver. Trilateration can then be employed to determine the position of a receiver

once the distance between the receiver and the satellites has been established and the positions of the satellites are known. At least four satellites are needed to determine a single point due to the receiver's inherent clock error, which means there are four unknown factors to be determined, the receiver's coordinates (X, Y, Z) and the clock error. Due to the receiver's inherent clock error, the time difference between the transmitted and the received signal must be estimated, which means that it is not a true range determination but a so-called pseudo-range. (Hofmann-Wellenhof et al., 2007, p. 4)

2.1.2 Global Positioning System

The Global Positioning System (GPS) is the most popular and oldest GNSS service. Currently (10/4/2023), it includes 31 satellites orbiting the earth, with 24 satellites being operational at all times. These satellites circle the earth at an altitude of 20200 km and complete one orbit every 11 hours and 58 minutes. The orbital planes are inclined at an angle of 55 degrees to the equator to guarantee global coverage. The satellites transmit signals on three different frequencies L1, L2 and L5; on these signals, there is modulated information (code observations). The modulated code on the carrier signal delivers information to the receiver about the satellite, which makes it possible to determine the following:

- The identification of the satellite
- Timestamp for transmission to derive the transit time
- The satellite's position, i.e. the ephemeris

2.1.3 Code and phase observations

There are two main ways to determine the range measurements between the satellite and the receiver, either with code or phase observations. Determining distance with code observations is the original idea behind GPS and follows the concept described above in the text. In this technique, the signal transmitted from the satellite will have modulated information about the signal as a code. In the receiver, a similar code is generated simultaneously, and thus the time difference between the transmitted and received code can be easily determined by how long it took since the

receiver generated the same signal. In order to ensure successful positioning, synchronisation of the clocks in both the satellite and the receiver is necessary. However, any discrepancies in time can be estimated by utilising additional observations, as described previously (Hofmann-Wellenhof et al., 2007, p. 105).

Phase observations also compare the received signal to the generated signal, but instead of comparing the coded segment, it measures the difference in the phase between the transmitted and the generated carrier wave. The distance is determined by how many whole periods and parts of a period there are between the receiver and the satellite. Since the number of whole wavelengths is unknown at the initialisation of the measurement, it takes some time to resolve this phase ambiguity. It is also crucial to correctly determine the phase ambiguity; otherwise, the distance will be incorrect by an integer number of wavelengths. Another problem with phase observations is that they require that the signal between the receiver and the satellite is continuously observed, i.e. if the signal is lost, a cycle slip will occur, and the phase ambiguity must be solved again (Hofmann-Wellenhof et al., 2007, p. 106).

The disparity in range precision between code and phase observations can be elucidated by examining the difference in signal frequency. From the L1 band in GPS, the modulated C/A code observation has a frequency of 1.023 megachips per second, while the carrier phase observation has a frequency of 1575.42 MHz. Since the wavelength of the signals travels at the speed of light, approximately 300 000 000 m/s, the signals' wavelengths are approximately 300 m and 0.2 m respectively. The signal resolution, typically around one per cent of the wavelength, is a guideline for estimating the accuracy of a range measurement and theoretically achieving a precision of approximately three meters for the code observation and two millimetres for the phase observations. (Lantmäteriet, 2023)

2.1.4 Error sources and biases

All observations, either code or phase, are affected by biases and noise that decrease the precision of the measurement. As seen in Table 2.1, from Hofmann-Wellenhof et al. (2007, p. 111), the user equivalent range error (UERE) describes the impact of different sources on the GNSS observation's precision. The major contributors to this range error are the delay introduced by the ionosphere and bias introduced by the satellite clock, and incorrect data about the satellite's orbit, i.e. that the ephemerides are wrong. These three factors seem to be the main culprits, but

they are not as influential as they seem, and there are several ways to reduce their impact. However, the biases introduced by tropospheric delay and multipath are much harder to redeem.

Table 2.1: UERE computation

Error source	Bias (m)	Random (m)	Total (m)
Ephemerides data	2.1	0.0	2.1
Satellite clock	2.0	0.7	2.1
Ionosphere	4.0	0.5	4.0
Troposphere	0.5	0.5	0.7
Multipath	1.0	1.0	1.4
Receiver measurement	0.5	0.2	0.5
UERE (m)	5.1	1.4	5.3

2.1.5 Ionospheric delay

The ionospheric delay occurs when the signal from a satellite is refracted as it passes through the ionosphere, which is the uppermost layer of the earth's atmosphere. The ionosphere consists of ionised gas containing free particles, mainly electrons, and is situated at an altitude of 50 to 1000 km above sea level. The concentration of these free particles in the ionosphere fluctuates with seasonal changes and time of day and is also linked to solar activity. The presence of free particles in the ionosphere can interfere with satellite signals and cause errors in range estimation. However, the ionosphere is a dispersive medium, meaning it refracts different frequencies differently. By using signals of multiple frequencies, the delay caused by the ionosphere can be circumvented by applying a linear combination. It is important to note that this technique requires the receiver to be capable of receiving multiple frequencies. If not, the ionospheric effect must be modelled to obtain accurate range estimates (Hofmann-Wellenhof et al., 2007, pp. 122–127).

2.1.6 Tropospheric delay

The troposphere, which extends from the ground level up to approximately 50 km above the sea level, is the lower part of the atmosphere. Contrary to the ionosphere, it is not a dispersive medium to the frequencies used by GNSS, so the delay caused by the troposphere has to be modelled. The troposphere comprises two primary layers: the dry upper layer and the lower wet layer. Most of the delay is attributed

to the dry upper layer, accounting for roughly 90% of the total delay. This layer can be reasonably easily modelled, as the delay depends on the region's atmospheric pressure. In contrast, modelling the lower wet layer is more challenging, as the delay is mainly caused by water vapour, which can vary greatly. Several models are available to determine tropospheric delay, but the Vienna Mapping Function (VMF) is the model utilised in this thesis (Hofmann-Wellenhof et al., 2007, p. 65).

2.1.7 Satellite clocks and ephemerides

With an orbital velocity of around four kilometres per second, minor discrepancies in the timestamp or positioning of the satellite will result in significant deviations in the estimated receiver position. A satellite clock error occurs when the onboard clock is not correctly synchronised with the official GPS time. The ephemerides provide ideal information about the satellite's position, but several factors, such as direct solar radiation, may impact the satellite's orbital plane, putting it slightly off course. Ways to redeem or minimise both satellite clock and ephemeride errors are either by obtaining corrected data post-process or by relative positioning (Hofmann-Wellenhof et al., 2007).

2.1.8 Multipath

Multipath occurs when the transmitted satellite signal arrives at the receiver from more than one direction, i.e. it reflects on nearby surfaces and thereby, the range becomes longer. Figure 2.1 shows that the indirect paths are longer than the direct path. The main objects that cause this are buildings, trees, water surfaces, snow, and ground. The effects of multipath vary from around 15 m to less than a centimetre, depending on the type of observation used. The impact is drastically lesser on phase observations than on code observations. The ways to minimise the risk of multipath contamination is to ensure that the GNSS antenna is on an open area far from reflective surfaces and not using low-elevation satellites due to the higher likelihood of interference. The effect is often less for long-term static measurements due to the change of satellite geometry over time (Hofmann-Wellenhof et al., 2007, p. 155).

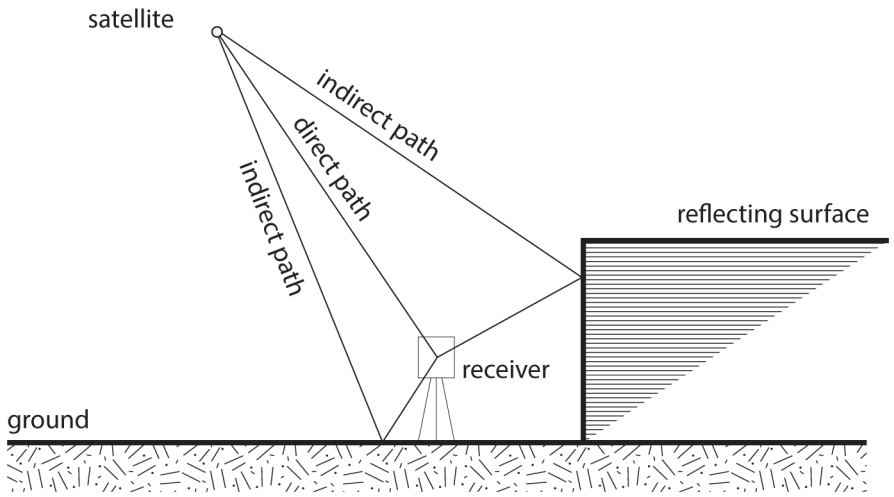

Figure 2.1: Multipath implies that the satellite signals take an indirect route as they bounce off surrounding surfaces, thus increasing the length of the path. Consequently, estimating the distance between the satellite and the receiver becomes inaccurate as the signal travels through multiple paths, arriving at different times and angles at the receiver.

2.1.9 Relative positioning

Relative positioning is a technique that can help circumvent, eliminate or minimise biases. To use this technique, at least two receivers should observe the same satellites simultaneously, with one at known coordinates and the other at unknown coordinates. This makes it possible to determine the position of an unknown point relative to a known point. The vector between the receivers is referred to as a baseline, and the relative measurement means that only the difference in coordinates between the two points is determined, not the absolute position of the point. The advantage of relative positioning is that many biases affecting both receivers will be minimised or eliminated by differencing the observation from one point to the other. Using a double-difference solution, it is possible to eliminate the clock bias in both the satellite and the receiver and significantly reduce the effects of the ionospheric and tropospheric delays. However, the amount of reduction in atmospheric delay depends on the length of the baseline. Shorter baselines will provide more reduction because the atmospheric conditions of the receivers will be more similar. For longer baselines, combining relative positioning with methods, such as linear combinations and models, can help reduce the impact of atmospheric delay. (Hofmann-Wellenhof et al., 2007)

2.2 Crustal deformation due to mass loading

The earth's crust is not a static structure. Instead, it is dynamic, responsive and can deform and adjust to various mass changes. Mass loadings are changes in the distribution of mass or pressure on the earth's surface, which can occur due to factors such as ocean tides, atmospheric pressure, hydrological effects, melting glaciers or changing water levels at reservoirs. The deformation of the earth's crust due to mass loadings is either elastic or viscoelastic. The former occurs when the earth's crust responds to a mass loading by deforming instantaneously and returning to its original shape once the load is removed, as shown in Fig. 2.2. Viscoelastic deformation will not rebound instantaneously (Torge & Müller, 2012). This is because viscoelastic deformation transpires over extended periods, as exemplified by the ice sheets during the last ice age. This long-lasting mass deformation displaces the underlying mantle material, which flows away from the area, thus creating a deformation. When the weight of the ice sheets disappears, the mantle slowly flows back into the space previously occupied by the deformation, allowing the crust to rise. The rebound from this deformation persists to the present day. In this thesis, only the effects of elastic deformations will be discussed. Elastic deformations, induced by mass loadings, are typically subtly, exhibiting variations from a few millimetres up to several centimetres (van Dam & Wahr, 1998). Such deformations predominantly significantly affect the vertical orientation, yet they also influence a point's horizontal position.

Before the publication of Farrell's paper, "Deformation of the Earth by Surface Loads," in 1972, no established method existed to precisely determine the impact of surface deformation attributable to mass changes. Farrell introduced a strategy for estimating this effect, employing elastic Green's functions. By combining these functions with the "mass-load Love number" and the distance to the load, Farrell demonstrated how one might accurately ascertain the extent of surface deformation caused by a given mass. Here, a Green's function is a sum of the mass-load Love numbers. The distance, in the form of Legendre polynomes, acts as weights to the load Love numbers.

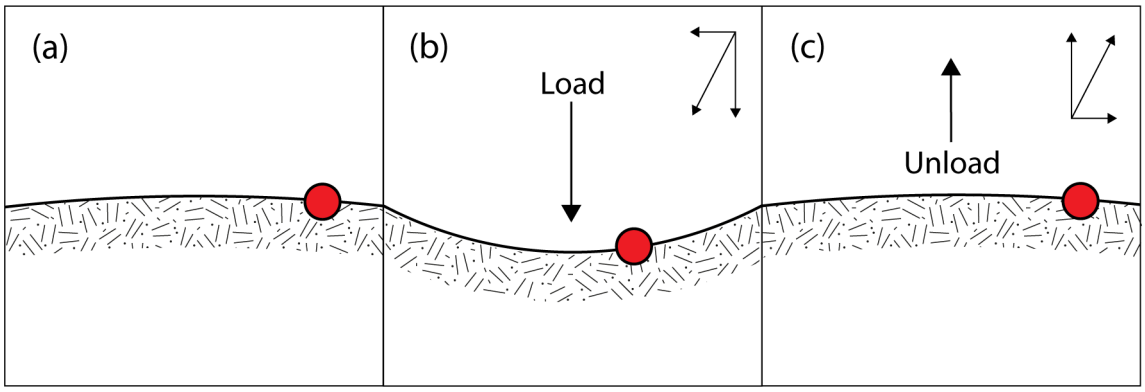

Figure 2.2: The impact of elastic loading, which can cause displacement of a permanent GNSS station (red dot). The station remains stationary in the absence of a load signal, as shown in panel (a). However, panel (b) displays the impact of an elastic load signal on the station, leading to deformation and displacement in both vertical and horizontal directions. Finally, panel (c) demonstrates the dissipation of the load effect and the crust's immediate rebound, resulting in the station's return to its original position.

Different types of mass loading

As previously mentioned, there are various ways in which mass loading can affect the earth's surface. This section will briefly review the different types of mass loading phenomena that can result in observable changes in measurements obtained from satellite positioning or gravity sensors.

Tidal loadings

The gravitational pull of celestial bodies, mainly the Sun and the Moon, causes mass distribution changes in the oceans and the atmosphere (Torge & Müller, 2012, p. 375). Since mass redistribution is constantly changing, this deforms the crust. Above all, ocean tide loads (OTL) are prominent and can deform the earth's crust several centimetres (Pagiatakis et al., 1982, p. 2); the effect is much less impactful in the case of atmospheric tidal loads (ATL), and it can have a maximum effect of 1.5 millimetres at the equator (Dach et al., 2007, p. 243). It is important to distinguish between tidal mass loadings and solid earth tides, where the latter is not considered a mass load effect. Solid earth tides are the deformation of the body of the earth due to celestial attraction. As will be discussed later in the subchapter about Love numbers, this effect cannot be modelled by mass Love numbers, but with Love numbers and solid earth tides are not considered a surface load.

Atmospheric loading

Atmospheric mass loading (ATML) is the deformation caused by the weight of the atmosphere on the earth's surface. The atmosphere has a mass, and as it moves around, it exerts pressure on the surface, causing it to deform. That this phe-

nomenon could cause crust deformations in the order of magnitude of several centimetres was first discovered in the late 19th century by Darwin (1882) (Petrov & Boy, 2004).

Non-tidal ocean loading
Non-tidal ocean loading (NTOL) refers to the distribution of seawater masses that are influenced by processes other than tidal effects. These processes include ocean currents and weather patterns. NTOL is closely linked to atmospheric loading (ATML). In coastal regions, the effect of NTOL can be comparable in magnitude to that of ATML (Williams & Penna, 2011).

Hydrological loading
Hydrological loading (HYDL) is a term used to describe the alterations in mass caused by changes in the quantity of water that is stored in different land areas. This includes water stored in various forms such as snow, soil and groundwater, lakes and rivers. The changes in mass resulting from these hydrological processes can lead to vertical displacements of several centimetres (van Dam et al., 2001)

2.2.1 Load Love Numbers

Love numbers (h and l) and Shida numbers (k) are coefficients that describe the earth's elasticity in response to the gravitational pull of celestial bodies, predominantly the Sun and the Moon. However, these Love numbers are insufficient to predict how a mass placed on the surface of the earth will deform the earth's crust. A variant known as the "mass-load Love number" was introduced to address this. Consequently, while Love numbers reflect the earth's elasticity under the influence of celestial gravitational forces, mass-load Love numbers dictate how a surface mass will cause crust deformation. To distinguish between the two, the mass-load Love numbers are represented with an appended prime number symbol (h', l', and k') and will henceforth be referred to as load Love numbers.

These load Love numbers are derived from seismological data describing the earth's density, structures, and elastic properties (Bos & Scherneck, 2013). In order to accurately determine the deformation effect of a mass load on the earth's surface, it is necessary to employ load Love numbers up to n=10000 (Farrell, 1972).

The Love numbers are used in Green's function and describe how a unit mass at the earth's surface affects a point at a spherical distance. Load Love numbers are derived for various earth models such as the Gutenberg-Bullen (GB) model (Farrell,

1972) or the Preliminary Reference Earth Model (PREM) (Dziewonski & Anderson, 1981).

2.2.2 Green's functions

Green's functions determine the deformation effect of a mass load on a spherical earth's surface at a specific angular distance, as depicted in Fig. 2.3. There are six different Green's functions that can be categorized into three distinct groups.

1. Displacement: Vertical and horizontal
2. Acceleration: Vertical and horizontal
3. The strain tensor components

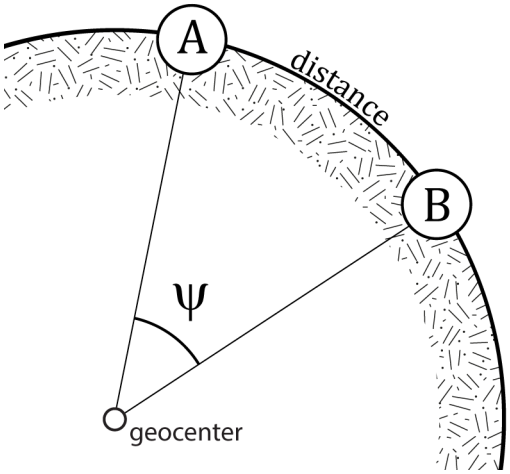

Figure 2.3: The figure illustrates the angular distances (ψ) between two designated points, (A) and (B), on the surface of a spherical earth.

2.2.3 Derivation of Green's function of vertical displacement

The load Love number and gravitational potential (W) caused by a mass load, as described by Jentzsch (1997), are connected to the vertical, horizontal, and potential deformations.

$$\begin{bmatrix} U_n \\ V_n \\ \Phi_n \end{bmatrix} = W_n \begin{bmatrix} \frac{h_n^{'}}{g} \\ \frac{l_n^{'}}{g} \\ k_n^{'} \end{bmatrix} \tag{2.1}$$

Where U_n, V_n and Φ_n are the vertical, horizontal, and potential deformations. W_n is the gravitational potential caused by the mass load, and g is the gravitational acceleration.

Green's function for vertical displacement can be expressed as:

$$U = \sum_{n=0}^{\infty} U_n P_n(\cos\psi) \tag{2.2}$$

As seen in Eq. 2.1 the n-th degree vertical displacement can be expressed as:

$$U_n = W_n \frac{h_n^{'}}{g} \tag{2.3}$$

Green's function for vertical displacement can now be expressed as:

$$U = \sum_{n=0}^{\infty} W_n \frac{h_n^{'}}{g} P_n(\cos\psi) \tag{2.4}$$

Gravitational potential caused by the mass load:

$$W = \frac{Gm}{d} \tag{2.5}$$

Here, G is the Gravitational constant, m is the load of the mass (with a value of 1 kg), and d is the distance between the mass and the observation point.

The distance between two points on a sphere can be expressed with spherical harmonics (Hofmann-Wellenhof & Moritz, 2006):

$$\frac{1}{d} = \sum_{n=0}^{\infty} \frac{r^{'n}}{r^{n+1}} P_n(\cos\psi) \tag{2.6}$$

Since at the earth's surface $r^{'} = r = R$ the function can be rewritten as:

$$\frac{1}{d} = \sum_{n=0}^{\infty} \frac{1}{R} P_n(\cos\psi) \tag{2.7}$$

Gravitational acceleration:

$$g = \frac{Gmm_e}{R^2} \tag{2.8}$$

In Eq. 2.8 m_e = earth's mass. With the assumption that $m = 1$ kg Eq. 2.8 can be rearranged as:

$$G = \frac{gR^2}{m_e} \tag{2.9}$$

Substituting Eq. 2.6 and Eq. 2.8 into Eq. 2.5 enables the derivation of an expression for the n-th gravitational potential, which can be represented as follows:

$$W = \sum_{n=0}^{\infty} W_n P_n(\cos\psi) = \frac{gR^2}{m_e} \sum_{n=0}^{\infty} \frac{1}{R} P_n(\cos\psi) \tag{2.10}$$

The n-th gravitational potential:

$$W_n = \frac{gR}{m_e} \tag{2.11}$$

Substitute Eq. 2.11 into Eq. 2.4 derives the expression representing the total deformation:

$$U = \sum_{n=0}^{\infty} W_n \frac{h_n^{'}}{g} P_n(\cos\psi) = \sum_{n=0}^{\infty} \frac{gR}{m_e} \frac{h_n^{'}}{g} P_n(\cos\psi) = \frac{R}{m_e} \sum_{n=0}^{\infty} h_n^{'} P_n(\cos\psi) \tag{2.12}$$

Green's function for vertical displacement at a spherical distance ψ:

$$u(\psi) = \frac{R}{m_e} \sum_{n=0}^{\infty} h_n^{'} P_n(\cos\psi) \tag{2.13}$$

As illustrated in Equation 2.13, the deformation effect at a distance ψ can be characterised as the infinite summation of load coefficients, each being multiplied by their corresponding Legendre polynomial. Notably, with an increase in the degree n, the

Love numbers tend towards a constant, as indicated in Equation 2.14. Thus, conducting computations with n=10000 is deemed appropriate for achieving sufficient precision.

$$\lim_{n\to\infty} \begin{bmatrix} h_n^{'} \\ nl_n^{'} \\ nk_n^{'} \end{bmatrix} = \begin{bmatrix} h_\infty^{'} \\ l_\infty^{'} \\ k_\infty^{'} \end{bmatrix} \tag{2.14}$$

When using a value for $h_n^{'}$ that approaches a limit, Eq. 2.13 can be rewritten as Kummer's transformation:

$$u(\psi) = \frac{Rh_\infty^{'}}{m_e} \sum_{n=0}^{\infty} P_n(\cos\psi) + \frac{R}{m_e} \sum_{n=0}^{\infty} (h_n^{'} - h_\infty^{'}) P_n(\cos\psi) \tag{2.15}$$

The first sum is well-known and can be rewritten as:

$$\frac{Rh_\infty^{'}}{m_e} \sum_{n=0}^{\infty} P_n(\cos\psi) = \frac{Rh_\infty^{'}}{2m_e \sin\frac{\psi}{2}} \tag{2.16}$$

This is because the infinite sum of this Legendre polynomial can be written as (Farrell, 1972):

$$\sum_{n=0}^{\infty} P_n(\cos\psi) = \frac{1}{2\sin\frac{\psi}{2}} \tag{2.17}$$

The Green's function for vertical displacement will end up looking like this:

$$u(\psi) = \frac{Rh_\infty^{'}}{2m_e \sin\frac{\psi}{2}} + \frac{R}{m_e} \sum_{n=0}^{\infty} (h_n^{'} - h_\infty^{'}) P_n(\cos\psi) \tag{2.18}$$

The Legendre polynomials are determined using the recursion formula described by Hofmann-Wellenhof and Moritz (2006, p. 15).

$$P_n(\cos\psi) = -\frac{n-1}{n} P_{n-2}(\cos\psi) + \frac{2n-1}{n} P_{n-1}(\cos\psi) \tag{2.19}$$

This implies that the calculation of P_2 exclusively necessitates the values from P_0 and P_1, while P_3 can be deduced utilising P_1 and P_2. Given that $P_0 = 1$ and

$P_1 = \cos\psi$, this methodology provides an efficient and sophisticated means for determining Legendre polynomials.

2.3 Common Mode Error

Common Mode Error (CME) refers to the systematic errors in the GNSS time series in the same regional network, i.e., all stations have similar observations, which means a similar error would be present at all stations. In short, the theory assumes that nearby or regional stations are affected by the same common mode error, which is spatially coherent. CME is among the most significant sources of error in the GNSS time series (White et al., 2022). The origin of CMEs is incorrect modelling of the ephemeris, the reference frame, and the atmosphere delay, but it can also be due to errors in the satellite's and the receiver's hardware or, most likely, a combination of all (Gruszczynski et al., 2016).

There are several different techniques to mitigate the effect of CMEs, some more elaborate than others; some common methods are; Stacking (Wdowinski et al., 1997), principal component analysis (PCA) (Dong et al., 2006), and independent component analysis (ICA) (Liu et al., 2015). Different methods have their advantages and disadvantages; for smaller networks where the CME is assumed to be uniform for all stations, the stacking method may be sufficient; on the other hand, for larger networks, methods such as PCA and ICA are more suitable. The advantage of the stacking method is the possibility of using incomplete data, while other methods require continuous data (Liu et al., 2015). The issue of missing data can be remedied through interpolation, although this approach may result in the introduction of some degree of uncertainty into the observations.

The stacking method advanced by Wdowinski et al. (1997) operates on the presumption that the common mode error remains consistent across the entire network for each epoch. This inherently implies that all observations for every station within the network are performed with equivalent accuracy. In response to this assumption, Nikolaidis (2002) proposed a weighting technique that assigns weights to each observation according to its standard deviation. Other alternative weighting strategies that could be utilised in stacking might include some form of distance weighting, such as inverse distance weighting.

Because the study's focus is confined to a relatively small research area, which is well within the bounds of the areas examined by Wdowinski et al. (1997) and Kierulf et al. (2022), both have successfully employed the stacking method, and given that the data set under examination features 5% missing observations, it was deemed appropriate to employ the stacking method for this study.

As the name suggests, the stacking method involves stacking multiple time series from nearby stations, aligning them in time, and computing the average signal. The common mode error can be estimated and removed by subtracting the average signal from the individual time series.

Determining the CME

Determine the Common Mode Error (CME) by the stacking technique, a simplified linear regression method, is used to find the best fit for detrended and demeaned time series data. Specifically, this involves calculating the residual ε for each epoch t and site s by comparing the observed position O to the predicted position C.

$$\varepsilon_s(t) = O_s(t) - C_s(t) \tag{2.20}$$

Stacking

Determine the CME ($\varepsilon(t)$) for each epoch; the values of $\varepsilon_s(t)$ obtained from all sites are averaged, resulting in a single value denoted as:

$$\hat{\varepsilon}(t) = \frac{\sum_{s=1}^{S} \varepsilon_s(t)}{S} \tag{2.21}$$

$S =$ represents the total number of sites

Filtering

After determining the CME, filtering can be applied to the observed data. The CME is subtracted from each site's observed position O to obtain the filtered position $\hat{O}$. This filtering process removes CME-related noise from the data, allowing for a more precise representation of the underlying signal.

$$\hat{O}_s(t) = O_s(t) - \hat{\varepsilon}(t) \tag{2.22}$$

2.4 The Hydrological model

The hydrological model estimates the water balance in a given region. This entails determining the amount of water stored at a specific location at a given time, including water that is either saturated in the ground, stored as groundwater, present in watercourses and lakes or present as snow. The water balance is estimated based on various factors, including precipitation, transportation, and evaporation. In Norway, a regional hydrological model has been developed by The Norwegian Water Resources and Energy Directorate (NVE) (Beldring et al., 2003) and builds upon the model of Hydrologiska Byråns Vattenbalansavdelning (HBV) model proposed by Bergström et al. (1995). The NVE model divides the land area into a grid with a resolution of one square kilometre. Each grid cell has unique characteristics, such as soil, vegetation, and sea-level altitude. The individual grid cells' water capacities are updated individually and daily based on their unique features and climate conditions. The model is composed of several components, including snow water equivalent (SWE), groundwater equivalent (GWE), and saturated water in the soil (WS).

The SWE component describes the water equivalent of the snowpack in millimetres, while the GWE component represents the total amount of water stored in the groundwater zone in millimetres.

The model does not provide the moisture content in the soil but instead provides the percentage of the simulated water content in the soil. To calculate the soil moisture content (SMC), the soil porosity ϕ and soil thickness d must be determined. Bramanto et al. (2022) suggested an approach to estimate soil moisture content (SMC) for the Norwegian hydrological model by utilizing a global dataset of soil thickness (Pelletier et al., 2016) and setting the general soil porosity to 30%. The soil thickness values can be obtained for the centre point of each grid cell using any GIS software. The SMC for each grid cell can be calculated by multiplying the fraction (WS), porosity(ϕ), and thickness (d).

$$SMC = WS \cdot \phi \cdot d \tag{2.23}$$

Chapter 3

Methodology and Data

3.1 Software

All calculations during the project were performed using Python (3.9.13) with the Spyder IDE (5.4.1) software. For geographic information analysis, the QGIS software (3.22.4) was utilised. Both Bernese (Dach et al., 2007) and Gamit/Globk (Herring et al., 2018) delivered the GPS solutions for the PGS.

3.2 Permanent GNSS stations

A CME analysis was required to evaluate the impact of local and regional mass loads on the Permanent GNSS station (PGS) at Maurset (MAUC). At least one additional PGS is necessary for a CME analysis, but preferably more. To ensure that the stations received as similar a signal as possible, all PGSs in the vicinity of the MAUC were considered. The PGSs with continuous observation during the selected period are Lofthus (LOFT), Voss (VSSC), Haukeli (HAUC), Østerbø (OSTC), Rauland (RAUC), and Dagali (DGLS), as shown in Fig. 3.1.

3.3 Time series

The time series for GPS utilised in this study were obtained from the computations made by the programs Bernese (Dach et al., 2007) and GAMIT/GLOBK (Herring et al., 2018). The processed time series was provided for this study by the NMA.

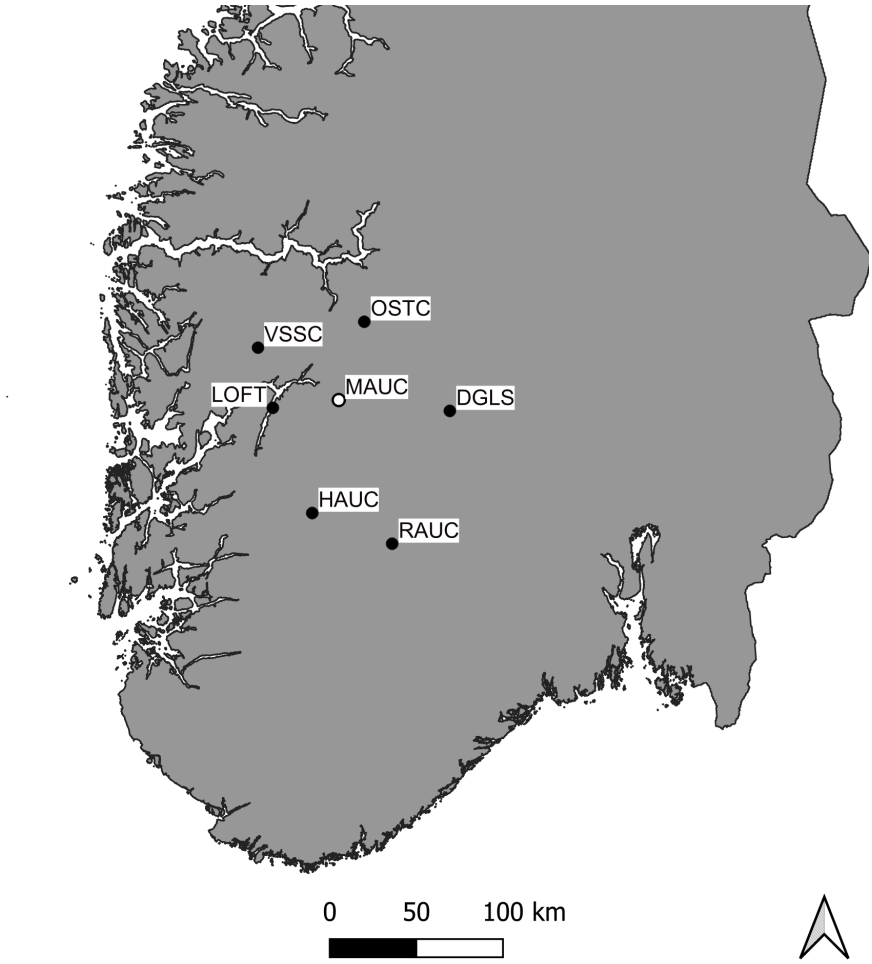

Figure 3.1: The map displays the southern region of Norway and identifies the permanent GNSS stations selected for this study, particularly emphasising the station labelled as MAUC. The surrounding stations, represented by black dots, comprise the network that will serve as the foundation for computing the common mode error.

Both programs determine the position of PGSs based on an ionospheric free relative positioning approach (described in Chapter 2). Both solutions use updated orbital corrections to improve the result further. As seen in Table 3.1, both programs deviate when it comes to if they are part of a global or regional solution and elevation angle. However, the result can be significantly different with the same data processed using various types of processing software (White et al., 2022).

Table 3.1: Differences between the software Bernese and GAMIT/GLOBK. E represents the elevation angle. Lesser elevation angle represents that the software includes satellites closer to the horizon.

Software	Elevation	Elevation-depending weighting	Solution
Bernese	3°	$\cos^2(E)$	Regional
GAMIT/GLOBK	10°	$\mathrm{a}^2 + \mathrm{b}^2/\sin^2(E)$	Global

The selected data used in this study comprises five years of continuous observations spanning from February 2017 to February 2022. The choice of this specific period is based on various limiting factors related to the dataset provided by Bernese. This is due to continuity regarding the data, where two events in the time series play a role.

First, the Bernese data underwent a transition from how to estimate the impact of the tropospheric delay in 2015, where the mapping function was changed from the Global Mapping Function to the Vienna Mapping Function.

Second, the Bernese data also transitioned regarding the reference frame, shifting from ITRF2008 to ITRF2014 on 31 January 2017.

To conduct an in-depth investigation, having the same reference frame and tropospheric mapping model is crucial. Consequently, the two time-period options are 2010-2015 or 2017-2022. As seen in Fig. 3.2, the two periods differ in the number of missing values. Even though the period from 2017 to 2022 contains more missing observations overall than the 2010-2015 period, it is worth noting that the missing observations during the latter period are not continuous, while the 33 days hiatus as seen in the year 2011 is. Due to these factors and the opportunity to evaluate current settings used in the software, the period between 2017 and 2022 was deemed more appropriate to analyse. The addition of analysing the same PGSs, where GAMIT/GLOBK established the observations, was a later edition and not a contributing factor to the chosen period. Fig. 3.3 reveals a discrepancy in missing observations between the two processing software, suggesting that different techniques were employed to determine if the daily solution were fit to remain in the dataset.

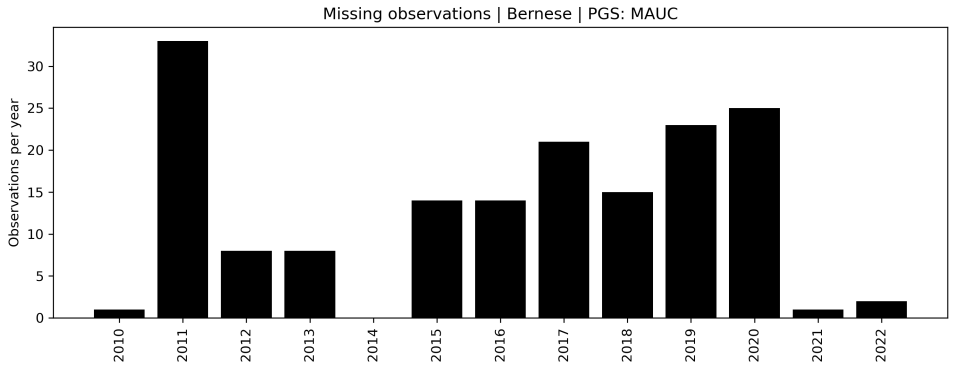

Figure 3.2: Missing observations for the permanent GNSS station MAUC 2010-2022.

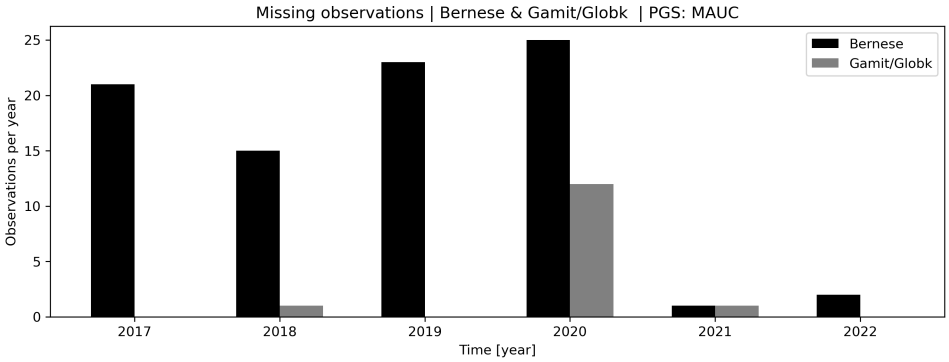

Figure 3.3: Missing observations for the permanent GNSS station MAUC 2017-2022 and discrepancy in missing observations between the two processing software Bernese and Gamit/Globk.

3.4 Time series analysis

For the time series analysis, the initial step involved filtering out the anomalous observations, i.e., outliers. Subsequently, a linear unweighted least squares regression model was employed to fit the observations, considering both annual and semiannual frequencies. Equation 3.1 represents this model:

$$\begin{aligned} h(t) &= a + bt + c\cos\omega t + d\sin\omega t + e\cos 2\omega t + f\sin 2\omega t \\ \omega &= \frac{2\pi}{365.25} \end{aligned} \tag{3.1}$$

The variable t denotes the duration of time measured in days. The unknown coefficients a and b correspond to the constant and linear trend. The variables c, d, e, and f represent the amplitude and phase of the annual and semiannual deformation. The standard deviation for the model was established by:

$$\begin{aligned} \sigma &= \sqrt{\frac{\sum(\epsilon^2)}{m-n}} \\ \varepsilon &= \text{Residuals} \\ m &= \text{Number of observations} \\ n &= \text{Number of unknowns} \end{aligned} \tag{3.2}$$

In order to detect and eliminate outliers, a standard threshold of three times the standard deviation was utilised. Subsequently, the time series were re-analysed by

fitting them to a linear regression model to remove the linear trend b. Figure 3.4 depicts the raw data, while Fig. 3.5 illustrates the processed data after removing the outliers without a trend present.

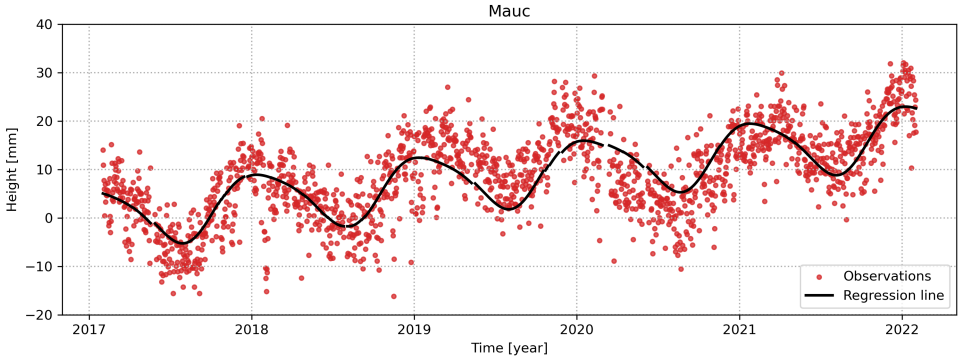

Figure 3.4: The uncorrected height estimations obtained from Bernese. As depicted in the graph, a trend is present in the time series, and certain data points could be identified as outliers.

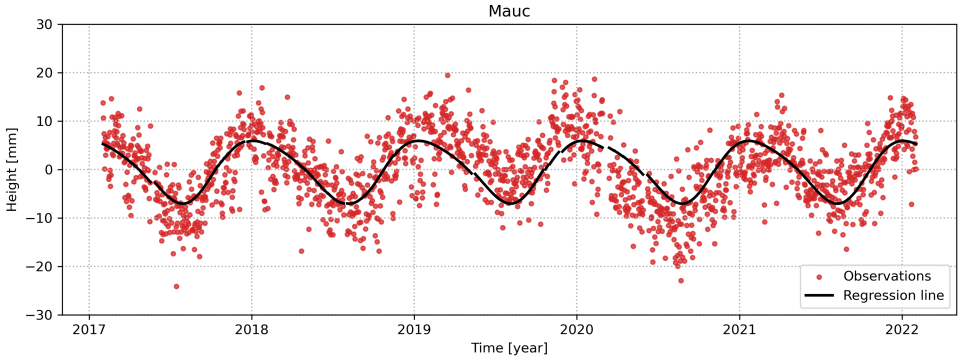

Figure 3.5: Similar as Fig. 3.4, but the height estimates have undergone detrending, outlier detection, and elimination of outliers.

3.5 Land Grid

To evaluate the amount of water stored in the land area, a grid with a size of one square kilometre was established. The grid cell size was selected to match the spatial resolution of NVE's hydrological model and was assigned UTM33N coordinates to align with NVE's grid data reference frame. However, the grids surrounding and containing the PGS had a higher resolution of 100 x 100 meters, as depicted in Fig. 3.6, to exclude the grid cell close to the PGS to avoid deviations in the calculated mass load due to singularity, and to capture local effects better. The centre points

with UTM33N coordinates from both grids were used to obtain data from NVE's API server.

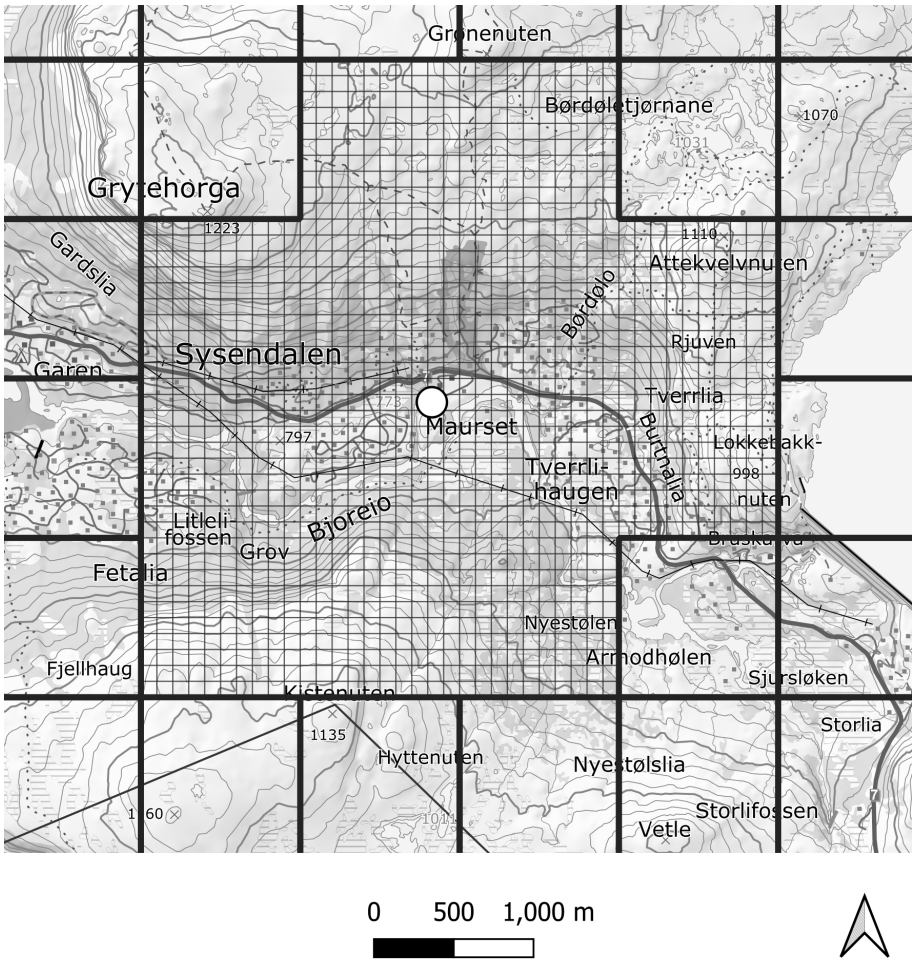

Figure 3.6: Various grid cells adopted in this research. The grid cells within a range of approximately two kilometres from the stations and the surrounding area have a size of 100 x 100 meters. Conversely, the grid cells outside this region have a size of 1 x 1 kilometre. This approach aims to eliminate the load influence of the proximate grid cell to the PGS to avoid singularity but also enables to more accurate capture of local effects within a ca. two km from the PGS. (Topografisk Norgeskart gråtone, 2017)

Additionally, the grid was used to collect soil depth data by integrating the global dataset from Pelletier et al. (2016). The mean soil depth in that area was extracted for each grid centre point.

The extent of the land grid is the southern part of Norway, including all land in a radius of 300 kilometres from an artificial centre point derived from the positions of the PGS used. The size restriction is based on two conditions. One is the availability of constant hydrological data based on the same conditions, i.e., not including data from the neighbouring country Sweden. Two, the assumption that the local effects

are the most prominent ones and that the mass loading effects from beyond the extent of the grid would affect the stations roughly the same, i.e., removed by common mode filtering.

3.6 Acquiring hydrological data

Access to hydrological data based on the local HBV model from the Norwegian Water Resources and Energy Directorate (NVE) for a specific location can be obtained through an API server provided by NVE, accessible via URL: http://api.nve.no/doc/gridtimeseries-data-gts/. This grid-based model has a resolution of one square kilometre and covers the entire Norwegian mainland. The only inputs required are the grid coordinates and the time period to obtain information about a specific feature during a period, such as the snow water equivalent (SWE).

Missing data and outliers were removed and replaced using linear interpolation to ensure data consistency. For prolonged periods of missing data, nearby observations from neighbouring grid cells were used for interpolation to ensure stability. Any grid cells with no data at all were excluded from the dataset. Two stages were utilised to detect outliers in the dataset. The first stage aimed to eliminate data points with unlikely or extreme values, while the second stage utilised a statistical approach whereby any values exceeding three times the standard deviation were removed. After removing the identified outliers, nan-values were replaced, and interpolation was subsequently carried out. To cater to the constraints of each layer in the dataset (i.e., SWE, groundwater equivalent (GWE), and water in the soil (WS)), a customised approach was adopted for each layer to prevent the elimination of valid data as outliers. A validation process was also implemented to ensure the highest accuracy level, where a subset of grid cells for each layer was randomly chosen and validated manually.

To estimate the land water storage mass impact of the PGSs, the required components, including SWE, GWE, and WS, were extracted from the API server. Since GWE represents the total amount of groundwater in the area, the mean was removed over a five-year period (2017-2022).

The mass for each grid cell was determined by multiplying the area (A) with the water column (WC) and the density (ρ) at each grid cell. The density of water was set to $1000\,\mathrm{kg/m^3}$, as seen in Eq. 3.4

$$\begin{aligned} \text{Mass} &= WC \cdot A \cdot \rho \\ WC &= \text{Water column} \\ A &= \text{Area} \\ \rho &= \text{Density} \end{aligned} \tag{3.3}$$

3.7 Water reservoirs

Certain PGSs are situated in close proximity or immediate vicinity to water reservoirs where the water level undergoes continual alterations. Given the resultant mass changes, deformation in the surrounding area will ensue, which must be modelled and incorporated into the system to account for the vertical shifts that may arise due to the water level fluctuations. A list of stations with water reservoirs that may impact the elevation of the stations by up to one-tenth of a millimetre is provided in Table 3.2.

Table 3.2: A table of PGSs that have water reservoirs in their proximity and the water reservoirs connected to each station.

Station	Water reservoir
HAUC	Brodalsvatn
	Kjelavatn
	Ståvatn
	Sognavatn
MAUC	Sysenvatnet
OSTC	Nyhellervatnet
RAUC	Møsvatn
	Totak

The area defining the water masses is divided into a grid to derive the effect of mass loading on the PGS imposed by these reservoirs. The reservoirs' water level and volume changes were derived from www.sildre.no, an NVE platform that delivers hydrological data. Inconsequvent data such as outliers and missing data were removed and interpolated using a linear technique.

There is uncertainty about how the reservoirs' area changes with the volume of water due to the absence of bathymetric maps. A flood chart would be ideal, but aerial photographs, as shown in Fig. 3.7, were used to determine the reservoirs' extent at their low water levels, i.e., by using aerial photos taken on corresponding dates

with low water levels in the data delivered by Sildre. In cases where aerial data was unavailable, a reduction of 100 meters was applied to the area to counter the uncertainty of water depth in shallow parts of the reservoir. This method ensures that the data used in the calculations are reliable and accurate, despite the absence of aerial information. The retracted area was subsequently used as the reference point for the analysis, and only changes in volume within this area were determined. This approach allows for the exclusion of shallow portions of the reservoir, which may cause significant uncertainties that could affect the final results.

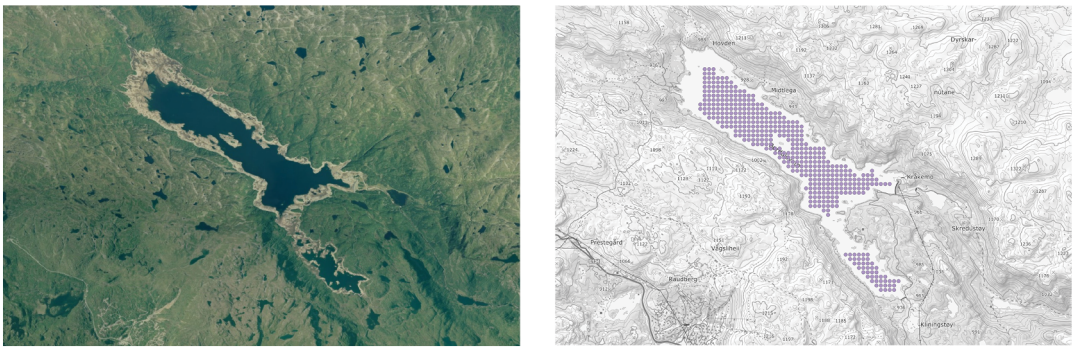

Figure 3.7: The above images illustrate the process of determining the area of water reservoirs. The left image displays an aerial photograph capturing low water levels. The right image presents the photograph's interpretation, wherein the points represent the centre of 100 x 100-meter squares. Volume estimation is limited to low water level boundaries. (Norge i Bilder)(Topografisk Norgeskart gråtone, 2017)

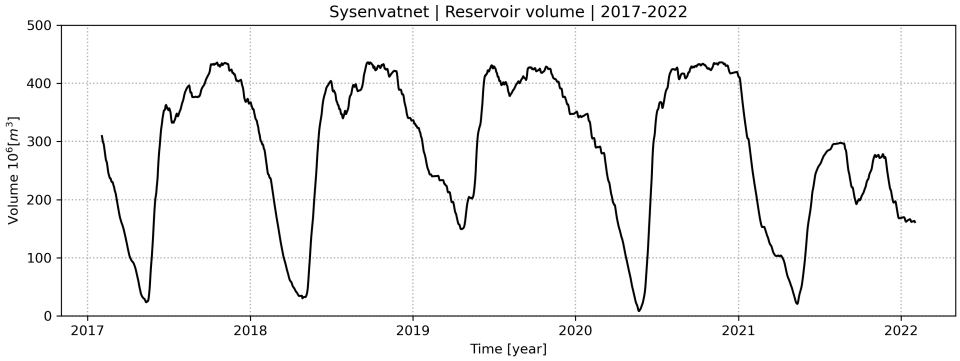

Figure 3.8: Temporal volume changes in Sysenvatnet from 2017 to 2022 (NVE).

Instead of using the measured water level, changes in volume were used to calculate the mass of the reservoir. Figure 3.8 presents an illustrative representation of the changes in the volume of a water reservoir. The volume within each grid cell was assumed to be uniformly distributed, meaning the volume was evenly dispersed across the area. This allowed for a more precise estimation of the reservoir's mass

without being affected by the coarseness of the grid. Additionally, using changes in volume instead of water level meant that uncertainties regarding the water depth in shallow areas did not have to be addressed. This simplified the analysis process and ensured that the final results were reliable.

3.8 Distance

In order to determine the distance between the PGS and each grid cell, they must be in the same reference frame. The grid cells' centre points are in UTM33N, while the base stations are in ITRF2014. Therefore, both datasets were transformed into ETRS89 with longitudinal and latitudinal coordinates. Since ETRS89 does not account for continental drift, the coordinates in the ITRF2014 dates were transformed using the last observation date, i.e., 2022-02-01. The transformation and ellipsoid distance were determined using Pyproj (PROJ contributors, 2023), a Python library. The mean earth radius between the two points was used to estimate the spherical distance as an angle (ψ).

$$\psi = \frac{\text{Distance} \cdot 180}{\text{R}_{\text{mean}} \cdot \Pi} \tag{3.4}$$

3.9 Earth model

As described in Chapter 2, the load Love number is derived from an earth model. This thesis uses load Love numbers derived from PREM. The Love numbers have been determined by Pagiatakis (1990). The tabulated values are represented in Table A1. Pagiatakis recommends either a linear or a cubic spline interpolation to interpolate between the tabulated values, as he provides only a few definite Love numbers (Pagiatakis, 1990, p. 553). This thesis used a cubic spline method for the best interpretation. To assess the calculated Love numbers, the vertical deformation of one kilogram at distances from 0°-180° was determined and compared with those computed by Pagiatakis, as shown in Table A2. The deviations of the results are subtle, and the values are consistent with those of Pagiatakis, as seen in Fig. 3.9.

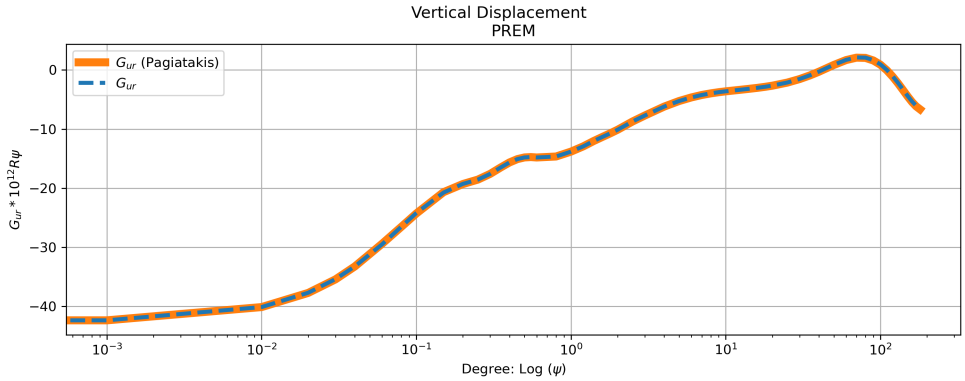

Figure 3.9: Normalized surface vertical displacement PREM-model

3.10 Elastic loading signals

The vertical displacement at the PGS sites caused by changes in water content was determined by first calculating the Green function for each grid cell. These were then scaled by the mass of each grid cell. Therefore, the total vertical deformation for all grid cells can be expressed as the sum.

$$\begin{aligned} I_{Site}(t) &= \sum_{j}^{J} G(\psi_j) O(\psi_j, t) \\ t &= \text{Epoch} \\ G(\psi_j) &= \text{The Green function for radial displacement} \\ O(\psi_j, t) &= \text{Mass in the grid cell during a specific time} \end{aligned} \tag{3.5}$$

Green's vertical deformation function was computed for each grid cell to estimate the elastic signal of each hydrological component, such as SWE, GWT, or SWC. The hydrological observation of each grid cell was then multiplied by the corresponding Green's function for the specific epoch to determine the elastic signal for that hydrological component. The same procedure was used to determine the deformations from the reservoir.

3.10.1 Atmospheric mass loading

The time series data obtained from the Bernese software do not include corrections for ATML; this was added to each station by requesting corrections from the International Mass Loading Service URL: http://massloading.net (Petrov, 2017). The

numerical weather model used where the GEOS-FPIT, which has a resolution of $0.50^\circ \times 0.625^\circ \times 72$ layers $\times$ 3 hours. The model is developed by Global Modeling and Assimilation Office at NASA Goddard Space Flight Center. An average of the eight calculated solutions per day was used to obtain a daily solution, which coincides with the epochs of the other datasets used in the analysis.

3.10.2 Total elastic loading signal

The total seasonal loading signal arising from the hydrological components, atmospheric loading, and neighbouring reservoirs can be denoted as:

$$H_L^i(t) = I_{SWE}^i(t) + I_{GWE}^i(t) + I_{SMC}^i(t) + I_{WR}^i(t) + I_{ATML}^i(t) \tag{3.6}$$

t = Epoch
$H_L^i(t)$ = Total estimated elastic loading signal applied to a specific PGS (i)
$I_{SWE}^i(t)$ = Radial displacement caused by snow
$I_{GWE}^i(t)$ = Radial displacement caused by groundwater
$I_{SMC}^i(t)$ = Radial displacement caused by soil moisture content
$I_{WR}^i(t)$ = Radial displacement caused by water reservoirs
$I_{ATML}^i(t)$ = Radial displacement caused by atmospheric mass loading

3.11 Common Mode filtering and removal of elastic loading signals

The elimination of the elastic loading signal and the application of common mode filtering are two separate steps. Firstly, the elastic loading signal is removed from the time series data. Secondly, the common mode filtering is applied to the residual data to further filter out any remaining noise. After removing the elastic loading signal, the time series can be represented as.

$$\begin{aligned} H_{GNSS,L}^i(t) &= H_{GNSS}^i(t) - H_L^i(t) \\ H_{GNSS} &= \text{Observed time series (PGS)} \end{aligned} \tag{3.7}$$

As described in Chapter 2, it is assumed that all stations in a regional network experience a similar signal, which results in a uniform impact on all stations. Removing this signal will reduce noise and the signal's annual amplitude. In order to remove the CME from the time series of a specific station, the CME signal is first calculated for all other stations within the network. Subsequently, this CME signal is subtracted from the time series of the targeted station to filter out the impact of CME.

$$\begin{aligned} H^i_{CM}(t) &= H^i_{GNSS}(t) - CM(t) \\ CM &= \text{Common Mode Error} \end{aligned} \tag{3.8}$$

The inclusion of regional loading signals in the common mode filtering is premised on the assumption that each PGS has a unique observable loading signal. Specifically, the local elastic signal has a discernible effect on the PGS height observation, owing to the distinct characteristics surrounding each PGS, such as variations in climate, elevation, and proximity to large water reservoirs. As a result, it is possible to represent the time series that has been filtered to remove common mode effects while taking into account the impact of the loading signal, as follows:

$$H^i_{CM,L}(t) = H^i_{GNSS,L}(t) - CM(t) \tag{3.9}$$

Chapter 4

Results and Interpretation

This chapter presents the study's findings and is divided into four parts. The first one will report the results of the estimated load signal, with a primary focus on the PGS located in Maurset (MAUC). The outcomes of the remaining PGSs will be accessible in the appendix. The second part will centre on the GNSS time series and present the outcomes linked to the subtraction of the estimated load signal and common mode filtering. Herein, the outcomes of all PGSs are exhibited, as the MAUC PGS is considered atypical. The results from the other PGSs are deemed significant since, in theory, their results should show better observation spread (RMSE) and annual amplitude size after the estimated load is subtracted and common filtering is applied. The third part will discuss the different PGS, focusing on visual inspection of the time series. The fourth part will be a summary of the results.

4.1 Analysing the elastic loading signals

The results will be visualised using a series of graphs showing the estimated load affecting PGS at MAUC. Load effects that will be visualised are the following: SWE, SWC, GWT, water reservoirs, and ATML. These will also be merged to illustrate the total load acting on the PGS. The total load signal will be illustrated together with the GPS observations over the period. This is to establish any possible correlation between the GNSS signal and the loading signal, specifically with respect to their phase and magnitude. If the loading signal is predominantly responsible for the elevation offsets observed in the PGS, it is expected that the two signals would exhibit a high level of similarity.

4.1.1 Hydrological loading (SWE)

As Fig. 4.1 illustrates the Snow water equivalent (SWE) load's significant impact on the deformation, with a vertical displacement ranging from approximately 6 mm to 10 mm per year. The effect is most pronounced during the early spring, gradually diminishing towards the early summer months.

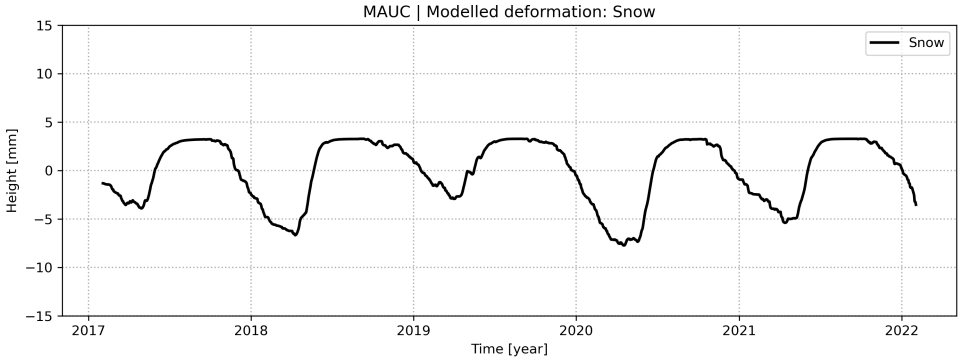

Figure 4.1: Modelled deformation caused by snow load at the PGS MAUC from 2017 to 2022.

4.1.2 Hydrological loading (GWT)

Figure 4.2 illustrates the impact of the loading signal derived from the groundwater table (GWT). The effect of this signal is on the order of a few millimetres per season. Notably, the loading effect displays a seasonal pattern, with its maximum observed during the early summer months. The groundwater loading appears to be a relatively minor contributor to the overall vertical deformation observed at the PGS, as its magnitude is notably smaller than that of other loading signals, such as the snow load. Nonetheless, its contribution should not be ignored in interpreting the PGS behaviour.

4.1.3 Hydrological loading (SMC)

As Figure 4.3 illustrates, the estimated load signal derived from the soil moisture content (SMC) has an annual deformation of approximately 4 mm.

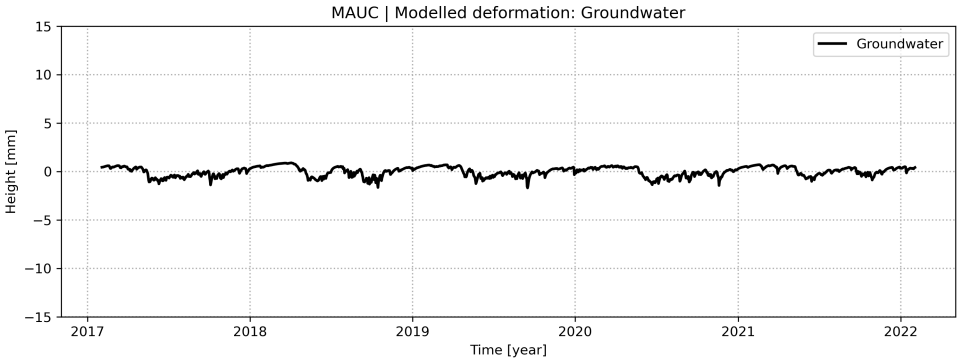

Figure 4.2: Modelled deformation caused by groundwater load at the PGS MAUC from 2017 to 2022.

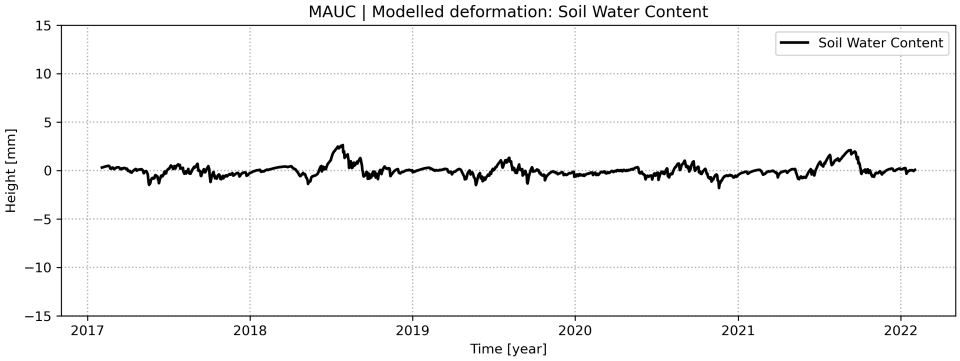

Figure 4.3: Modelled deformation caused by soil moisture content load at the PGS MAUC during the period from 2017 to 2022.

4.1.4 Water reservoir loading

Figure 4.5 shows the impact of the water level changes in the nearby Sysenvatnet reservoir on the PGS's deformation. The loading signal cooresponds to with the volume variations in the reservoir, as presented in Fig. 4.4. The annual deformation effect induced by water level changes, occurring at a distance of approximately 2.5 km, is estimated to be around 3 mm.

4.1.5 Total hydrological loading effect

Figure 4.6, presents the total elastic loading signal caused by hydrological changes in the surrounding area and water level variations in Sysenvatnet. The deformation effect due to this loading leads to an average annual vertical displacement of approximately 8 mm at MAUC.

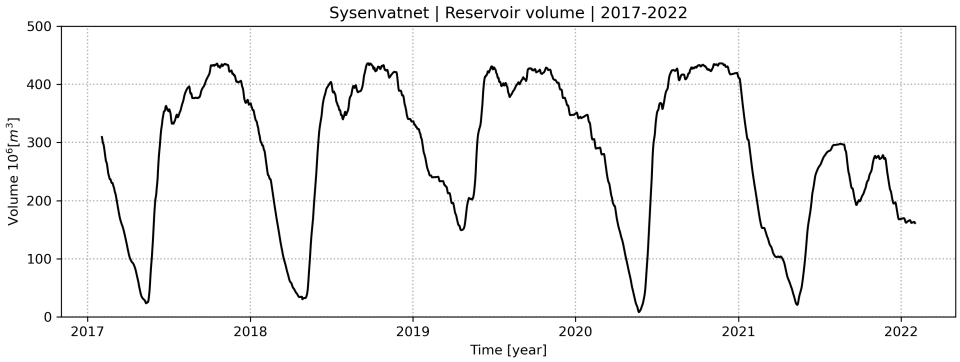

Figure 4.4: The temporal volume changes in the Sysenvatnet from 2017 to 2022 (NVE).

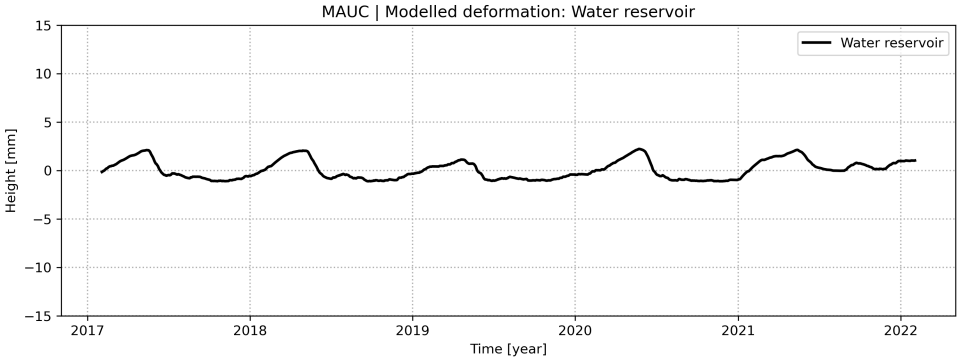

Figure 4.5: The modelled deformation caused by Sysenvatnet load at the PGS MAUC during the period from 2017 to 2022 (NVE).

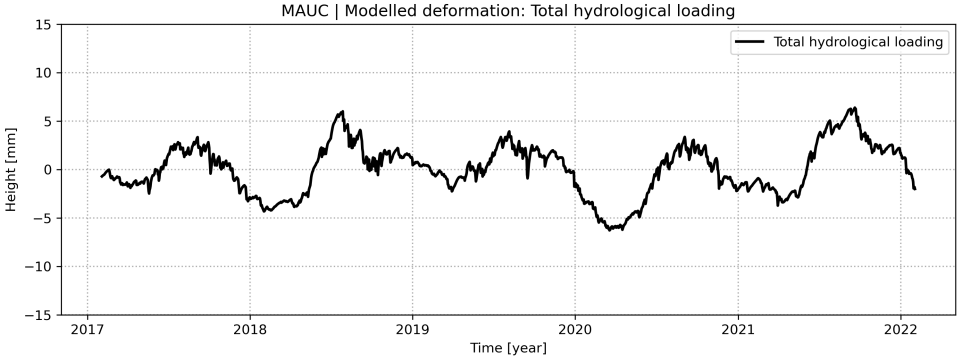

Figure 4.6: The total hydrological and water reservoir load at the PGS MAUC during the period from 2017 to 2022. (NVE)

4.1.6 Atmospheric loading

The GPS time series generated by Bernese do not incorporate corrections for atmospheric loading, which, as discussed in Chapter 2, can result in significant vertical displacement up to several centimetres. Figure 4.7 presents the atmospheric load-

ing imposed on MAUC during the period. The graph displays seasonal behaviour, indicating that the signal is less influential during winter than in spring and summer. Figure 4.8 demonstrates the addition of the atmospheric loading signal to the hydrological signal. Note that there is a phase shift between the two signals, which is evident when comparing Figures 4.9 and 4.10. These figures depict the loading signals together with the GPS observations.

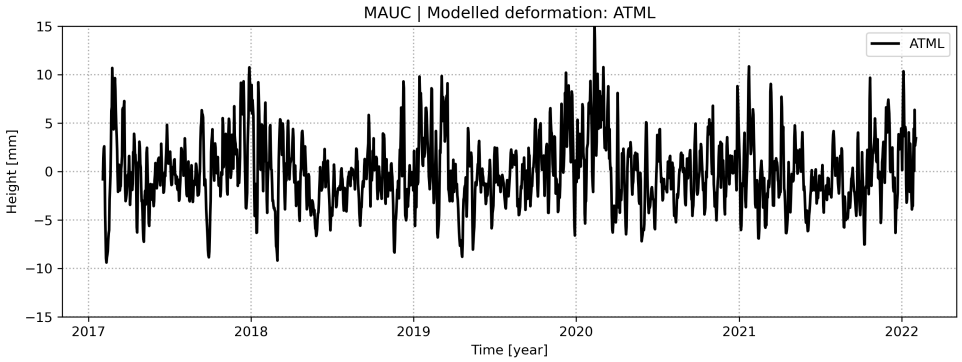

Figure 4.7: The modelled deformation caused by the atmospheric load at the PGS MAUC during the period from 2017 to 2022.

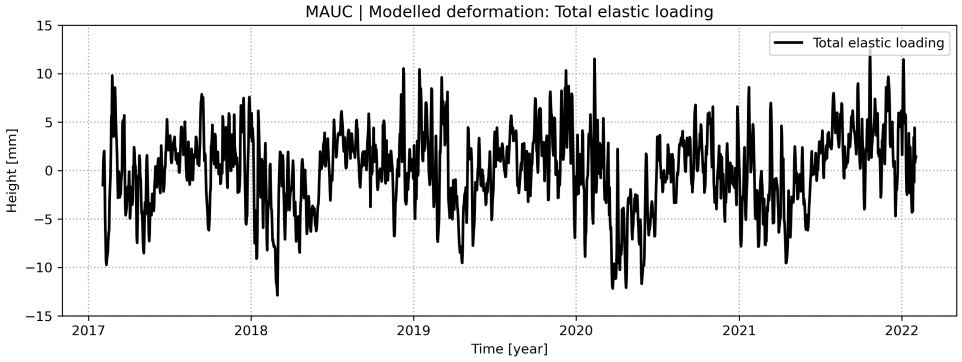

Figure 4.8: The modelled deformation caused by the total hydrological, atmospherical and water reservoir load at the PGS MAUC during the period from 2017 to 2022.

4.1.7 Comparison to GPS observations

Figure 4.9 depicts the hydrological signal only, whereas Fig. 4.10 combines the hydrological and atmospheric signals. The atmospheric signal that has been added to the total hydrological signal in Fig. 4.10 has been smoothed for ease of interpretation, and the total elastic signal in this figure exhibits a less pronounced seasonal pattern than the hydrological signal in Fig. 4.9. Moreover, Figure 4.9 reveals a phase

shift between the hydrological loading signal and the GPS observations, which is noticeable when comparing the regression line (that stems from Eq. 3.1) and the loading signal. In Fig. 4.11, the vertical deformation caused by the water reservoir is displayed, together with the GPS observations; this graph also shows that the seasonal signal of the observations does not show any similarities with the seasonal signal from the water reservoir.

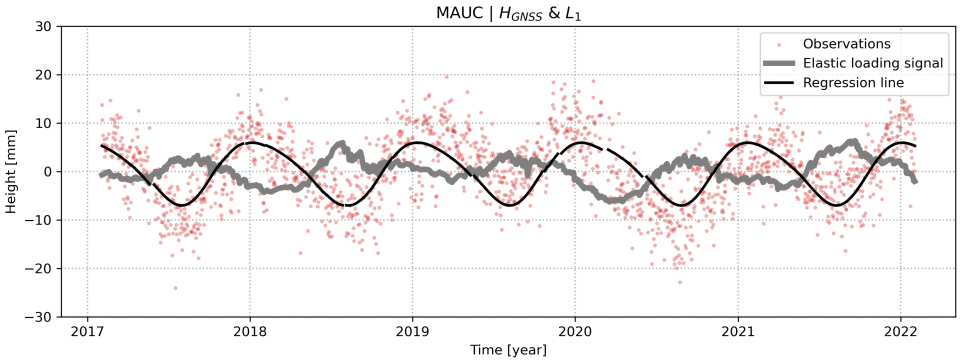

Figure 4.9: GPS observations, the regression line, and the total elastic loading signal derived from the hydrological and the water reservoir loading. As seen in the graph, there is a phase shift between the elastic loading signal and the regression line of the GPS observations.

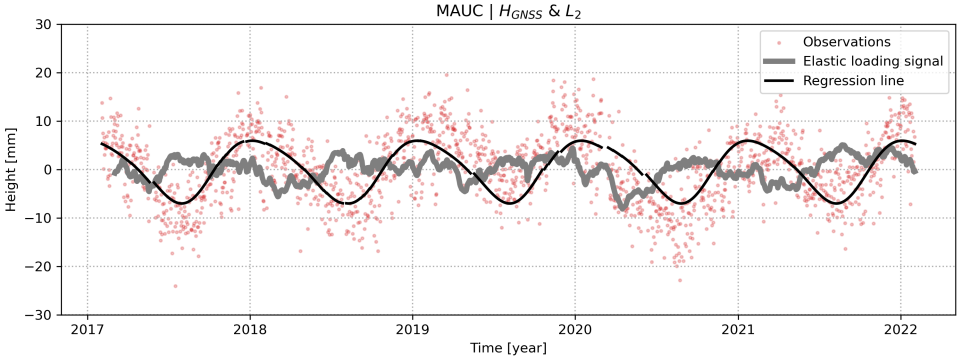

Figure 4.10: GPS observations, the regression line, and the total elastic loading signal derived from the hydrological, the atmospherical, and the water reservoir loading. As seen in the graph, there is a phase shift between the elastic loading signal and the regression line of the GPS observations.

The seasonal signal observed in the GPS data exhibits negligible resemblance in both magnitude and phase to the loading signals obtained from the hydrological data or water reservoir. There are some resemblances in the periodic signal present in atmospheric loading, seen in Fig. 4.12. The prominent seasonal signal evident in the GPS observations cannot be attributed to either the reservoir or other modelled loading signals, or at least not to those available in the data.

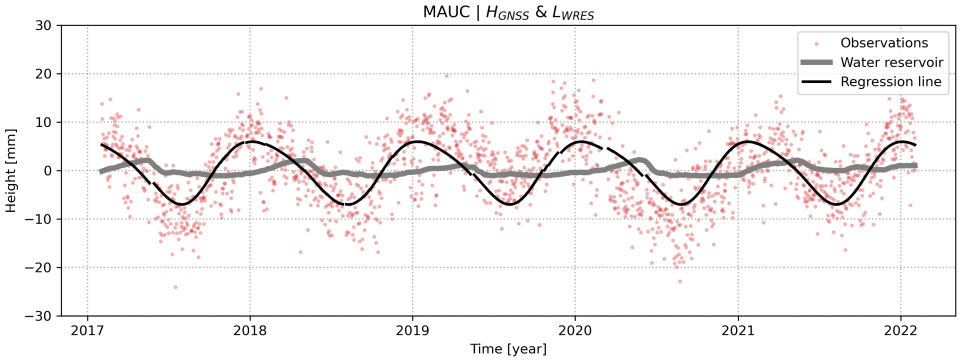

Figure 4.11: GPS observations, the regression line, and the total elastic loading signal derived from the water reservoir loading. As seen in the graph, there is a phase shift between the elastic loading signal and the regression line of the GPS observations.

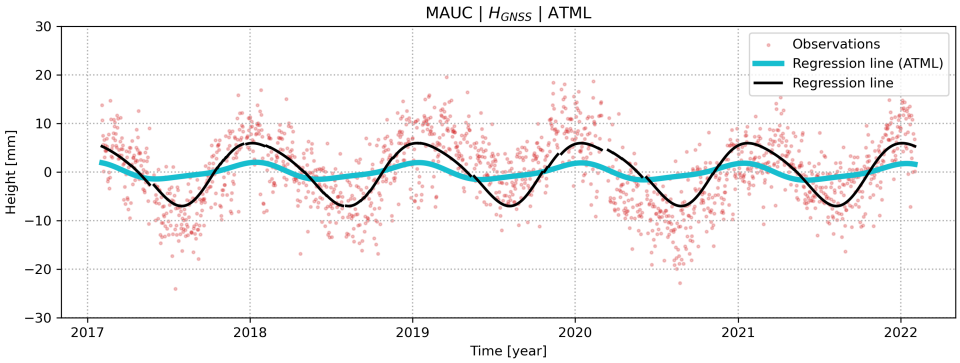

Figure 4.12: GPS observations, the regression line, and the seasonal smoothed regression line for the ATML. The graph shows that the seasonal smoothed regression line for the ATML corresponds well with the uplift of the GPS observations during the winter months.

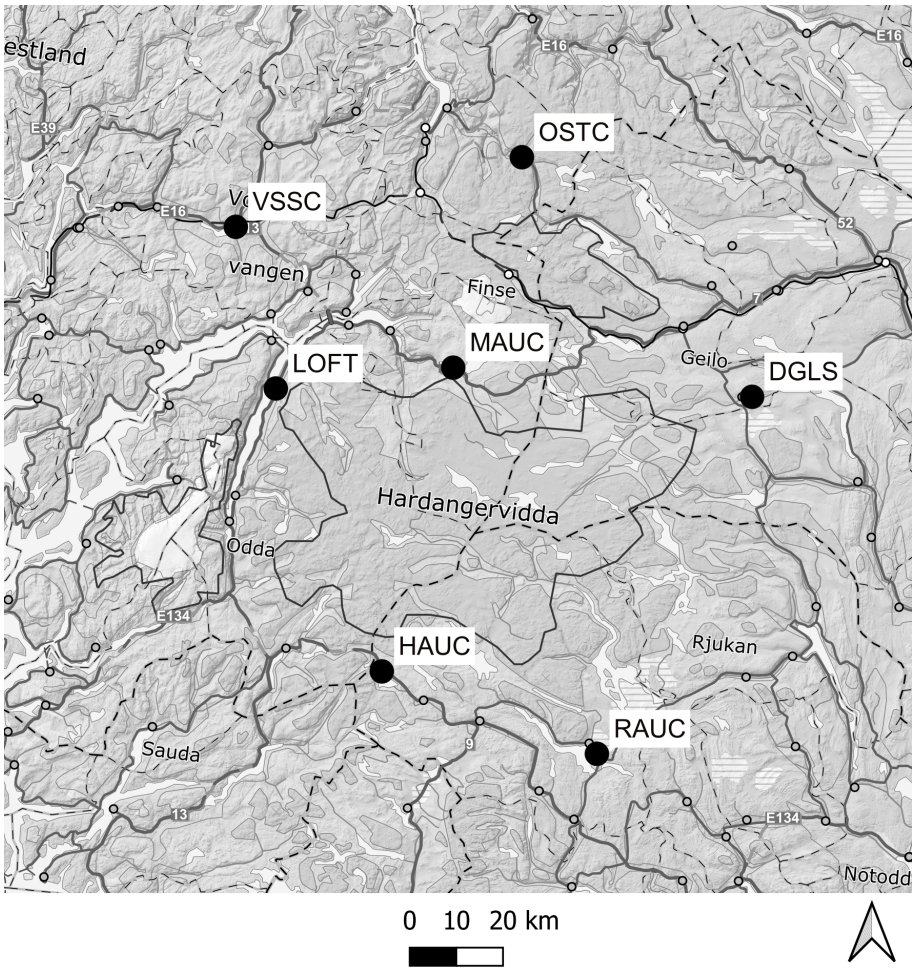

Figure 4.13: The locations of the permanent GNSS PGSs that were utilized in this study. The locations of the PGSs are depicted as black dots on the map. (Topografisk Norgeskart gråtone, 2017)

4.2 Analysing the GPS time series

The subsequent sections, tables and graphs will show the results of subtracting the loading signal from the observed GPS time series and the effects of common mode filtering. Figures showing time series for all stations are available in the appendix, and only results deemed especially interesting will be presented in this Chapter. A total of eight different analyses are carried out, six of which are conducted on the time series from Bernese and two from the time series from GAMIT/GLOBK. The various analyses examine the influence of introducing or removing specific estimated loading signals and PGSs components on the time series. An overview of all the PGSs used in the study is presented in Fig. 4.13

As previously mentioned, the study was conducted in six distinct analyses, which can be categorised into three datasets and two methods of approach. The datasets include the Bernese time series without atmospheric loading corrections, the Bernese time series with corrections for atmospheric loading, and the GAMIT/GLOBK time series. As the GAMIT/GLOBK time series exhibits a two-year hiatus at the DGLS station, this station has been excluded from this solution. Consequently, to facilitate a fair comparison between the two network solutions, a Bernese solution omitting DGLS has been incorporated. The methods of approach are described as follows:

Firstly, an analysis was performed that included all hydrological loading signals as a basis for computing the common mode error. This analysis is denoted as L1.

Secondly, an analysis was carried out, excluding all modelled hydrological loading signals and only computing the common mode filtering using the loading signal from the water reservoirs. This analysis aimed to assess the influence of the local load signal on the PGS and to ascertain whether other elastic loading signals are essential in this type of network or not. This analysis is denoted as L2.

The results are summarized in Table 4.2 to 4.16 and follow a standardised format, where the first row of each PGS represents the detrended and outlier-free original GPS solution titled H_{GNSS}, i.e., the unfiltered time series. The second row shows the unfiltered time series with the subtracted loading effect $H_{GNSS} - L$. The third row displays the results of common mode filtering on the unfiltered time series H_{CM}, while the fourth row demonstrates the common mode filtering on the $H_{GNSS} - L$ values. The columns report the RMSE of the time series, the RMSE relative to the unfiltered time series, the amplitude of the seasonal signal, the standard deviation of the amplitude, and the amplitude relative to the unfiltered time series.

All comparisons are relative to the unfiltered time series, denoted as H_{GNSS}.

The RMSE value quantifies the magnitude of the residual noise or error present in a given time series. The amplitude indicates the magnitude of the unmodelled periodic signals in the time series. Lower values of both RMSE and amplitude are preferred. Lower RMSE values indicate a higher accuracy in the predicted time series, and a lower amplitude indicates that deformations or other periodic effects are correctly modelled or removed by common mode.

4.2.1 Bernese, L1

These findings are based on the GPS time series from the Bernese software and removing the loading signal derived from the hydrological loading and the proximate water reservoirs. This supposition assumes that the loading effect stemming from the atmospheric pressure was uniformly distributed across all PGSs in the network and would be corrected through common mode filtering. Comprehensive results can be found in Tables 4.1 and 4.2.

$\mathbf{H_{GNSS} - L}$

Table 4.2 illustrates that removing the loading signal $H_{GNSS} - L$ slightly reduces the RMSE values. An increase in the annual amplitude is observed, suggesting that the load signal is concealing a more substantial unmodelled periodic signal. These findings are consistent with those of (Kierulf et al., 2022), who documented a similar rise in amplitude and a decrease in RMSE upon applying the modelled loading signal.

$\mathbf{H_{CM}}$

The common mode filtering analysis reduces the RMSE values for all PGSs, averaging 27%. In addition, the amplitude decreased for all PGSs, except for RAUC and VSSC. Where RAUC shows a significant increase of 79%, and VSSC remains unchanged.

$\mathbf{H_{CM,L}}$

The RMSE reduction exhibits a marginally lower decrease in this solution compared to H_{CM}, i.e., a 26% reduction on average. The amplitude is diminished relative to H_{GNSS} for all PGSs except RAUC, averaging a 32% reduction. However, the amplitude of RAUC is decreased concerning the H_{CM} solution. It is worth noting

that the amplitude is less reduced for all PGSs compared to the H_{CM} time series, excluding LOFT, MAUC, and VSSC. The amplitude discrepancies between the H_{CM} and $H_{\mathrm{CM,L}}$ solutions are solely statistically significant for the PGSs DGLS, MAUC, and RAUC, where they surpass two standard deviations.

Table 4.1: The table shows the average relative values from Table 4.2.

	Avg. RMS diff. (%)	Avg. AMP diff. (%)
$H_{\mathrm{GNSS}} - L$	-5	73
H_{CM}	-27	-26
$H_{\mathrm{CM,L}}$	-26	-32

Table 4.2: The Bernese solution for all PGSs within the network, with L denoting the loading signal derived from hydrological and water reservoir loadings. Displayed are the annual RMSE, amplitude, and amplitude's standard deviation. The variations in RMSE and amplitude are relative to H_{GNSS}. H_{GNSS} represents the unfiltered time series, whereas $H_{\mathrm{GNSS}} - L$ corresponds to the unfiltered time series with the loading effect subtracted. H_{CM} refers to the common mode-filtered time series based on H_{GNSS}, and $H_{\mathrm{CM,L}}$ refers to the common mode-filtered time series applied to $H_{\mathrm{GNSS}} - L$.

PGS		RMSE (mm)	RMSE diff (%)	Amp (mm)	Amp std (mm)	Amp diff (%)
DGLS						
	H_{GNSS}	5.4		5.2	+/-0.2	
	$H_{\mathrm{GNSS}} - L$	5.3	-2	7.4	+/-0.2	42
	H_{CM}	4.1	-24	2.7	+/-0.1	-48
	$H_{\mathrm{CM,L}}$	4.2	-22	3.0	+/-0.1	-42
HAUC						
	H_{GNSS}	5.5		2.6	+/-0.2	
	$H_{\mathrm{GNSS}} - L$	5.0	-9	4.5	+/-0.2	73
	H_{CM}	3.8	-31	0.4	+/-0.1	-85
	$H_{\mathrm{CM,L}}$	3.8	-31	0.5	+/-0.1	-81
LOFT						
	H_{GNSS}	6.6		2.1	+/-0.2	
	$H_{\mathrm{GNSS}} - L$	6.3	-5	4.2	+/-0.2	100
	H_{CM}	4.9	-26	1.2	+/-0.2	-43
	$H_{\mathrm{CM,L}}$	4.9	-26	1.1	+/-0.2	-48
MAUC						
	H_{GNSS}	5.6		6.4	+/-0.2	
	$H_{\mathrm{GNSS}} - L$	5.3	-5	8.9	+/-0.2	39
	H_{CM}	4.2	-25	4.3	+/-0.1	-33
	$H_{\mathrm{CM,L}}$	4.3	-23	4.0	+/-0.1	-38
OSTC						
	H_{GNSS}	6.4		4.7	+/-0.2	
	$H_{\mathrm{GNSS}} - L$	6.1	-5	7.2	+/-0.2	53
	H_{CM}	4.5	-30	2.4	+/-0.2	-49
	$H_{\mathrm{CM,L}}$	4.6	-28	2.5	+/-0.2	-47
RAUC						
	H_{GNSS}	5.1		1.9	+/-0.2	
	$H_{\mathrm{GNSS}} - L$	4.9	-4	3.9	+/-0.2	105
	H_{CM}	3.9	-24	3.4	+/-0.1	79
	$H_{\mathrm{CM,L}}$	3.9	-24	2.8	+/-0.1	47
VSSC						
	H_{GNSS}	5.4		1.7	+/-0.2	
	$H_{\mathrm{GNSS}} - L$	5.1	-6	3.4	+/-0.2	100
	H_{CM}	4.0	-26	1.7	+/-0.1	0
	$H_{\mathrm{CM,L}}$	4.0	-26	1.5	+/-0.1	-12

4.2.2 Bernese, L2

These results are based on the GPS time series derived from Bernese and the loadings signal from nearby water reservoirs, assuming that the other loading signals were uniform across all PGSs in the network and would be removed by common mode filtering. The overall results are available in Tables 4.3 and 4.4. If not directly specified, all comparisons are relative to the unfiltered time series, denoted as H_{GNSS}.

$\mathbf{H_{GNSS} - L}$

Table 4.4 demonstrates that removing the loading signal will have no impact on the RMSE. Nevertheless, amplitude alterations are observed at the PGSs situated near water reservoirs, HAUC, MAUC, OSTC, and RAUC. HAUC and OSTC adhere to the trend discerned in prior analyses and exhibit a marginal amplitude increase, while MAUC and RAUC display a decrease. This observation suggests that a portion of the seasonal signal is associated with fluctuations in water levels proximate to these PGSs reservoirs. Notably, RAUC shows a substantial decline of 32%.

$\mathbf{H_{CM}}$

The outcomes of the common mode filtering applied to the unfiltered time series align with those in Table 4.2 and are solely present in the table to reference the $H_{\mathrm{CM,L}}$ values.

$\mathbf{H_{CM,L}}$

The RMSE values correspond to those presented in Table 4.2, barring OSTC, which exhibits marginally lower values. The mean RMSE reduction stands at 26%. The amplitude reductions resemble those in Table 4.1, averaging a 28% reduction. HAUC exhibits an increased amplitude compared to the $H_{\mathrm{CM,L}}$ solution and the values presented in Table 4.2 and the H_{CM} solution in Table 4.4. This suggests that the modelled load effect of the nearby water reservoirs may be inaccurate.

Table 4.3: The average relative values from Table 4.4.

	Avg. RMS diff. (%)	Avg. AMP diff. (%)
$H_{\mathrm{GNSS}} - L$	0	-4
H_{CM}	-27	-26
$H_{\mathrm{CM,L}}$	-26	-28

Table 4.4: The Bernese solution for all PGSs within the network, with L denoting the loading signal derived from water reservoir loadings. Displayed are the annual RMSE, amplitude, and amplitude's standard deviation. The variations in RMSE and amplitude are relative to H_{GNSS}. H_{GNSS} represents the unfiltered time series, whereas $H_{\mathrm{GNSS}} - L$ corresponds to the unfiltered time series with the loading effect subtracted. H_{CM} refers to the common mode-filtered time series based on H_{GNSS}, and $H_{\mathrm{CM,L}}$ refers to the common mode-filtered time series applied to $H_{\mathrm{GNSS}} - L$.

PGS		RMSE (mm)	RMSE diff (%)	Amp (mm)	Amp std (mm)	Amp diff (%)
DGLS						
	H_{GNSS}	5.4		5.2	+/-0.2	
	$H_{\mathrm{GNSS}} - L$	5.4	0	5.2	+/-0.2	0
	H_{CM}	4.1	-24	2.7	+/-0.1	-48
	$H_{\mathrm{CM,L}}$	4.2	-22	2.8	+/-0.1	-46
HAUC						
	H_{GNSS}	5.5		2.6	+/-0.2	
	$H_{\mathrm{GNSS}} - L$	5.5	0	2.8	+/-0.2	8
	H_{CM}	3.8	-31	0.4	+/-0.1	-85
	$H_{\mathrm{CM,L}}$	3.8	-31	1.0	+/-0.1	-62
LOFT						
	H_{GNSS}	6.6		2.1	+/-0.2	
	$H_{\mathrm{GNSS}} - L$	6.6	0	2.1	+/-0.2	0
	H_{CM}	4.9	-26	1.2	+/-0.2	-43
	$H_{\mathrm{CM,L}}$	4.9	-26	1.0	+/-0.2	-52
MAUC						
	H_{GNSS}	5.6		6.4	+/-0.2	
	$H_{\mathrm{GNSS}} - L$	5.6	0	6.1	+/-0.2	-5
	H_{CM}	4.2	-25	4.3	+/-0.1	-33
	$H_{\mathrm{CM,L}}$	4.3	-23	4.0	+/-0.1	-38
OSTC						
	H_{GNSS}	6.4		4.7	+/-0.2	
	$H_{\mathrm{GNSS}} - L$	6.4	0	4.8	+/-0.2	2
	H_{CM}	4.5	-30	2.4	+/-0.2	-49
	$H_{\mathrm{CM,L}}$	4.5	-30	2.4	+/-0.2	-49
RAUC						
	H_{GNSS}	5.1		1.9	+/-0.2	
	$H_{\mathrm{GNSS}} - L$	5.1	0	1.3	+/-0.2	-32
	H_{CM}	3.9	-24	3.4	+/-0.1	79
	$H_{\mathrm{CM,L}}$	3.9	-24	3.1	+/-0.1	63
VSSC						
	H_{GNSS}	5.4		1.7	+/-0.2	
	$H_{\mathrm{GNSS}} - L$	5.4	0	1.7	+/-0.2	0
	H_{CM}	4.0	-26	1.7	+/-0.1	0
	$H_{\mathrm{CM,L}}$	4.0	-26	1.5	+/-0.1	-12

4.2.3 Bernese, L1 with ATML

These results are based on the GPS time series derived from Bernese and the removal of the loadings signal derived from hydrological loading, atmospheric pressure, and nearby water reservoirs. The results are available in Tables 4.5 and 4.6.

$\mathbf{H_{GNSS} - L}$

Tables 4.6 and 4.5 present the analysis results indicating that removing the loading signal leads to a 2% and 53% increase in RMSE and amplitude, respectively, for the entire network.

$\mathbf{H_{CM}}$

The outcomes of the common mode filtering applied to the unfiltered time series align with those in Table 4.2 and are solely present to reference the $H_{CM,L}$ values.

$\mathbf{H_{CM,L}}$

The common mode filtering applied to the $H_{GNSS} - L$ signal exhibits results akin to those delineated in Table 4.2, with average values bearing a resemblance, as observed in Tables 4.1 and 4.5.

Table 4.5: The average relative values from Table 4.6.

	Avg. RMS diff. (%)	Avg. AMP diff. (%)
$H_{\mathrm{GNSS}} - L$	2	53
H_{CM}	-27	-26
$H_{\mathrm{CM,L}}$	-26	-24

Table 4.6: The Bernese solution for all PGSs within the network, with L denoting the loading signal derived from atmospheric, hydrological, and water reservoir loadings. Displayed are the annual RMSE, amplitude, and amplitude's standard deviation. The variations in RMSE and amplitude are relative to H_{GNSS}. H_{GNSS} represents the unfiltered time series, whereas $H_{\mathrm{GNSS}} - L$ corresponds to the unfiltered time series with the loading effect subtracted. H_{CM} refers to the common mode-filtered time series based on H_{GNSS}, and $H_{\mathrm{CM,L}}$ refers to the common mode-filtered time series applied to $H_{\mathrm{GNSS}} - L$.

PGS		RMSE (mm)	RMSE diff (%)	Amp (mm)	Amp std (mm)	Amp diff (%)
DGLS						
	H_{GNSS}	5.4		5.2	+/-0.2	
	$H_{\mathrm{GNSS}} - L$	5.6	4	6.2	+/-0.2	19
	H_{CM}	4.1	-24	2.7	+/-0.1	-48
	$H_{\mathrm{CM,L}}$	4.1	-24	2.9	+/-0.1	-44
HAUC						
	H_{GNSS}	5.5		2.6	+/-0.2	
	$H_{\mathrm{GNSS}} - L$	5.3	-4	3.8	+/-0.2	46
	H_{CM}	3.8	-31	0.4	+/-0.1	-85
	$H_{\mathrm{CM,L}}$	3.8	-31	0.5	+/-0.1	-81
LOFT						
	H_{GNSS}	6.6		2.1	+/-0.2	
	$H_{\mathrm{GNSS}} - L$	6.8	3	3.7	+/-0.2	76
	H_{CM}	4.9	-26	1.2	+/-0.2	-43
	$H_{\mathrm{CM,L}}$	4.8	-27	1.1	+/-0.2	-48
MAUC						
	H_{GNSS}	5.6		6.4	+/-0.2	
	$H_{\mathrm{GNSS}} - L$	5.7	2	7.9	+/-0.2	23
	H_{CM}	4.2	-25	4.3	+/-0.1	-33
	$H_{\mathrm{CM,L}}$	4.3	-23	4.0	+/-0.1	-38
OSTC						
	H_{GNSS}	6.4		4.7	+/-0.2	
	$H_{\mathrm{GNSS}} - L$	6.6	3	6.2	+/-0.2	32
	H_{CM}	4.5	-30	2.4	+/-0.2	-49
	$H_{\mathrm{CM,L}}$	4.6	-28	2.3	+/-0.2	-51
RAUC						
	H_{GNSS}	5.1		1.9	+/-0.2	
	$H_{\mathrm{GNSS}} - L$	5.5	8	4.0	+/-0.2	111
	H_{CM}	3.9	-24	3.4	+/-0.1	79
	$H_{\mathrm{CM,L}}$	4.0	-22	2.8	+/-0.1	47
VSSC						
	H_{GNSS}	5.4		1.7	+/-0.2	
	$H_{\mathrm{GNSS}} - L$	5.3	-2	2.8	+/-0.2	65
	H_{CM}	4.0	-26	1.7	+/-0.1	0
	$H_{\mathrm{CM,L}}$	4.0	-26	1.5	+/-0.1	-12

4.2.4 Bernese L2 with ATML

These results are based on the GPS time series derived from Bernese and removing the loadings signal from nearby water reservoirs and ATML, assuming that the hydrological loading signals were uniform across all PGSs in the network and would be removed by common mode filtering. The results are available in Tables 4.7 and 4.8.

$\mathbf{H_{GNSS} - L}$

Tables 4.8 and 4.7 show a slight increase in RMSE for all PGSs, with an average of 8%. The amplitude, however, is significantly reduced for all PGSs except RAUC. The overall reduction of the amplitude indicates that part of the periodic signal is due to atmospheric loading. The average amplitude reduction is -25%.

$\mathbf{H_{CM}}$

The outcomes of the common mode filtering applied to the unfiltered time series align with those in Table 4.2 and are solely present in the table to reference the $H_{\mathrm{CM,L}}$ values.

$\mathbf{H_{CM,L}}$

The common mode filtering applied to the $H_{GNSS} - L$ signal yields results akin to those delineated in Table 4.4, and the average values closely resemble one another, as evidenced by the comparison between Tables 4.3 and 4.7. This observation further implies that, for a network of this particular size, it would suffice to merely estimate the local load effect and subsequently attenuate the influence of other factors through common mode filtering.

Table 4.7: The average relative values from Table 4.8.

	Avg. RMS diff. (%)	Avg. AMP diff. (%)
$H_{\mathrm{GNSS}} - L$	8	-25
H_{CM}	-27	-26
$H_{\mathrm{CM,L}}$	-26	-24

Table 4.8: The Bernese solution for all PGSs within the network, with L denoting the loading signal derived from atmospheric and water reservoir loadings. Displayed are the annual RMSE, amplitude, and amplitude's standard deviation. The variations in RMSE and amplitude are relative to H_{GNSS}. H_{GNSS} represents the unfiltered time series, whereas $H_{\mathrm{GNSS}} - L$ corresponds to the unfiltered time series with the loading effect subtracted. H_{CM} refers to the common mode-filtered time series based on H_{GNSS}, and $H_{\mathrm{CM,L}}$ refers to the common mode-filtered time series applied to $H_{\mathrm{GNSS}} - L$.

PGS		RMSE (mm)	RMSE diff (%)	Amp (mm)	Amp std (mm)	Amp diff (%)
DGLS						
	H_{GNSS}	5.4	0	5.2	+/-0.2	0
	$H_{\mathrm{GNSS}} - L$	5.8	7	3.6	+/-0.2	-31
	H_{CM}	4.1	-24	2.7	+/-0.1	-48
	$H_{\mathrm{CM,L}}$	4.1	-24	2.7	+/-0.1	-48
HAUC						
	H_{GNSS}	5.5	0	2.6	+/-0.2	0
	$H_{\mathrm{GNSS}} - L$	5.8	5	1.7	+/-0.2	-35
	H_{CM}	3.8	-31	0.4	+/-0.1	-85
	$H_{\mathrm{CM,L}}$	3.8	-31	1.0	+/-0.1	-62
LOFT						
	H_{GNSS}	6.6	0	2.1	+/-0.2	0
	$H_{\mathrm{GNSS}} - L$	7.1	8	1.4	+/-0.2	-33
	H_{CM}	4.9	-26	1.2	+/-0.2	-43
	$H_{\mathrm{CM,L}}$	4.8	-27	1.0	+/-0.2	-52
MAUC						
	H_{GNSS}	5.6	0	6.4	+/-0.2	0
	$H_{\mathrm{GNSS}} - L$	6.0	7	4.7	+/-0.2	-27
	H_{CM}	4.2	-25	4.3	+/-0.1	-33
	$H_{\mathrm{CM,L}}$	4.3	-23	3.9	+/-0.1	-39
OSTC						
	H_{GNSS}	6.4	0	4.7	+/-0.2	0
	$H_{\mathrm{GNSS}} - L$	6.9	8	3.2	+/-0.2	-32
	H_{CM}	4.5	-30	2.4	+/-0.2	-49
	$H_{\mathrm{CM,L}}$	4.6	-28	2.3	+/-0.2	-51
RAUC						
	H_{GNSS}	5.1	0	1.9	+/-0.2	0
	$H_{\mathrm{GNSS}} - L$	5.8	14	2.3	+/-0.2	21
	H_{CM}	3.9	-24	3.4	+/-0.1	79
	$H_{\mathrm{CM,L}}$	4.0	-22	3.1	+/-0.1	63
VSSC						
	H_{GNSS}	5.4	0	1.7	+/-0.2	0
	$H_{\mathrm{GNSS}} - L$	5.7	6	1.0	+/-0.2	-41
	H_{CM}	4.0	-26	1.7	+/-0.1	0
	$H_{\mathrm{CM,L}}$	4.0	-26	1.4	+/-0.1	-18

4.2.5 Bernese, L1, – without DGLS

As mentioned earlier, for a fair comparison between the results obtained from the Bernese software and GAMIT/GLOBK, the networks must share the same basis, i.e., the same PGSs. Since DGLS was removed from the GAMIT/GLOBK due to an incomplete dataset, a second network solution for Bernese was added, excluding DGLS. In light of the similarities in solutions with or without ATML correction regarding common mode, this network solution solely consists of a solution without ATML correction. This implies that the results are based on the GPS time series and the removal of the loading signal derived from hydrological loading and nearby water reservoirs. Results can be found in Tables 4.9 and 4.10.

$\mathbf{H_{GNSS} - L}$

The values of removing the loading signal from the observed time series are the same as in Table 4.2 and are only included as a reference.

$\mathbf{H_{CM}}$

Generally, the values are consistent with those found in Table 4.2.

$\mathbf{H_{CM,L}}$

The RMSE values are unchanged in this network solution compared to the one presented in Table 4.2. However, the amplitudes differ, with significantly better values displayed at MAUC, RAUC and VSSC.

Table 4.9: The table shows the average relative values from Table 4.10.

	Avg. RMS diff. (%)	Avg. AMP diff. (%)
HGNSS-L	-6	79
HCM	-28	-27
HCML	-28	-37

Table 4.10: The Bernese solution for all PGSs within the network except the PGS DGLS, with L denoting the loading signal derived from hydrological and water reservoir loadings. Displayed are the annual RMSE, amplitude, and amplitude's standard deviation. The variations in RMSE and amplitude are relative to H_{GNSS}. H_{GNSS} represents the unfiltered time series, whereas $H_{\mathrm{GNSS}} - L$ corresponds to the unfiltered time series with the loading effect subtracted. H_{CM} refers to the common mode-filtered time series based on H_{GNSS}, and $H_{\mathrm{CM,L}}$ refers to the common mode-filtered time series applied to $H_{\mathrm{GNSS}} - L$.

PGS		RMSE (mm)	RMSE diff (%)	Amp (mm)	Amp std (mm)	Amp diff (%)
HAUC						
	H_{GNSS}	5.5		2.6	+/-0.2	
	$H_{\mathrm{GNSS}} - L$	5.0	-9	4.5	+/-0.2	73
	H_{CM}	3.7	-33	0.7	+/-0.1	-73
	$H_{\mathrm{CM,L}}$	3.7	-33	0.6	+/-0.1	-77
LOFT						
	H_{GNSS}	6.6		2.1	+/-0.2	
	$H_{\mathrm{GNSS}} - L$	6.3	-5	4.2	+/-0.2	100
	H_{CM}	4.7	-29	0.9	+/-0.2	-57
	$H_{\mathrm{CM,L}}$	4.7	-29	0.7	+/-0.2	-67
MAUC						
	H_{GNSS}	5.6		6.4	+/-0.2	
	$H_{\mathrm{GNSS}} - L$	5.3	-5	8.9	+/-0.2	39
	H_{CM}	4.3	-23	4.7	+/-0.1	-27
	$H_{\mathrm{CM,L}}$	4.3	-23	4.5	+/-0.1	-30
OSTC						
	H_{GNSS}	6.4		4.7	+/-0.2	
	$H_{\mathrm{GNSS}} - L$	6.1	-5	7.2	+/-0.2	53
	H_{CM}	4.4	-31	2.9	+/-0.2	-38
	$H_{\mathrm{CM,L}}$	4.5	-30	3.0	+/-0.2	-36
RAUC						
	H_{GNSS}	5.1		1.9	+/-0.2	
	$H_{\mathrm{GNSS}} - L$	4.9	-4	3.9	+/-0.2	105
	H_{CM}	3.9	-24	2.9	+/-0.1	53
	$H_{\mathrm{CM,L}}$	3.9	-24	2.3	+/-0.1	21
VSSC						
	H_{GNSS}	5.4		1.7	+/-0.2	
	$H_{\mathrm{GNSS}} - L$	5.1	-6	3.4	+/-0.2	100
	H_{CM}	4.0	-26	1.4	+/-0.1	-18
	$H_{\mathrm{CM,L}}$	4.0	-26	1.1	+/-0.1	-35

4.2.6 Bernese, L2 – without DGLS

These findings stem from the GPS time series obtained using the Bernese and the removal of the loading signal originating from adjacent water reservoirs, with the exclusion of the PGS DGLS. The results can be found in Tables 4.12 and 4.11.

$\mathbf{H_{GNSS} - L}$ After removing the loading signal from the observed time series, the resulting values are the same as in Table 4.4 and are only included as a reference.

$\mathbf{H_{CM}}$ The values generally align with those presented in Table 4.4, albeit with marginally improved outcomes for RAUC.

$\mathbf{H_{CM,L}}$ The RMSE values are in the same magnitude in this network solution compared to the one presented in Table 4.4. However, the amplitudes differ, with significantly better values displayed at VSSC.

Table 4.11: The average relative values from Table 4.12.

	Avg. RMS diff. (%)	Avg. AMP diff. (%)
$H_{\mathrm{GNSS}} - L$	0	-5
H_{CM}	-28	-27
$H_{\mathrm{CM,L}}$	-26	-32

Table 4.12: The Bernese solution for all PGSs within the network except the PGS DGLS, with L denoting the loading signal derived from water reservoir loadings. Displayed are the annual RMSE, amplitude, and amplitude's standard deviation. The variations in RMSE and amplitude are relative to H_{GNSS}. H_{GNSS} represents the unfiltered time series, whereas $H_{\mathrm{GNSS}} - L$ corresponds to the unfiltered time series with the loading effect subtracted. H_{CM} refers to the common mode-filtered time series based on H_{GNSS}, and $H_{\mathrm{CM,L}}$ refers to the common mode-filtered time series applied to $H_{\mathrm{GNSS}} - L$.

PGS		RMSE (mm)	RMSE diff (%)	Amp (mm)	Amp std (mm)	Amp diff (%)
HAUC						
	H_{GNSS}	5.5		2.6	+/-0.2	
	$H_{\mathrm{GNSS}} - L$	5.5	0	2.8	+/-0.2	8
	H_{CM}	3.7	-33	0.7	+/-0.1	-73
	$H_{\mathrm{CM,L}}$	3.7	-33	1.0	+/-0.1	-62
LOFT						
	H_{GNSS}	6.6		2.1	+/-0.2	
	$H_{\mathrm{GNSS}} - L$	6.6	0	2.1	+/-0.2	0
	H_{CM}	4.7	-29	0.9	+/-0.2	-57
	$H_{\mathrm{CM,L}}$	4.7	-29	0.7	+/-0.2	-67
MAUC						
	H_{GNSS}	5.6		6.4	+/-0.2	
	$H_{\mathrm{GNSS}} - L$	5.6	0	6.1	+/-0.2	-5
	H_{CM}	4.3	-23	4.7	+/-0.1	-27
	$H_{\mathrm{CM,L}}$	4.3	-23	4.5	+/-0.1	-30
OSTC						
	H_{GNSS}	6.4		4.7	+/-0.2	
	$H_{\mathrm{GNSS}} - L$	6.4	0	4.8	+/-0.2	2
	H_{CM}	4.4	-31	2.9	+/-0.2	-38
	$H_{\mathrm{CM,L}}$	4.4	-31	3.0	+/-0.2	-36
RAUC						
	H_{GNSS}	5.1		1.9	+/-0.2	
	$H_{\mathrm{GNSS}} - L$	5.1	0	1.3	+/-0.2	-32
	H_{CM}	3.9	-24	2.9	+/-0.1	53
	$H_{\mathrm{CM,L}}$	3.9	-24	2.7	+/-0.1	42
VSSC						
	H_{GNSS}	5.4		1.7	+/-0.2	
	$H_{\mathrm{GNSS}} - L$	5.4	0	1.7	+/-0.2	0
	H_{CM}	4.0	-26	1.4	+/-0.1	-18
	$H_{\mathrm{CM,L}}$	4.0	-26	1.0	+/-0.1	-41

4.2.7 GAMIT/GLOBK, L1

These results are based on the GPS time series derived from the solution given by GAMIT/GLOBK and the removal of the loadings signal derived from hydrological loading and nearby water reservoirs. As discussed in Chapter 3, this solution is already corrected for ATML. The results are shown in Tables 4.13 and 4.14.

$\mathbf{H_{GNSS}}$

In contrast to the Bernese solution, seen in Table 4.10, the RMSE values in this solution are generally higher. The amplitude values exhibit variations, although they are not consistently higher; however, the associated uncertainties are more considerable.

$\mathbf{H_{GNSS} - L}$

When the load signal is removed from the GPS time series, the RMSE values decrease, and the amplitude increases, consistent with the pattern observed in the Bernese solution, Table 4.10. The average reduction in RMSE is 4%, which is slightly lower than the value reported in Table 4.9. The amplitude shows an average increase of 48%.

$\mathbf{H_{CM}}$

The common mode filtering applied to the unfiltered time series results in a decline in RMSE and amplitude values, with mean reductions of 46% and 28%, respectively. The average RMSE reduction diverges significantly from the Bernese solution, as evident in Table 4.9. Nonetheless, the RMSE values are generally elevated while the amplitude is diminished compared to the values in Table 4.10. In concurrence with the Bernese solution, an increase in the amplitude of RAUC is observed.

$\mathbf{H_{CM,L}}$

Upon applying common mode filtering to the $H_{GNSS} - L$ signal, the mean values for RMSE and amplitudes are diminished by 34% and 45%, respectively.

Table 4.13: The table shows the average relative values from Table 4.14.

	Avg. RMS diff. (%)	Avg. AMP diff. (%)
$H_{\mathrm{GNSS}} - L$	-3	56
H_{CM}	-46	-28
$H_{\mathrm{CM,L}}$	-45	-34

Table 4.14: The GAMIT/GLOBK solution for all PGSs within the network except the PGS DGLS, with L denoting the loading signal derived from hydrological and water reservoir loadings. Displayed are the annual RMSE, amplitude, and amplitude's standard deviation. The variations in RMSE and amplitude are relative to H_{GNSS}. H_{GNSS} represents the unfiltered time series, whereas $H_{\mathrm{GNSS}} - L$ corresponds to the unfiltered time series with the loading effect subtracted. H_{CM} refers to the common mode-filtered time series based on H_{GNSS}, and $H_{\mathrm{CM,L}}$ refers to the common mode-filtered time series applied to $H_{\mathrm{GNSS}} - L$.

PGS		RMSE (mm)	RMSE diff (%)	Amp (mm)	Amp std (mm)	Amp diff (%)
HAUC						
	H_{GNSS}	8.6		2.7	+/-0.3	
	$H_{\mathrm{GNSS}} - L$	8.0	-7	3.7	+/-0.3	37
	H_{CM}	4.5	-48	1.2	+/-0.2	-56
	$H_{\mathrm{CM,L}}$	4.5	-48	1.1	+/-0.2	-59
LOFT						
	H_{GNSS}	8.9		1.9	+/-0.3	
	$H_{\mathrm{GNSS}} - L$	8.6	-3	4.1	+/-0.3	116
	H_{CM}	5.1	-43	0.6	+/-0.2	-68
	$H_{\mathrm{CM,L}}$	5.1	-43	0.6	+/-0.2	-68
MAUC						
	H_{GNSS}	8.0		5.0	+/-0.3	
	$H_{\mathrm{GNSS}} - L$	7.6	-5	7.4	+/-0.3	48
	H_{CM}	4.6	-43	4.1	+/-0.2	-18
	$H_{\mathrm{CM,L}}$	4.6	-43	3.9	+/-0.2	-22
OSTC						
	H_{GNSS}	8.4		3.4	+/-0.3	
	$H_{\mathrm{GNSS}} - L$	8.0	-5	5.7	+/-0.3	68
	H_{CM}	4.4	-48	2.0	+/-0.1	-41
	$H_{\mathrm{CM,L}}$	4.5	-46	2.2	+/-0.1	-35
RAUC						
	H_{GNSS}	8.7		2.4	+/-0.3	
	$H_{\mathrm{GNSS}} - L$	8.4	-3	3.0	+/-0.3	25
	H_{CM}	4.8	-45	3.9	+/-0.2	63
	$H_{\mathrm{CM,L}}$	4.8	-45	3.3	+/-0.2	38
VSSC						
	H_{GNSS}	8.1		2.4	+/-0.3	
	$H_{\mathrm{GNSS}} - L$	7.9	-2	3.4	+/-0.3	42
	H_{CM}	4.4	-46	1.2	+/-0.1	-50
	$H_{\mathrm{CM,L}}$	4.4	-46	1.0	+/-0.1	-58

4.2.8 GAMIT/GLOBK, L2

These findings stem from the GPS time series obtained using the GAMIT/GLOBK and the removal of the loading signal originating from adjacent water reservoirs. Results are shown in Tables 4.16 and 4.16.

$\mathbf{H_{GNSS} - L}$

Removing the load signal from the GPS time series increases amplitude at HAUC and OSTC, while a slight decrease is observed at MAUC.

$\mathbf{H_{CM}}$

The outcomes of the common mode filtering applied to the unfiltered time series align with those in Table 4.14 and are solely present to reference the $H_{CM,L}$ values.

$\mathbf{H_{CM,L}}$

The exclusion of other loading signals does not benefit the solution compared to the L1 solution in Table 4.14. The overall results are similar to those in H_{CM} both regarding amplitude and RMSE. Compared to the Bernese solution in Table 4.12, the RMSE values are generally higher and the amplitudes lower, with higher uncertainties.

Table 4.15: The table shows the average relative values from Table 4.16.

	Avg. RMS diff. (%)	Avg. AMP diff. (%)
$H_{\mathrm{GNSS}} - L$	0	3
H_{CM}	-46	-28
$H_{\mathrm{CM,L}}$	-46	-29

Table 4.16: The GAMIT/GLOBK solution for all PGSs within the network except the PGS DGLS, with L denoting the loading signal derived from water reservoir loadings. Displayed are the annual RMSE, amplitude, and amplitude's standard deviation. The variations in RMSE and amplitude are relative to H_{GNSS}. H_{GNSS} represents the unfiltered time series, whereas $H_{\mathrm{GNSS}} - L$ corresponds to the unfiltered time series with the loading effect subtracted. H_{CM} refers to the common mode-filtered time series based on H_{GNSS}, and $H_{\mathrm{CM,L}}$ refers to the common mode-filtered time series applied to $H_{\mathrm{GNSS}} - L$.

PGS		RMSE (mm)	RMSE diff (%)	Amp (mm)	Amp std (mm)	Amp diff (%)
HAUC						
	H_{GNSS}	8.6	0	2.7	+/-0.3	0
	$H_{\mathrm{GNSS}} - L$	8.5	-1	3.2	+/-0.3	19
	H_{CM}	4.5	-48	1.2	+/-0.2	-56
	$H_{\mathrm{CM,L}}$	4.5	-48	1.5	+/-0.2	-44
LOFT						
	H_{GNSS}	8.9	0	1.9	+/-0.3	0
	$H_{\mathrm{GNSS}} - L$	8.9	0	1.9	+/-0.3	0
	H_{CM}	5.1	-43	0.6	+/-0.2	-68
	$H_{\mathrm{CM,L}}$	5.1	-43	0.7	+/-0.2	-63
MAUC						
	H_{GNSS}	8.0	0	5.0	+/-0.3	0
	$H_{\mathrm{GNSS}} - L$	7.9	-1	4.8	+/-0.3	-4
	H_{CM}	4.6	-43	4.1	+/-0.2	-18
	$H_{\mathrm{CM,L}}$	4.6	-43	3.9	+/-0.2	-22
OSTC						
	H_{GNSS}	8.4	0	3.4	+/-0.3	0
	$H_{\mathrm{GNSS}} - L$	8.4	0	3.5	+/-0.3	3
	H_{CM}	4.4	-48	2.0	+/-0.1	-41
	$H_{\mathrm{CM,L}}$	4.4	-48	2.2	+/-0.1	-35
RAUC						
	H_{GNSS}	8.7	0	2.4	+/-0.3	0
	$H_{\mathrm{GNSS}} - L$	8.7	0	2.4	+/-0.3	0
	H_{CM}	4.8	-45	3.9	+/-0.2	63
	$H_{\mathrm{CM,L}}$	4.8	-45	3.7	+/-0.2	54
VSSC						
	H_{GNSS}	8.1	0	2.4	+/-0.3	0
	$H_{\mathrm{GNSS}} - L$	8.1	0	2.4	+/-0.3	0
	H_{CM}	4.4	-46	1.2	+/-0.1	-50
	$H_{\mathrm{CM,L}}$	4.4	-46	0.9	+/-0.1	-62

4.2.9 Comparing variances of the time series

A variance analysis was executed on the time series to ascertain the existence of any significant disparity between the seasonal signals. The unfiltered signal H_{GNSS} was evaluated against H_{CM} and $H_{\mathrm{CM,L}}$. Bartlett's test was employed for this assessment under the null hypothesis that all input samples exhibit equal variances. Only results sourced from the solutions of Bernese (L1) and GAMIT/GLOBK (L1) are incorporated, given that the results only diverge in terms of the number of PGSs included in the network. In other words, all solutions comprising all PGSs in the network were the same, and the Bernese solution omitting DGLS was identical to GAMIT/GLOBK. The outcomes are detailed in Tables 4.17 and 4.18. For enhanced readability, p-values less than 0.05 are marked as "True", and those exceeding 0.05 are labelled as "False". Thus, "True" signifies a significant difference between the time series, leading to a rejection of the null hypothesis of equivalent variance and thus indicating that there is a significant difference in the seasonal signal.

Tables 4.17 and 4.18 show a significant difference between the unfiltered time series and those corrected for load effects and common mode filtering. The exception is the H_{CM} solution for VSSC in the Berneses solutions that include all stations, which corresponds well with the results seen in Table 4.2, where the common mode filtering does not alter the annual amplitude.

Table 4.17: P-values for the Bernese, L1 solution are represented. 'True' signifies a value below 0.05, while 'False' signifies a value exceeding 0.05. "True" suggests a statistically significant disparity between the time series.

Station	H_{CM}	$H_{\mathrm{CM,L}}$
	$P < 0.05$	$P < 0.05$
DGLS	True	True
HAUC	True	True
LOFT	True	True
MAUC	True	True
OSTC	True	True
RAUC	True	True
VSSC	False	True

Table 4.18: Similar to Table 4.17, but for GAMIT, L1

Station	H_{CM} $\mathrm{P} < 0.05$	$H_{\mathrm{CM,L}}$ $\mathrm{P} < 0.05$
HAUC	True	True
LOFT	True	True
MAUC	True	True
OSTC	True	True
RAUC	True	True
VSSC	True	True

4.2.10 Comparison of software

Both software yields similar solutions for this relatively compact network, with subtle distinctions. Generally, the Bernese software provides a more precise solution, characterised by lower RMSE, albeit with larger amplitudes. Conversely, GAMIT/-GLOBK offers a noisier solution featuring higher RMSE values and lower amplitudes with increased uncertainty.

The findings concerning the PGS MAUC compare the results obtained from both Bernese and GAMIT/GLOBK solutions. Table 4.19 demonstrates that the values following common mode filtering are comparable to a certain degree. The GAMIT/-GLOBK solution exhibits marginally higher RMSE values and uncertainties associated with the amplitude. Thus, although the amplitude results favour the GAMIT/-GLOBK solution, the network solution derived from Bernese is deemed more reliable. The higher RMSE observed with GAMIT/GLOBK solution is probably because it is a global solution, not a regional one like Bernese.

Table 4.19: The table provides a comparison of the solutions derived from different software, specifically concentrating on the PGS MAUC. The values presented are drawn from Tables 4.10 and 4.14. L denoting the loading signal derived from hydrological and water reservoir loadings. Displayed are the annual RMSE, amplitude, and amplitude's standard deviation. The variations in RMSE and amplitude are relative to H_{GNSS}. H_{GNSS} represents the unfiltered time series, whereas $H_{\mathrm{GNSS}} - L$ corresponds to the unfiltered time series with the loading effect subtracted. H_{CM} refers to the common mode-filtered time series based on H_{GNSS}, and $H_{\mathrm{CM,L}}$ refers to the common mode-filtered time series applied to $H_{\mathrm{GNSS}} - L$.

Software	PGS		RMSE (mm)	RMSE diff (%)	Amp (mm)	Amp std (mm)	Amp diff (%)
Bernese	MAUC						
		H_{GNSS}	5.6		6.4	+/-0.2	
		$H_{\mathrm{GNSS}} - L$	5.3	-5	8.9	+/-0.2	39
		H_{CM}	4.3	-23	4.7	+/-0.1	-27
		$H_{\mathrm{CM,L}}$	4.3	-23	4.5	+/-0.1	-30
GAMIT/GLOBK	MAUC						
		H_{GNSS}	8.0		5.0	+/-0.3	
		$H_{\mathrm{GNSS}} - L$	7.6	-5	7.4	+/-0.3	48
		H_{CM}	4.6	-43	4.1	+/-0.2	-18
		$H_{\mathrm{CM,L}}$	4.6	-43	3.9	+/-0.2	-22

4.3 Results on PGS

The results for each PGS within the network will be displayed as graphs illustrating the H_{GNSS}, $H_{GNSS} - L$, H_{CM}, and $H_{CM,L}$ for each respective PGS. As the various network and software solutions demonstrate similarities, only the outcomes derived from the Bernese L1, without any correction for atmospheric load, will be presented.

4.3.1 Results on DGLS

As seen in Fig. 4.14, the PGS show a clear seasonal displacement in H_{GNSS}, with a rise during the winter. After load and common mode filtering, the time series have a discernible lower amplitude and lesser spread of observations, which corresponds well with the results presented in Table 4.2.

4.3.2 Results on HAUC

In Fig. 4.15, the H_{GNSS} appears noisy, the regression line suggesting an increase during the winter months, potentially attributable to multipath effects caused by snow. Observe the lack of observation in early 2020 and the abrupt decline of the observation thereafter, exhibiting an almost rising linear trend towards 2022. This phenomenon is also present at other PGSs and corresponds well with that year's snow load, as seen in Appendix Fig. B3. The periodic signal dissipates upon applying load and common mode filtering, and the spread of observations is diminished. H_{CM} and $H_{CM,L}$ show a clear improvement in both noise and amplitude reduction.

4.3.3 Results on LOFT

The H_{GNSS} observations in Fig. 4.16 do not indicate a clear periodic signal on the time series. However, the regression line indicates a rise during the winter months. Both H_{CM} and $H_{CM,L}$ show less spread of the observations and no obvious periodic signal. Similar to HAUC, the observations show a decline in early 2020 due to snow load.

4.3.4 Results on OSTC

Figure 4.17 displays another PGS with a substantial seasonal signal, akin to DGLS, with more dispersed observations. Common mode filtering reduces both the seasonal signal and the noise within the observations. Still, as with DGLS, a periodic signal is left after the common mode filtering that shows similar tendencies, i.e., a height rise during winter.

4.3.5 Results on RAUC

RAUC is the PGS with the lowest initial RMSE and amplitude, as observed in Table 4.2, and it is the sole PGS exhibiting an increased amplitude after common mode filtering. This suggests that the other PGSs in the network slightly worsen its performance. Examining the graphs in Fig. 4.18, the H_{GNSS} regression line displays a minor increase during early summer, which is contrary to what is observed across the rest of the network. This concurs with the modelled deformation attributed to the nearby water reservoirs, as detailed in Appendix Fig. B11. The impact of removing the load associated with the water reservoirs is further evident in the $H_{GNSS} - L$ values presented in Table 4.4, where the amplitude decreases. The $H_{CM,L}$ graph reveals that the H_{GNSS} signal appears to be amplified but with a reduced spread.

4.3.6 Results on VSSC

VSSC is like RAUC, a PGS with initially low RMSE and amplitude, as seen in Table 4.2. This is further evident when examining the graphs in Fig. 4.19. The PGS observations do correspond well to both common mode filtering techniques by lowering the spread of observations (RMSE), but the amplitude is unchanged. Similar to HAUC, the observations show a decline in early 2020 due to snow load.

4.3.7 Results on MAUC

As observed in Fig. 4.20, a significant and distinct seasonal signal is evident in H_{GNSS}, characterised by an increase in height during winter. The periodic signal does not vanish with load or common mode filtering; however, the amplitude becomes less pronounced. The presence of a periodic signal in $H_{CM,L}$ implies that an

unmodelled signal is left within the observations.

As observed in Table 4.19, the Bernese results of $H_{GNSS} - L$ display a 5% decrease, indicating that the modelled loading effect of Synsenvatnet constitutes a part of the annual periodic signal, albeit to a limited extent. This also aligns well with the GAMIT/GLOBK solution presented in the same table, further suggesting this is the case. However, the primary portion of the amplitude reduction is attributed to the common mode filtering. As a result, it indicates that the remaining annual periodic signal in the dataset is associated with the PGS or a smaller region rather than modelled hydrological loading or a common signal in the network. A similar increase in amplitude is evident in DGLS and OSTC, which are neighbouring PGSs to MAUC, respectively, to the north and east. This may imply a delimited regional signal.

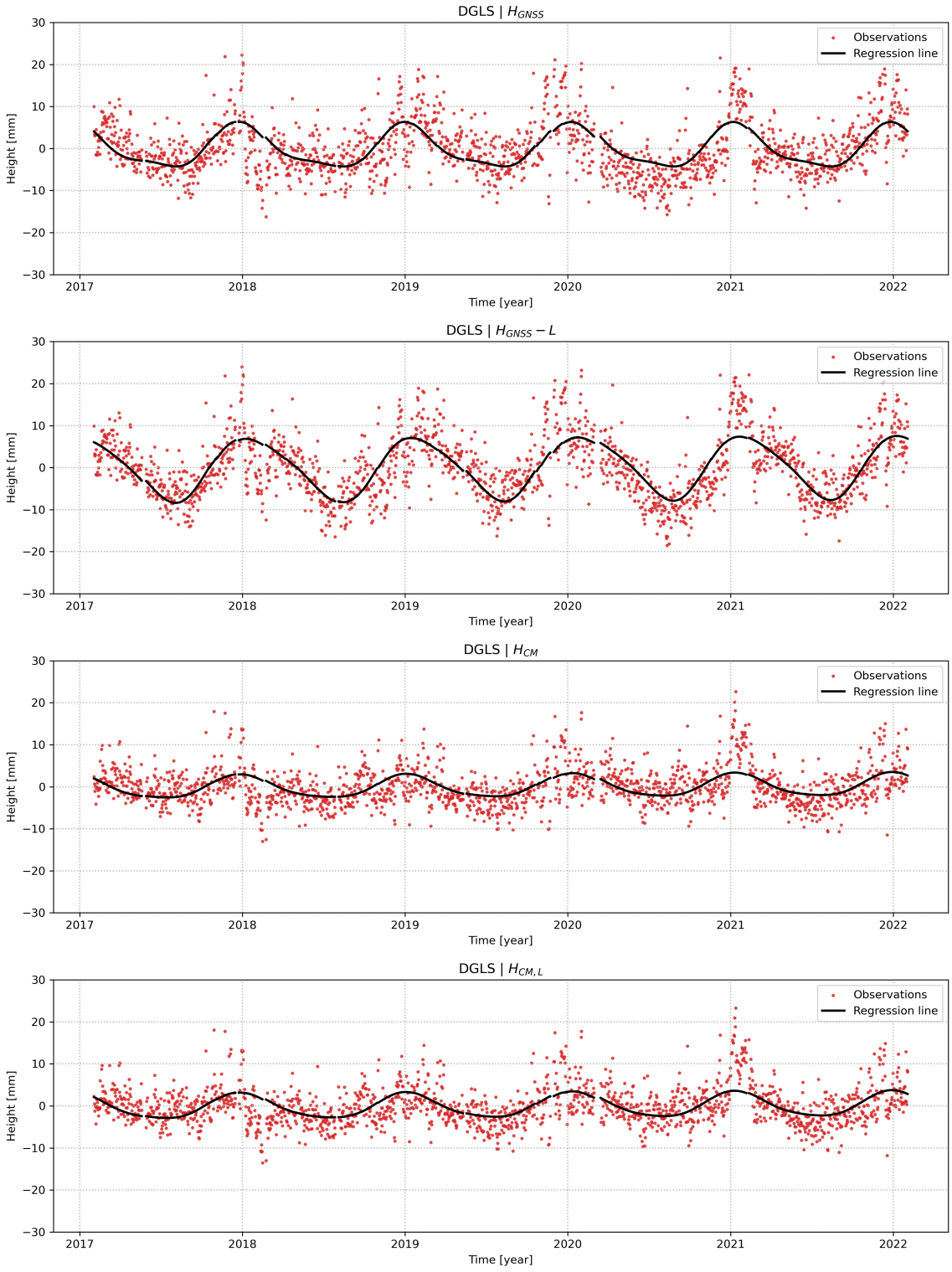

Figure 4.14: The GPS observations at DGLS and the regression line. H_{GNSS} represents the unfiltered time series, whereas $H_{\mathrm{GNSS}} - L$ corresponds to the unfiltered time series with the loading effect subtracted. H_{CM} refers to the common mode-filtered time series based on H_{GNSS}, and $H_{\mathrm{CM,L}}$ refers to the common mode-filtered time series applied to $H_{\mathrm{GNSS}} - L$.

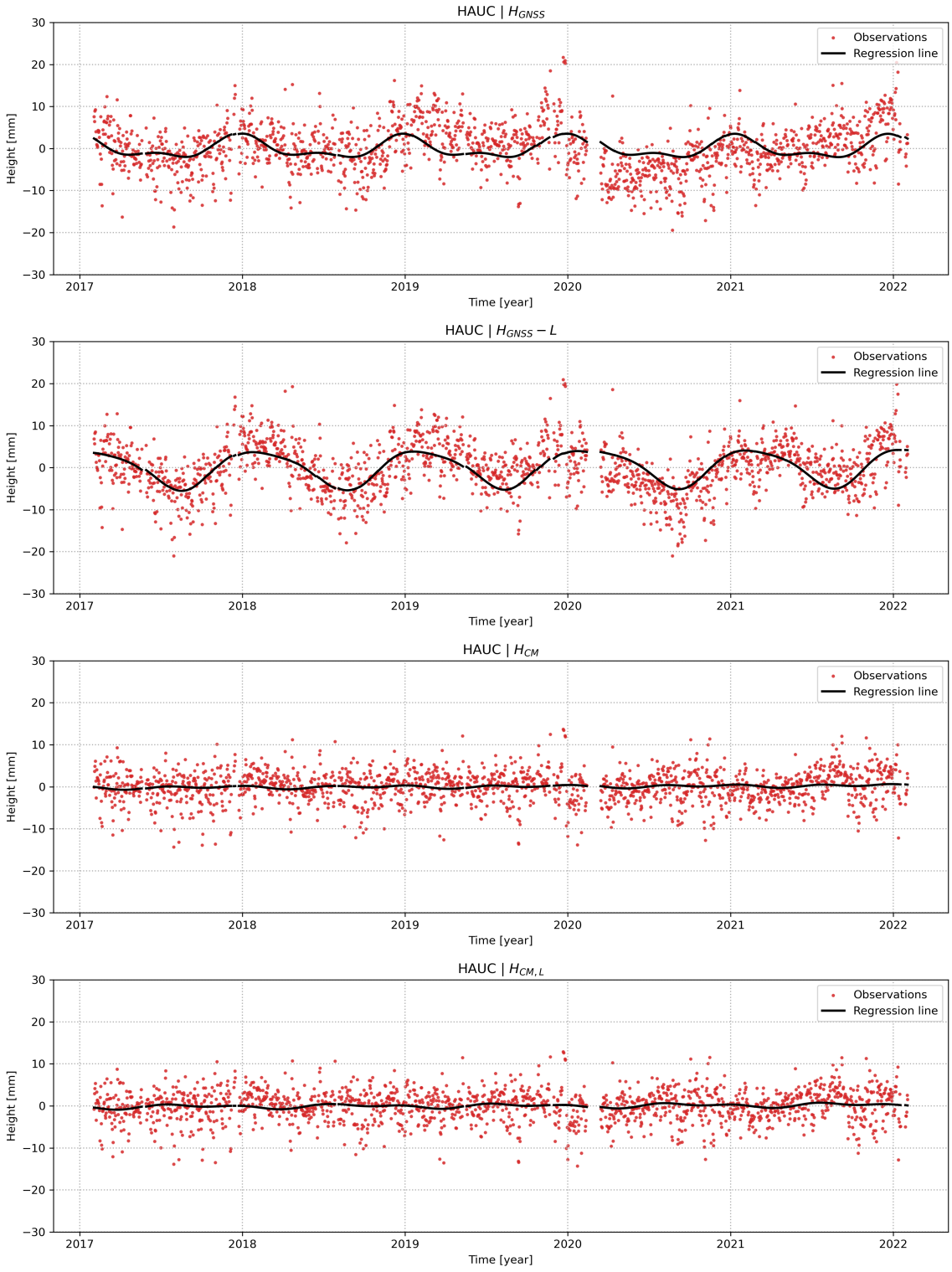

Figure 4.15: The GPS observations at HAUC and the regression line. H_{GNSS} represents the unfiltered time series, whereas $H_{\mathrm{GNSS}} - L$ corresponds to the unfiltered time series with the loading effect subtracted. H_{CM} refers to the common mode-filtered time series based on H_{GNSS}, and $H_{\mathrm{CM,L}}$ refers to the common mode-filtered time series applied to $H_{\mathrm{GNSS}} - L$.

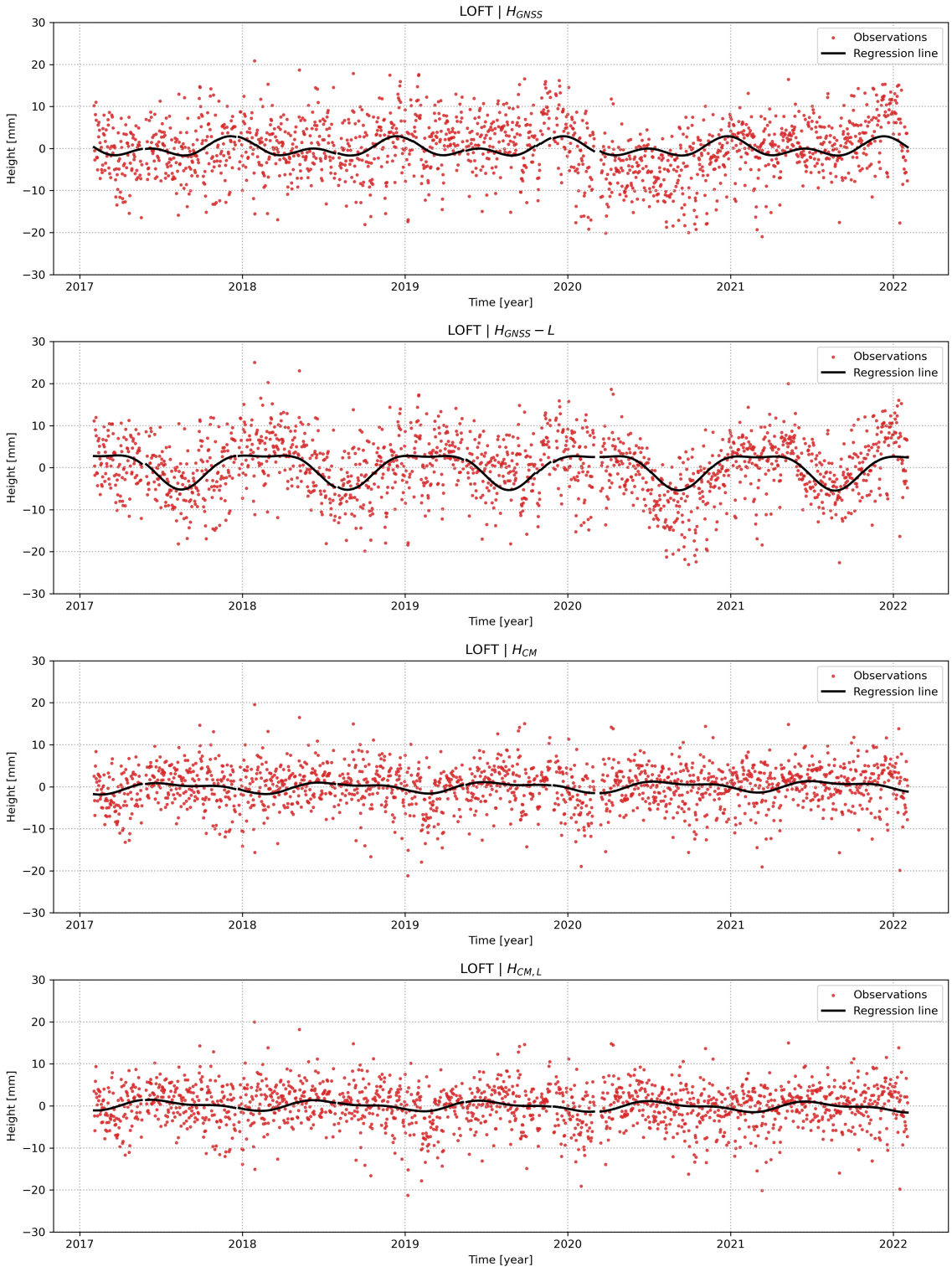

Figure 4.16: The GPS observations at LOFT and the regression line. H_{GNSS} represents the unfiltered time series, whereas $H_{\mathrm{GNSS}} - L$ corresponds to the unfiltered time series with the loading effect subtracted. H_{CM} refers to the common mode-filtered time series based on H_{GNSS}, and $H_{\mathrm{CM,L}}$ refers to the common mode-filtered time series applied to $H_{\mathrm{GNSS}} - L$.

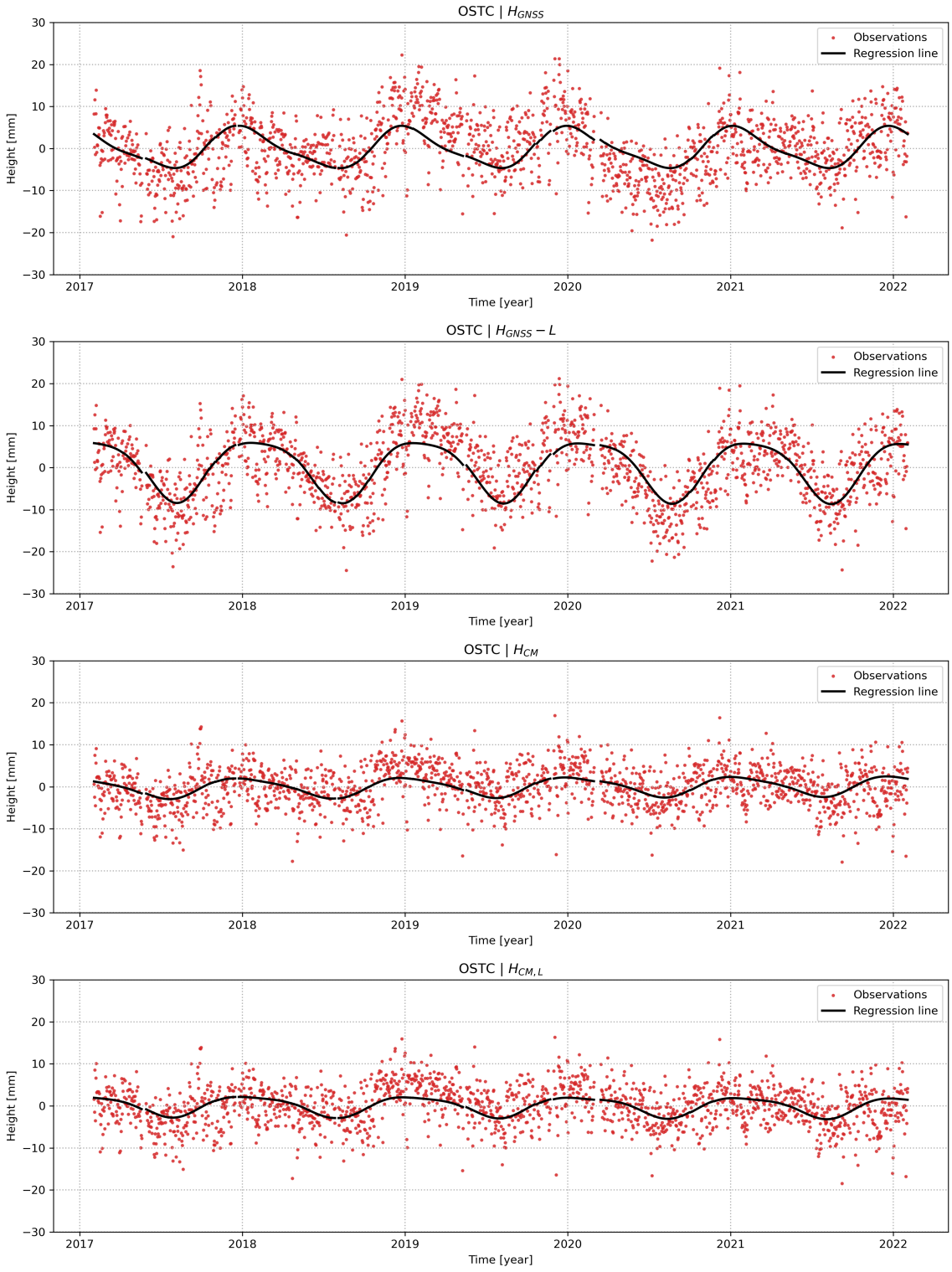

Figure 4.17: The GPS observations at OSTC and the regression line. H_{GNSS} represents the unfiltered time series, whereas $H_{\mathrm{GNSS}} - L$ corresponds to the unfiltered time series with the loading effect subtracted. H_{CM} refers to the common mode-filtered time series based on H_{GNSS}, and $H_{\mathrm{CM,L}}$ refers to the common mode-filtered time series applied to $H_{\mathrm{GNSS}} - L$.

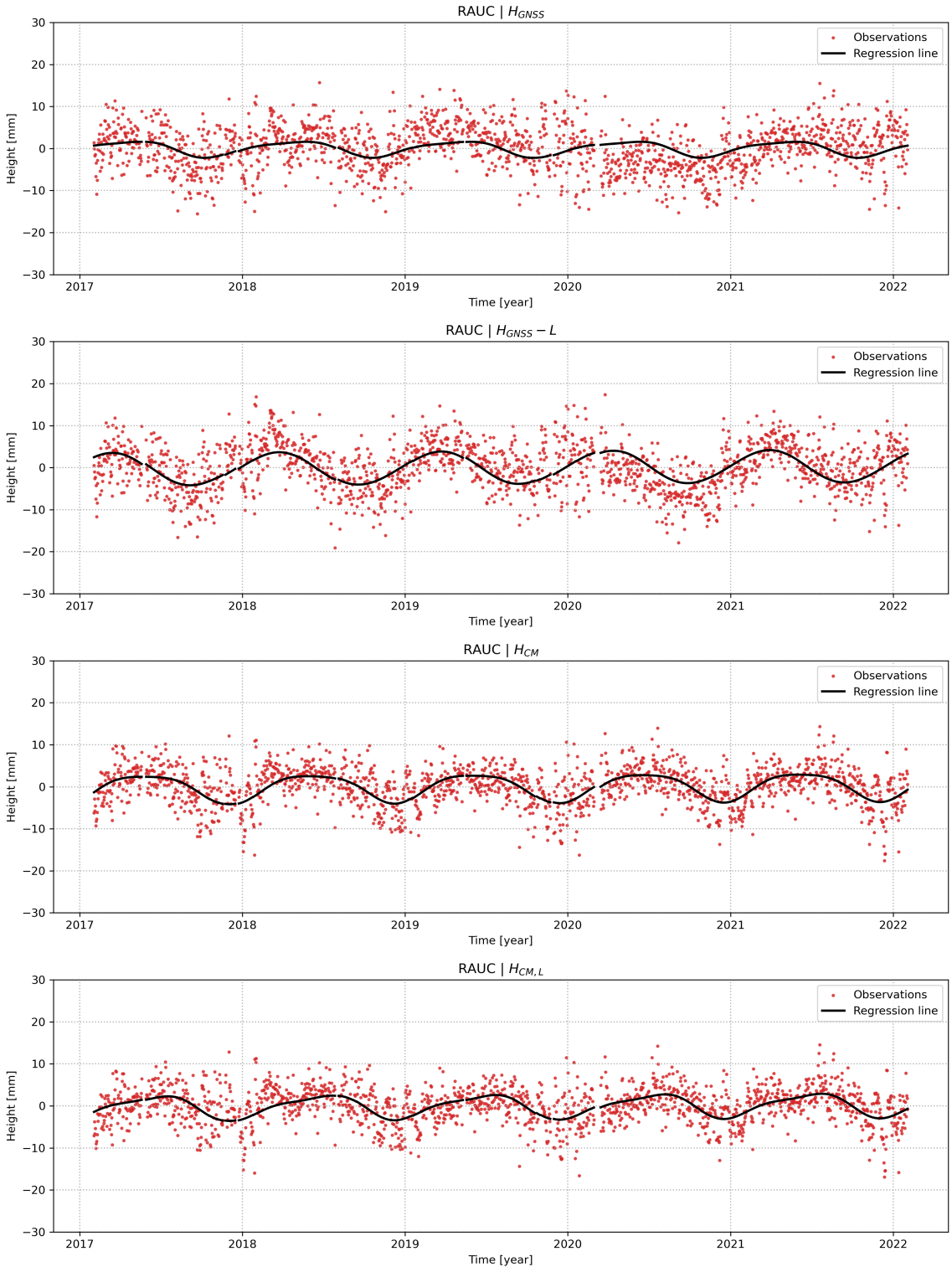

Figure 4.18: The GPS observations at RAUC and the regression line. H_{GNSS} represents the unfiltered time series, whereas $H_{\mathrm{GNSS}} - L$ corresponds to the unfiltered time series with the loading effect subtracted. H_{CM} refers to the common mode-filtered time series based on H_{GNSS}, and $H_{\mathrm{CM,L}}$ refers to the common mode-filtered time series applied to $H_{\mathrm{GNSS}} - L$.

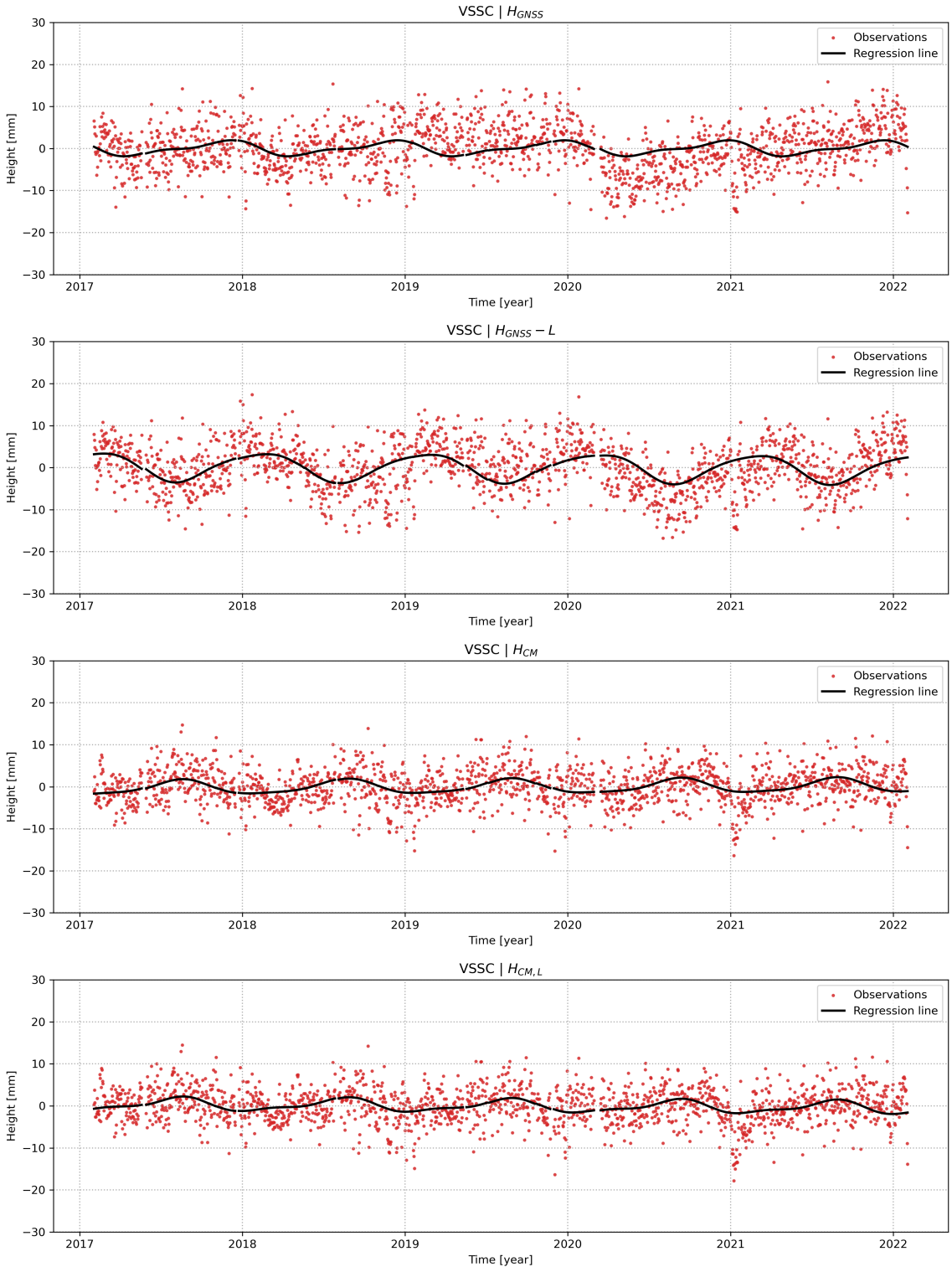

Figure 4.19: The GPS observations at VSSC and the regression line. H_{GNSS} represents the unfiltered time series, whereas $H_{\mathrm{GNSS}} - L$ corresponds to the unfiltered time series with the loading effect subtracted. H_{CM} refers to the common mode-filtered time series based on H_{GNSS}, and $H_{\mathrm{CM,L}}$ refers to the common mode-filtered time series applied to $H_{\mathrm{GNSS}} - L$.

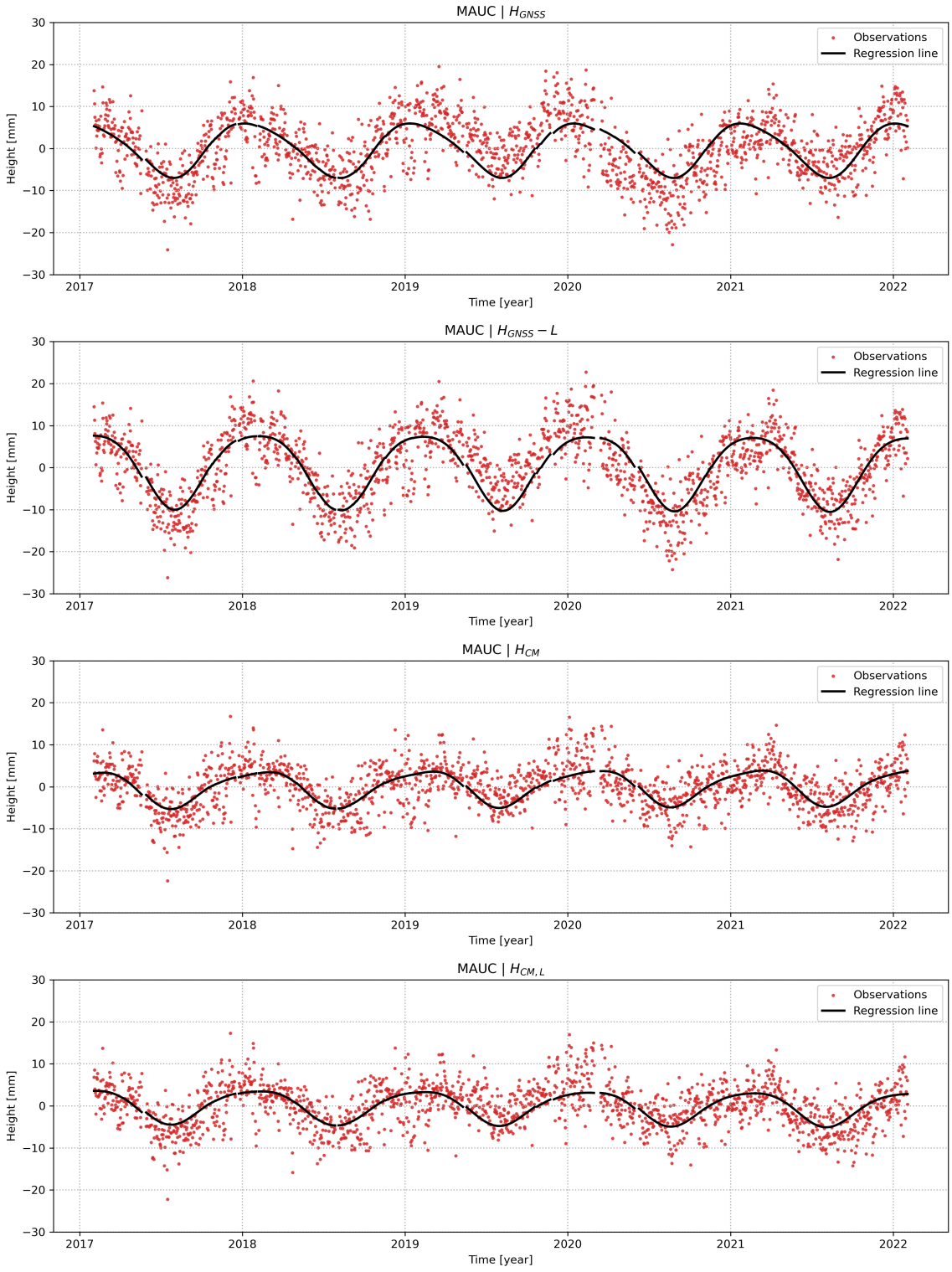

Figure 4.20: The GPS observations at MAUC and the regression line. H_{GNSS} represents the unfiltered time series, whereas $H_{\mathrm{GNSS}} - L$ corresponds to the unfiltered time series with the loading effect subtracted. H_{CM} refers to the common mode-filtered time series based on H_{GNSS}, and $H_{\mathrm{CM,L}}$ refers to the common mode-filtered time series applied to $H_{\mathrm{GNSS}} - L$.

4.4 Summary of results

In the unfiltered time series H_{GNSS}, all PGSs, excluding RAUC, display a notable uplift during the winter months, reaching a peak around the year's end. This is consistent for all network and software solutions.

Removing the load signal $H_{GNSS} - L$ derived from the water reservoirs similarly impacts PGSs in proximity to such reservoirs across all network solutions. This is shown by a slight increase in the annual amplitude observed at HAUC and OSTC, coupled with a decrease in the annual amplitude at MAUC. Interestingly, the Bernese L2 solution shows a 32% reduction in RAUC, seen in Table 4.12, a change not mirrored in the GAMIT/GLOBK solution (Table 4.16). The uniform decrease in the annual amplitude seen in MAUC across all network solutions implies that changes in water levels in the nearby reservoir (Sysenvatnet) account for a small proportion of the seasonal vertical displacement observed at this PGS. However, the effect of water level fluctuations at Sysenvatnet on the annual amplitude of MAUC is marginal, with the Bernese solution showing a maximum reduction of merely 5% (Table 4.4).

Removing the load signal $H_{GNSS} - L$ derived from hydrological changes and water reservoirs does affect all network solutions similarly, with a clear rise observed in the amplitude and a slight reduction in RMSE. For the Bernese solution, the amplitude displays an average rise of 73% (Table 4.1), while the GAMIT/GLOBK solutions exhibit an average rise of 56% (Table 4.13). The findings indicate that the hydrological load suppresses a larger unmodelled seasonal signal in the region, thus not part of the seasonal signal affecting the PGSs. This aligns well with the comparison between the load signal and GPS observations, as depicted in Fig. 4.10. The figure demonstrates a phase shift between the load signal and the GPS observations.

The solutions derived from the Bernese software, which incorporated atmospheric, hydrological, and water reservoir loadings, demonstrated variance from other network solutions when the load signal was removed from the GPS observation. This resulted in an increase in both the RMSE and amplitude. However, the rise in amplitude was relatively less significant compared to other solutions, as indicated in Tables 4.1 and 4.5. The Bernese solution, factoring solely the elastic load emanating from water reservoirs and ATML, suggests that the removal of the load signal reduces the amplitude for all PGS, except for RAUC, by an average of 25% (Table 4.7). Conversely, the RMSE has an average increase of 8%. This indicates that the ATML could potentially contribute to the observed seasonal signal.

Common mode filtering attenuates the annual periodic signal within the network, except for RAUC, regardless of the software or network solution employed. Depending on the network solutions, the application of common mode filtering results in an average annual amplitude reduction ranging between 24% and 37%. Furthermore, common mode filtering uncovers a consistent annual periodic signal of equal magnitude at DGLS and OSTC, persisting across all networks. This signal is also present at MAUC, albeit with a greater amplitude. Of greater significance, the signal considerably influences the observations more than the modelled deformation effect of the proximate water reservoir at MAUC. Thus, even if removing the loading signal attributed to the water reservoir will have a marginally positive impact on the seasonal amplitude, it pales compared to the unmodelled signal. The results also indicate that either the network solution reduces the hydrological loading effect on the PGSs or that the loading signal suppresses an unmodelled signal. The findings further suggest that implementing a loading model, be it hydrological or atmospheric, may not be crucial for a network of this scale and with similar loads impacting the area since both common mode solutions, H_{CM} and $H_{CM,L}$, give very similar results. This indicates that only local deformation effects, such as those caused by water reservoirs, must be modelled.

The software employed to process the GPS observations can result in discrepancies concerning the influence of local deformation effects. The Bernese software demonstrates a 32% reduction at RAUC in the $H_{GNSS} - L$, while GAMIT/GLOBK exhibits no impact. Both solutions display similar outcomes for MAUC, which is located close to a sizeable reservoir. The overarching conclusion reveals that the disparities between the software after common mode filtering are negligible.

The comparison of variances across time series reveals a significant disparity between the unfiltered series and those subjected to common mode filtering correction.

Chapter 5

Discussion

5.1 Loading models

The hydrological data acquired from NVE are based on estimation, predictions, and interpolated values and will therefore exhibit a degree of uncertainty. However, the data will indicate what influence that can be expected for the amount of water stored over the land area. Even a rough estimation of the hydrological load may contribute to improved results.

In addition, the total water storage in the region was not included in the study, partly because the data is not directly available by NVE and partly because it was assumed that the snow load, groundwater, and soil moisture are the hydrological effects of the greatest impact. In order to determine the total water storage in the region, a summation of all involved factors, such as precipitation, snowmelt, evaporation and runoff, can then be adapted to a linear regression model or a polynomial function, where the trend in the model then determines the total water flow (Bramanto, 2022). Including the total amount of water could eventually explain the phase shift between the estimated hydrological load and the vertical GPS time series. As discussed in the results, the loading deformation due to soil moisture content (SMC) is substantial. At the PGS MAUC, it causes a deformation of 4 mm, i.e., if it is incorrectly predicted, it can impact the results. The model used in this thesis, assuming 30% porosity for all surfaces and using a global soil thickness model, is a crude estimation.

The data concerning water reservoir volumes, obtained from www.sildre.no, exhibits an uncertain quality but is accepted at a nominal value. Nonetheless, similar to

hydrological data, it suggests potential volume variations. A more critical issue is the imprecise modelling area of each reservoir in the absence of aerial imagery for the low water area extent. The assumption is that the area related to the volume change is just a smaller shape than the original reservoir, and assuming that the volume is constant in this smaller shape, thus neglecting the reservoir bathymetric features, is an unrefined model. While this method may be appropriate for larger reservoirs at a certain distance from the PGS, it could be deemed overly simplistic for smaller ones, particularly when the PGS is in close proximity to the reservoir. This is the situation at HAUC, where the PGS is roughly 200 metres from the nearest reservoir, and significant mass changes at this distance could substantially impact vertical deformation. The oversimplification of the reservoir and assumption of uniform volume changes might explain why the load model at this PGS does not align with the GPS observations.

5.2 PGS Network

The decision to include the PGSs only in the vicinity of MAUC was influenced by the work of (Wdowinski et al., 1997), which involved a compact network of PGSs surrounding a PGS under investigation. Nonetheless, by adopting an approach with a broader network of PGSs, incorporating some with known stable and high-quality time series, this would reinforce the network and yield more dependable results. It is important to remember that the purpose of the network is to capture common signals and, with common mode filtering, reduce network errors in order to determine the effects of the water reservoirs or other loading effects.

Since the network is small, it is difficult to determine if a local effect is present, affecting PGSs such as DGLS, OSTC, and MAUC, or if the phenomenon is only related to the PGSs. To examine the stability of the network, a script was created to determine the most favourable outcome for MAUC, presented in Table 5.1. The network only includes the PGSs with a distinctive annual amplitude present, namely DGLS and OSTC. As presented in the previous chapter, this results in a much better amplitude reduction than the other network solutions, with a seasonal amplitude for MAUC of 1.5 mm but with lower RMSE reduction. However, it is challenging to discern whether these PGSs are affected by a similar local source of deformation or merely have similar issues regarding other error sources, such as multipath. With a broader network, it may have been possible to determine if other neighbouring

stations to DGLS and OSTC exhibit a similar signal not relating to a modelled hydrological load.

Table 5.1: The Bernese solution for a network solution focused on the best possible solution for MAUC regarding reducing the amplitude, only including PGSs MAUC, DGLS, and OSTC. L denoting the loading signal derived from water reservoir loadings. Displayed are the annual RMSE, amplitude, and amplitude's standard deviation. The variations in RMSE and amplitude are relative to H_{GNSS}. H_{GNSS} represents the unfiltered time series, whereas $H_{\mathrm{GNSS}} - L$ corresponds to the unfiltered time series with the loading effect subtracted. H_{CM} refers to the common mode-filtered time series based on H_{GNSS}, and $H_{\mathrm{CM,L}}$ refers to the common mode-filtered time series applied to $H_{\mathrm{GNSS}} - L$.

PGS		RMS (mm)	RMS diff (%)	Amp (mm)	Amp std (mm)	Amp diff (%)
DGLS						
	H_{GNSS}	5.4		4.9	+/-0.2	
	$H_{\mathrm{GNSS}} - L$	5.4	0	4.9	+/-0.2	0
	H_{CM}	3.4	-37	0.2	+/-0.2	-96
	$H_{\mathrm{CM,L}}$	3.4	-37	0.2	+/-0.3	-96
MAUC						
	H_{GNSS}	5.6		6.3	+/-0.2	
	$H_{\mathrm{GNSS}} - L$	5.6	0	6.0	+/-0.2	-5
	H_{CM}	4.9	-13	2.4	+/-0.2	-62
	$H_{\mathrm{CM,L}}$	4.9	-13	1.5	+/-0.2	-76
OSTC						
	H_{GNSS}	6.4		4.6	+/-0.2	
	$H_{\mathrm{GNSS}} - L$	6.4	0	4.6	+/-0.2	0
	H_{CM}	3.4	-47	0.2	+/-0.2	-96
	$H_{\mathrm{CM,L}}$	3.4	-47	0.2	+/-0.2	-96

5.3 GPS time series

The GNSS time series are correlated, meaning that the data points collected during the time frame exhibit a relationship or association with each other. This implies that the measurement errors are not independent but exhibit a systematic relationship over time. Consequently, the uncertainty in the position estimates can be artificially reduced, making the results appear better than they actually are. To mitigate the impact of correlated errors on GNSS position estimates is possible by adding noise models to obtain more reliable results. Software like Hector (Bos et al., 2013) can be used to analyse the time series and add noise. This method was not used in the thesis. Instead, all analyses were based on a linear unweighted least

squares regression model. To evaluate potential disparities between the time series processed by Hector and the original data, the unfiltered H_{GNSS} time series from the GAMIT/GLOBK solution was processed through the Hector software, incorporating both white and flicker noise. The comparative results of these operations are presented in Table 5.2. It displays the original unfiltered H_{GNSS} time series derived from GAMIT/GLOBK, and its counterpart processed through Hector software (undertaken by NMA), with the added noise components. Although the annual seasonal amplitudes appear similar across both solutions, there is a noticeable difference in the magnitude of standard deviations to the amplitudes. These deviations are significantly larger in the series subjected to the noise model, which could influence the outcome of a statistical test to determine whether there is a significant difference between unfiltered time series and those filtered via common mode, with or without the removal of the loading signal. Utilising software like Hector would give the study more overall reliable results.

Table 5.2: A comparison between two GAMIT/GLOBK solutions processed either through an unweighted linear regression or the Hector software, with added white and flicker noise. H_{GNSS} represents unfiltered GPS time series, (WH) denotes White noise, and (FL) denotes Flicker noise.

PGS	H_{GNSS} Amp (mm)	H_{GNSS} Amp std (mm)	H_{GNSS} WH & FL Amp (mm)	H_{GNSS} WH & FL Amp std (mm)
HAUC	2.7	+/-0.3	2.6	+/-0.9
LOFT	1.9	+/-0.3	2.0	+/-0.8
MAUC	5.0	+/-0.3	4.8	+/-0.8
OSTC	3.4	+/-0.3	3.3	+/-1.0
RAUC	2.4	+/-0.3	2.9	+/-0.9
VSSC	2.4	+/-0.3	2.5	+/-0.8

5.4 Common Mode filtering

The common mode filtering employed in this study is a rudimentary approach that does not account for spatial resolution or the formal error associated with each observation. This method presumes a uniform spatial response to common mode errors, implying that the errors are identical for all PGSs. Nonetheless, as discussed in Chapter 2, alternative stacking methodologies, which assign weight to the observations, could have been implemented. An elementary inverse distance weighting method was examined but ultimately deemed to give inconclusive results and, thus, not incorporated into the thesis. Due to constraints in the Bernese dataset, which

does not provide standard deviations for each observation, the study did not include a method that weights each observation based on its uncertainty. Nevertheless, this approach could have been applied to the GAMIT/GLOBK datasets as an extra analysis.

5.5 Further work

This subchapter concentrates on additional research avenues based on the findings of this study. The primary objective of this study was to determine whether the seasonal vertical displacements at MAUC could be attributed to loading effects, either from the nearby water reservoir or hydrological effects. Given that none of the loading models assessed can account for the seasonal variations observed at MAUC, this subchapter discusses alternative directions for future studies. The occurrence of such behaviour in PGSs located in mountainous regions, such as rising during winter months and deforming during summer, is not unprecedented and has been documented in a recent paper (Pintori et al., 2022).

Pintori proposes several potential explanations for the observed phenomenon, including unmodelled hydrological effects, soil freezing, or ice formations within and on the antenna mount (Koulali & Clarke, 2020). Unmodulated hydrological effects might potentially be identified if the total water storage was determined. Frost heaving could contribute; however, according to the NMA, the antenna is mounted on bedrock, rendering this cause improbable. Ice formations within and on the antenna present an intriguing line of inquiry.

Several studies (Dill & Dobslaw, 2013; Steigenberger et al., 2009; Tregoning & Watson, 2009) suggest that the tropospheric delay model adopted in this study, WM1, has the potential to inject an artificial seasonal signal. This proposition might be reinforced given that the seasonal displacements observed at MAUC are in phase with atmospheric loading, as demonstrated in Figure 4.12. Since atmospheric loading variations align with meteorological alterations, they are inherently linked to the tropospheric delay.

Additionally, as previously mentioned, multipath effects due to snow (Larson, 2016) can induce uplift during winter. Multipath effects are related to the elevation angle utilised by the GNSS receiver. Specifically, lower elevation angles imply extended signal paths through the atmosphere and augment the probability that the signal

will reflect off objects or the ground before it reaches the receiver, thereby increasing the potential for multipath errors. Consequently, as the elevation angle diminishes, the probability of multipath errors increases.

Further examination of the phenomenon's distribution would be of interest. Is there a common characteristic among the PGSs exhibiting this type of behaviour? A GPS solution independent of a network, such as a Precise Point Positioning (PPP) solution, would also be of interest to determine whether the issue is associated with the network and if the observed displacements exhibit the same magnitude.

Chapter 6

Conclusions

The main purpose of this thesis is to analyse and find answers to the following questions:

- Do the vertical fluctuations at MAUC or other PGSs result from mass load deformation?
- How severe is the deformation of the mass loads related to water reservoirs, and should PGSs be located in the proximity of reservoirs, as Sysenvatnet?

To address these questions, the GPS time series from a network of PGSs were filtered for loading and common mode signals. The loading signal incorporated hydrological loadings such as SWE, GWT, and SMC, along with the load effects of water reservoirs in the vicinity of the PGSs in the network. This was achieved by acquiring data from NVE to determine the amount of water stored in land areas in southern Norway. Green's function for crustal deformation was utilised to determine the loading effect on each PGS. The GPS time series, provided by NMA and processed using Bernese and GAMIT/GLOBK software, were employed in this study. The common mode signal was ascertained via a network of PGSs surrounding MAUC.

The findings indicated that the hydrological loading signal neither aligned with the magnitude nor the phase of the observed elevation fluctuations in the GPS time series. Nonetheless, subtracting the loading signal increased the seasonal amplitude and reduced the RMSE, suggesting that the loading effect suppresses a larger unmodelled signal. Common mode filtering, based on the entire network, reduced the seasonal amplitude observed at MAUC and other PGSs exhibiting similar tendencies

but did not eliminate it entirely. Smaller vertical fluctuations were also present at neighbouring PGSs to MAUC, implying either a local unmodelled signal in the area or shared errors among these PGSs, potentially resulting in a vertical rise in GPS observations during winter, such as multipath or ice formations in the antenna. The deformation impact of water reservoirs was only conclusively observed at MAUC, demonstrating a decrease in amplitude in both software solutions. This confirms that the reservoir only marginally is the cause of the seasonal displacement, but its magnitude is negligible compared to other hydrological loading signals and the seasonal signal.

Based on these considerations, it can therefore be concluded that: Vertical fluctuations observed at MAUC do not stem from modelled hydrological loadings signals in the region and that the nearby reservoir is only marginally responsible. Further, the deformation effects caused by water reservoirs studied in this area are not significant enough to pose a genuine concern, as their impact is minor compared to other loading effects. Nevertheless, considering that their deformation impact diminishes with distance (due to its localised effect) and modelling them accurately requires bathymetric data, it would be prudent to avoid locating future PGS installations in close proximity to water reservoirs as a precautionary measure.

References

Beldring, S., Engeland, K., Roald, L. A., Sælthun, N. R., & Voksø, A. (2003). Estimation of parameters in a distributed precipitation-runoff model for Norway. *Hydrology and Earth System Sciences*, *7*(3), 304–316.

Bergström, S., et al. (1995). The HBV model. *Computer models of watershed hydrology.*, 443–476.

Bos, M., Fernandes, R., Williams, S., & Bastos, L. (2013). Fast error analysis of continuous GNSS observations with missing data. *Journal of Geodesy*, *87*(4), 351–360.

Bos, M., & Scherneck, H.-G. (2013). Computation of Green's functions for ocean tide loading. In *Sciences of geodesy-ii* (pp. 1–52). Springer.

Bramanto, B., Breili, K., Gerlach, C., Ophaug, V., & Gjevestad, J. (2022). Reducing hydrological disturbances in absolute gravity observations by combining global hydrological models with a regional run-off model. *Geophysical Journal International*, *230*(2), 976–994.

Dach, R., Hugentobler, U., Fridez, P., & Meindl, M. (2007). Bernese GPS Software Version 5.0, Astronomical Institute. *University of Bern, Switzerland.*

Darwin, G. (1882). XLVI. On variations in the vertical due to elasticity of the earth's surface. *The London, Edinburgh, and Dublin Philosophical Magazine and Journal of Science*, *14*(90), 409–427.

Dill, R., & Dobslaw, H. (2013). Numerical simulations of global-scale high-resolution hydrological crustal deformations. *Journal of Geophysical Research: Solid Earth*, *118*(9), 5008–5017.

Dong, D., Fang, P., Bock, Y., Webb, F., Prawirodirdjo, L., Kedar, S., & Jamason, P. (2006). Spatiotemporal filtering using principal component analysis and Karhunen-Loeve expansion approaches for regional GPS network analysis. *Journal of geophysical research: solid earth*, *111*(B3).

Dziewonski, A. M., & Anderson, D. L. (1981). Preliminary reference Earth model. *Physics of the earth and planetary interiors*, *25*(4), 297–356.

Farrell, W. (1972). Deformation of the Earth by surface loads. *Reviews of Geophysics*, *10*(3), 761–797.

Gruszczynski, M., Klos, A., & Bogusz, J. (2016). Orthogonal transformation in extracting of common mode errors from continuous GPS networks. *Acta Geodynamica et Geomaterialia*, *13*(3), 291–298.

Herring, T., King, R., Floyd, M., & McClusky, S. (2018). Introduction to GAMIT/-GLOBK. Release 10.7. Technical Report. Massachusetts Institute of Technology.

Hofmann-Wellenhof, B., Lichtenegger, H., & Wasle, E. (2007). *GNSS–global navigation satellite systems: GPS, GLONASS, Galileo, and more*. Springer Science & Business Media.

Hofmann-Wellenhof, B., & Moritz, H. (2006). *Physical geodesy*. Springer Science & Business Media.

Jentzsch, G. (1997). Earth tides and ocean tidal loading. *Tidal phenomena*, 145–171.

Kierulf, H. P., van Pelt, W., Petrov, L., Dähnn, M., Kirkvik, A., & Omang, O. (2022). Seasonal glacier and snow loading in Svalbard recovered from geodetic observations. *Geophysical Journal International*, *229*(1), 408–425.

Koulali, A., & Clarke, P. (2020). Effect of antenna snow intrusion on vertical GPS position time series in Antarctica. *Journal of Geodesy*, *94*(10), 101.

Lantmäteriet. (2023). *Distance measurement with code*. Retrieved March 28, 2023, from https://www.lantmateriet.se/en/geodata/gps-geodesi-och-swepos/gps-and-satellite-positioning/methods-for-gnss-measurement/distance-measurement-with-code/

Larson, K. M. (2016). GPS interferometric reflectometry: applications to surface soil moisture, snow depth, and vegetation water content in the western United States. *Wiley Interdisciplinary Reviews: Water*, *3*(6), 775–787.

Liu, B., Dai, W., Peng, W., & Meng, X. (2015). Spatiotemporal analysis of GPS time series in vertical direction using independent component analysis. *Earth, Planets and Space*, *67*(1), 1–10.

Nikolaidis, R. (2002). *Observation of geodetic and seismic deformation with the Global Positioning System*. University of California, San Diego.

Nordman, M., Mäkinen, J., Virtanen, H., Johansson, J. M., Bilker-Koivula, M., & Virtanen, J. (2009). Crustal loading in vertical GPS time series in Fennoscandia. *Journal of Geodynamics*, *48*(3-5), 144–150.

Pagiatakis, S. D., et al. (1982). *Ocean tide loading, body tide and polar motion effects on very long baseline interferometry*. Department of Surveying Engineering, University of New Brunswick Fredericton.

Pagiatakis, S. D. (1990). The response of a realistic earth to ocean tide loading. *Geophysical Journal International*, *103*(2), 541–560.

Pelletier, J. D., Broxton, P. D., Hazenberg, P., Zeng, X., Troch, P. A., Niu, G.-Y., Williams, Z., Brunke, M. A., & Gochis, D. (2016). A gridded global data set of soil, intact regolith, and sedimentary deposit thicknesses for regional and global land surface modeling. *Journal of Advances in Modeling Earth Systems*, *8*(1), 41–65.

Petrov, L., & Boy, J.-P. (2004). Study of the atmospheric pressure loading signal in very long baseline interferometry observations. *Journal of geophysical research: solid earth*, *109*(B3).

Pintori, F., Serpelloni, E., & Gualandi, A. (2022). Common-mode signals and vertical velocities in the greater Alpine area from GNSS data. *Solid Earth*, *13*(10), 1541–1567.

PROJ contributors. (2023). *PROJ coordinate transformation software library. Open Source Geospatial Foundation* [(last visited Mars 2023)]. https://proj.org/

Steigenberger, P., Boehm, J., & Tesmer, V. (2009). Comparison of GMF/GPT with VMF1/ECMWF and implications for atmospheric loading. *Journal of Geodesy*, *83*, 943–951.

Torge, W., & Müller, J. (2012). Geodesy. In *Geodesy*. de Gruyter.

Tregoning, P., & Watson, C. (2009). Atmospheric effects and spurious signals in GPS analyses. *Journal of Geophysical Research: Solid Earth*, *114*(B9).

van Dam, T., & Wahr, J. (1998). Modeling environment loading effects: A review. *Physics and Chemistry of the Earth*, *23*(9-10), 1077–1087.

van Dam, T., Wahr, J., Milly, P., Shmakin, A., Blewitt, G., Lavallée, D., & Larson, K. (2001). Crustal displacements due to continental water loading. *Geophysical Research Letters*, *28*(4), 651–654.

Wdowinski, S., Bock, Y., Zhang, J., Fang, P., & Genrich, J. (1997). Southern California permanent GPS geodetic array: Spatial filtering of daily positions for estimating coseismic and postseismic displacements induced by the 1992 Landers earthquake. *Journal of Geophysical Research: Solid Earth*, *102*(B8), 18057–18070.

White, A. M., Gardner, W. P., Borsa, A. A., Argus, D. F., & Martens, H. R. (2022). A review of GNSS/GPS in hydrogeodesy: Hydrologic loading applications

and their implications for water resource research. *Water Resources Research*, *58*(7), e2022WR032078.

Williams, S., & Penna, N. (2011). Non-tidal ocean loading effects on geodetic GPS heights. *Geophysical Research Letters*, *38*(9).

Appendices

A

Table A1: Love numbers, Loaded surfaces PREM Earth model. The table, derived from (Pagiatakis, 1990)

n	h'
0	-0.135
1	-0.295
2	-1.007
3	-1.065
4	-1.069
5	-1.103
6	-1.164
7	-1.238
8	-1.313
9	-1.388
10	-1.46
12	-1.6
14	-1.726
16	-1.845
18	-1.952
20	-2.048
25	-2.252
30	-2.411
40	-2.633
50	-2.777
60	-2.88
70	-2.958
80	-3.021
90	-3.077
100	-3.127
120	-3.221
140	-3.312
160	-3.403
180	-3.496
200	-3.59
250	-3.829
300	-4.069
350	-4.32
400	-4.526
800	-5.263
1000	-5.6
2000	-6.186
3000	-6.262
5000	-6.274
10000	-6.274

Table A2: Green's function for vertical displacement is presented in the table. The second column displays values from Pagiatakis (1990), while the third column exhibits values calculated for this thesis. The fourth column illustrates the differences between these values. All values have been normalised $G_{ur} * 10^{12}(R * \Psi)$, where Ψ is in radians.

Ψ, deg	G_{ur} (Pagiatakis, 1990)	G_{ur} this work	ΔG_{ur}
0.000	-42.603	-42.603	0.000
0.001	-42.377	-42.377	0.000
0.010	-40.132	-40.135	-0.003
0.020	-37.704	-37.737	-0.033
0.030	-35.400	-35.449	-0.049
0.040	-33.258	-33.261	-0.003
0.060	-29.522	-29.427	0.095
0.080	-26.523	-26.548	-0.025
0.100	-24.206	-24.290	-0.084
0.150	-20.745	-20.676	0.069
0.200	-19.273	-19.299	-0.026
0.250	-18.557	-18.552	0.005
0.300	-17.583	-17.583	0.000
0.350	-16.517	-16.517	0.000
0.400	-15.649	-15.649	0.000
0.450	-15.083	-15.084	-0.001
0.500	-14.799	-14.799	0.000
0.550	-14.736	-14.738	-0.002
0.600	-14.806	-14.807	-0.001
0.800	-14.642	-14.643	-0.001
1.000	-13.811	-13.812	-0.001
1.200	-12.922	-12.923	-0.001
1.400	-12.022	-12.022	0.000
1.600	-11.310	-11.311	-0.001
1.800	-10.695	-10.696	-0.001
2.000	-10.112	-10.113	-0.001
2.500	-8.708	-8.710	-0.002
3.000	-7.699	-7.701	-0.002
4.000	-6.190	-6.193	-0.003
5.000	-5.243	-5.246	-0.003
6.000	-4.634	-4.637	-0.003
7.000	-4.225	-4.229	-0.004
8.000	-3.949	-3.954	-0.005
9.000	-3.751	-3.756	-0.005

Ψ, deg	G_{ur} (Pagiatakis, 1990)	G_{ur} this work	ΔG_{ur}
10.000	-3.602	-3.608	-0.006
12.000	-3.383	-3.390	-0.007
14.000	-3.189	-3.197	-0.008
16.000	-3.013	-3.022	-0.009
18.000	-2.831	-2.842	-0.011
20.000	-2.642	-2.654	-0.012
25.000	-2.114	-2.129	-0.015
30.000	-1.518	-1.536	-0.018
35.000	-0.892	-0.913	-0.021
40.000	-0.267	-0.290	-0.023
50.000	0.894	0.864	-0.030
60.000	1.720	1.685	-0.035
70.000	2.135	2.093	-0.042
80.000	2.098	2.051	-0.047
90.000	1.667	1.614	-0.053
100.000	0.955	0.896	-0.059
110.000	0.016	-0.049	-0.065
120.000	-1.056	-1.127	-0.071
130.000	-2.184	-2.261	-0.077
140.000	-3.320	-3.403	-0.083
150.000	-4.390	-4.479	-0.089
160.000	-5.319	-5.414	-0.095
170.000	-6.045	-6.145	-0.100
180.000	-6.535	-6.642	-0.107

B

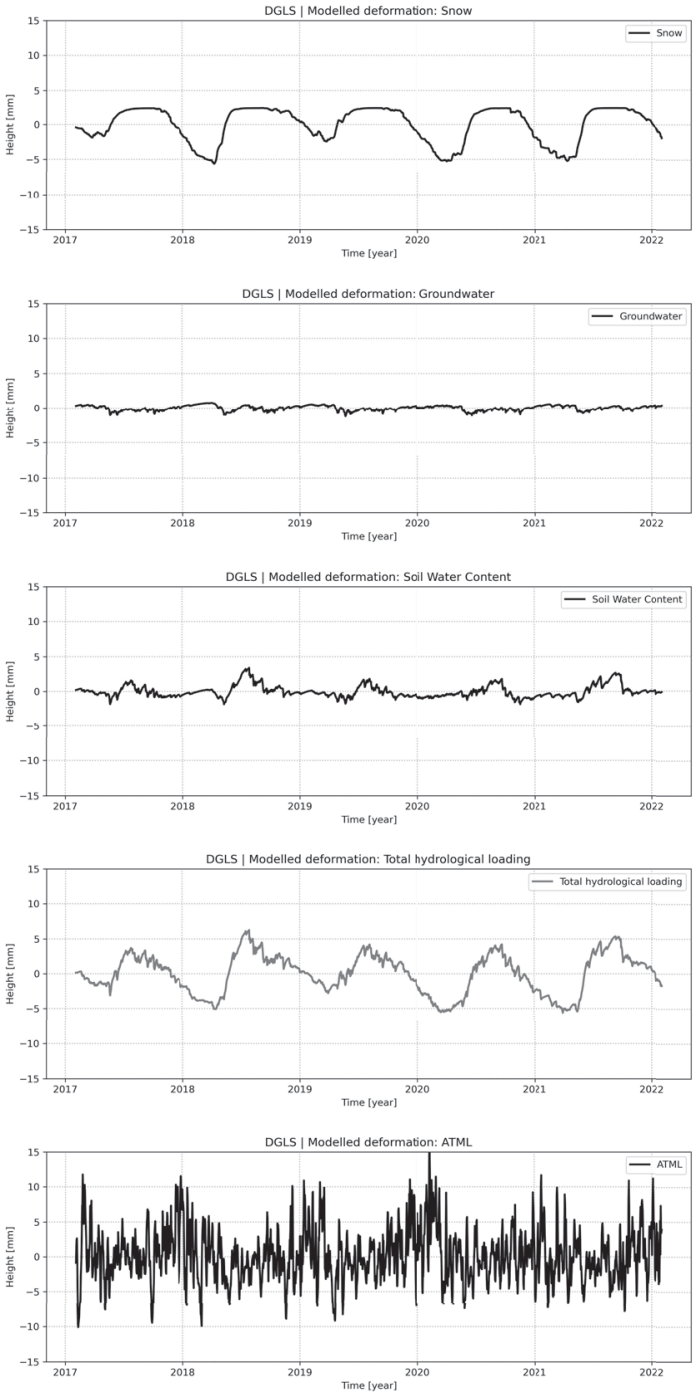

Figure B1: The graphs show the modelled deformation effects for DGLS from above: SWE, GWT, SMC, Total hydrological deformation, and ATML.

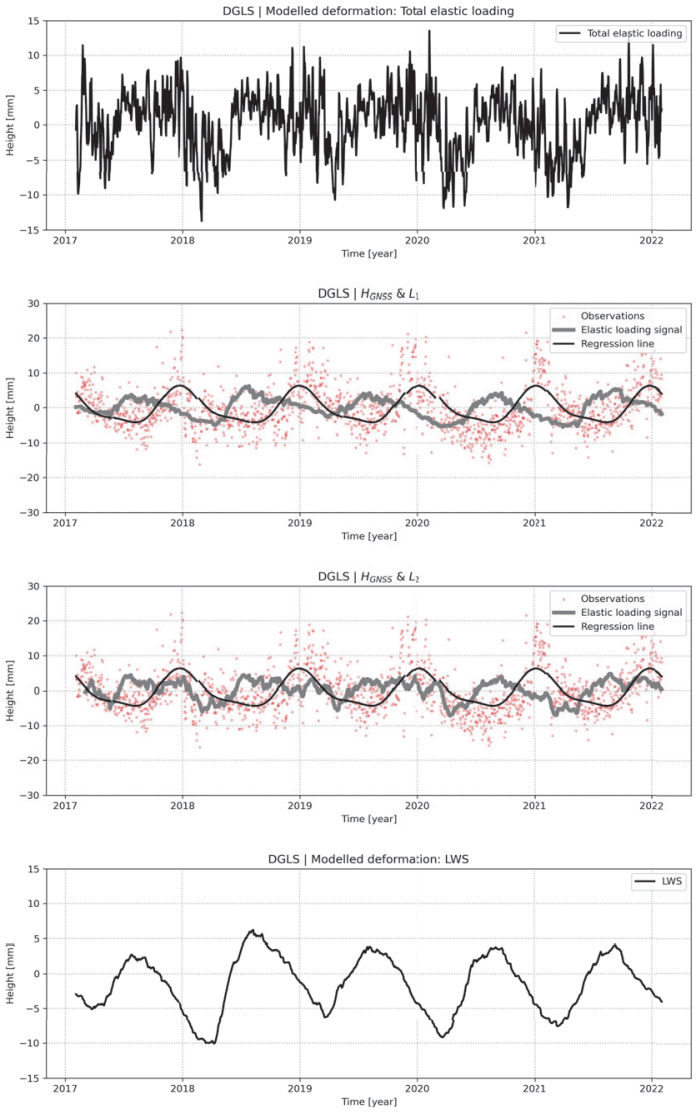

Figure B2: The graphs show the modelled deformation effects for DGLS from above: Total hydrological deformation + ATML; Total hydrological deformation together with GPS observations, and the regression line derived from the GPS observations; Total hydrological deformation + ATML together with GPS observations, and the regression line derived from the GPS observations; LWS GEOS-FPIT.

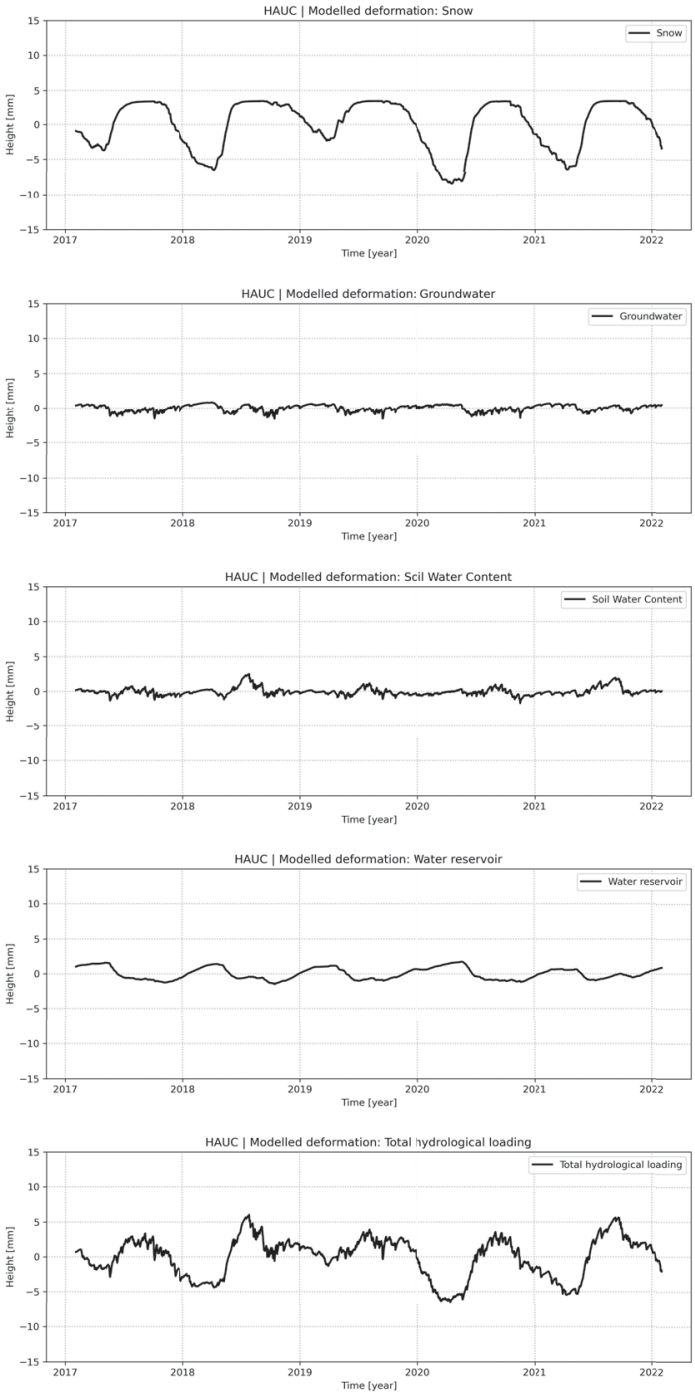

Figure B3: The graphs show the modelled deformation effects for HAUC from above: SWE, GWT, SMC, Water reservoir, and Total hydrological deformation.

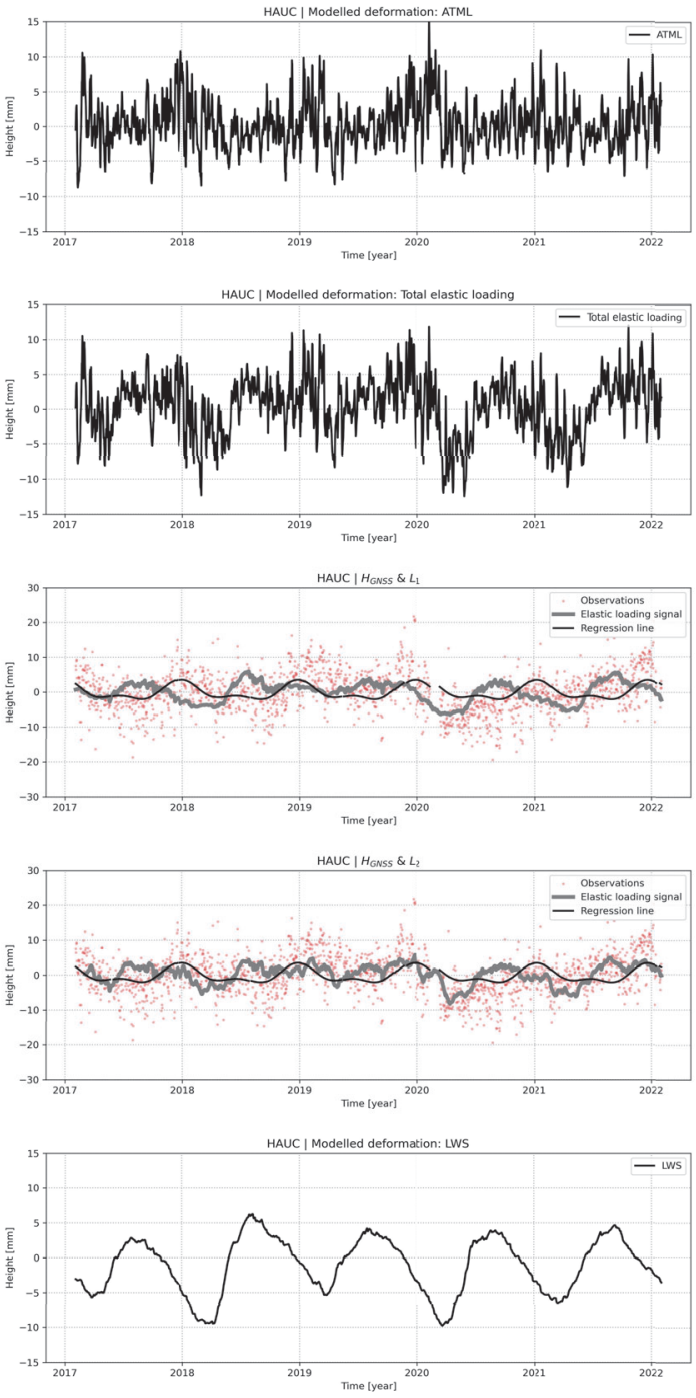

Figure B4: The graphs show the modelled deformation effects for HAUC from above: ATML; Total hydrological deformation + ATML; Total hydrological deformation together with GPS observations, and the regression line derived from the GPS observations; Total hydrological deformation + ATML together with GPS observations, and the regression line derived from the GPS observations; LWS GEOS-FPIT.

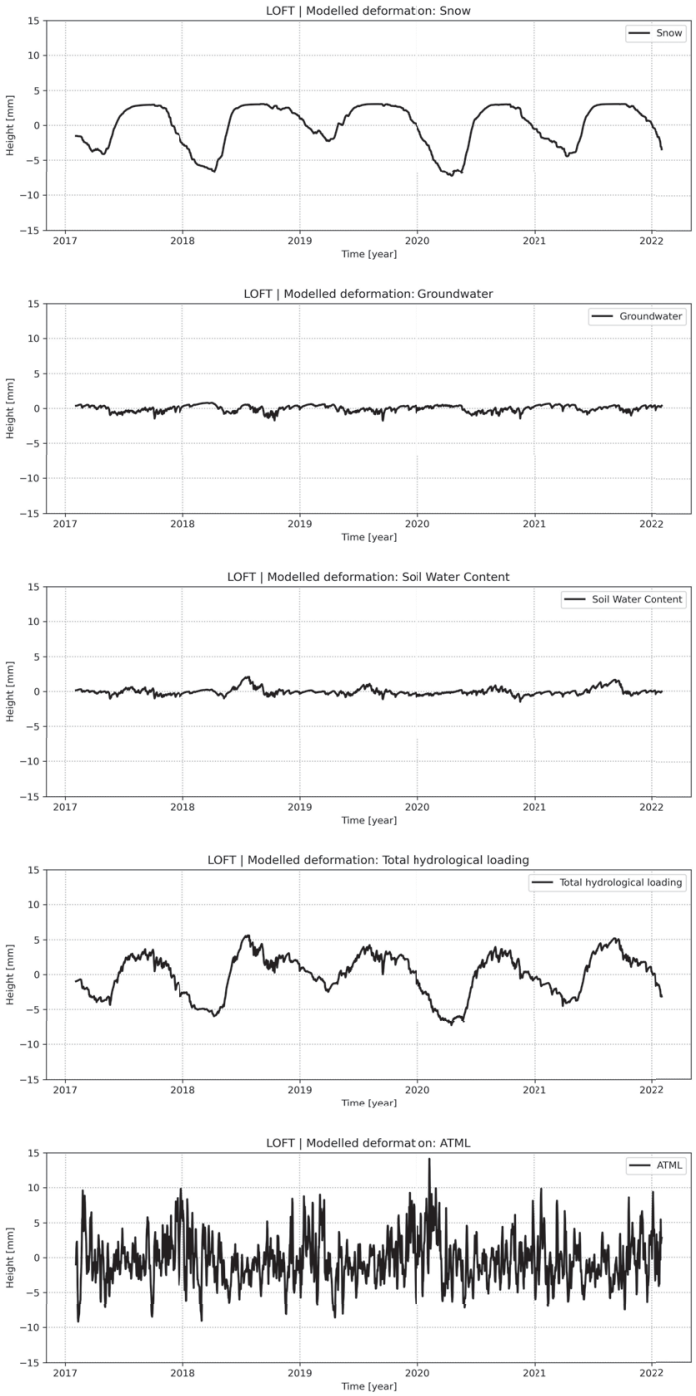

Figure B5: The graphs show the modelled deformation effects for LOFT from above: SWE, GWT, SMC, Total hydrological deformation, and ATML.

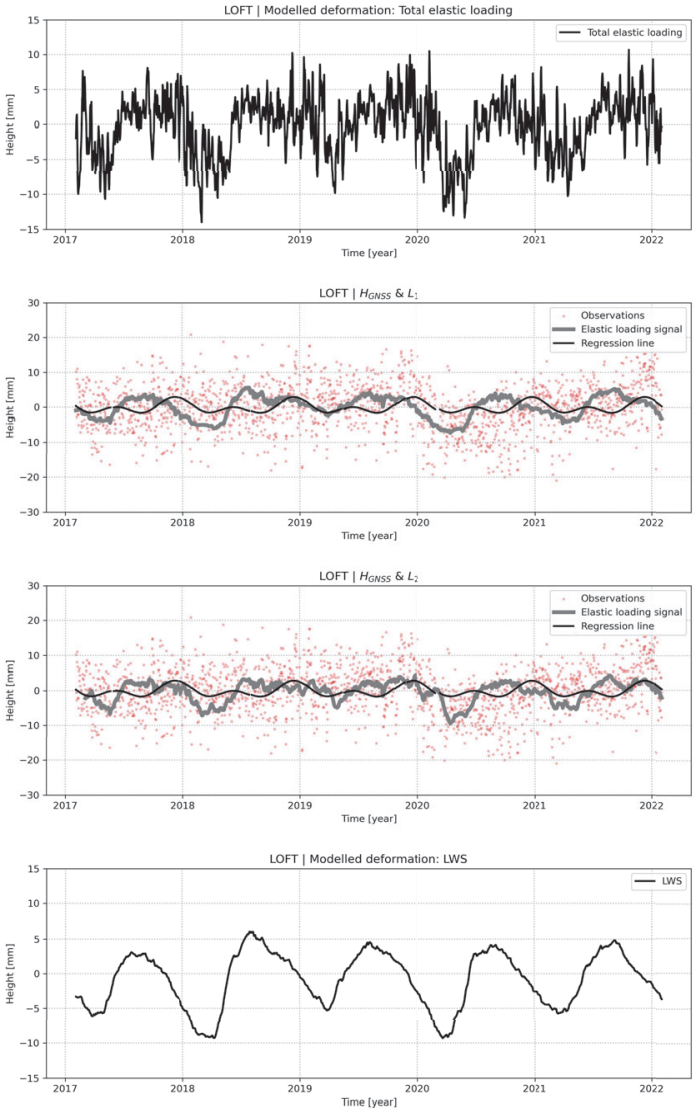

Figure B6: The graphs show the modelled deformation effects for LOFT from above: Total hydrological deformation + ATML; Total hydrological deformation together with GPS observations, and the regression line derived from the GPS observations; Total hydrological deformation + ATML together with GPS observations, and the regression line derived from the GPS observations; LWS GEOS-FPIT.

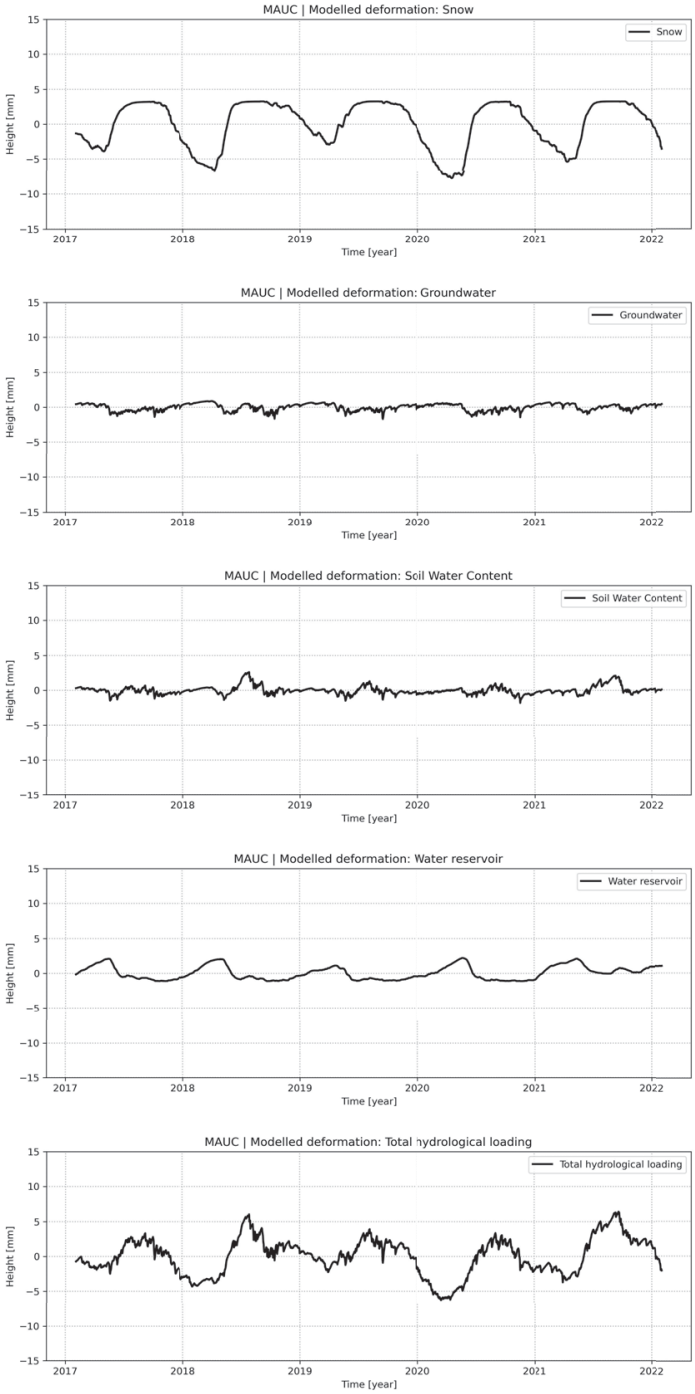

Figure B7: The graphs show the modelled deformation effects for MAUC from above: SWE, GWT, SMC, Water reservoir, and Total hydrological deformation.

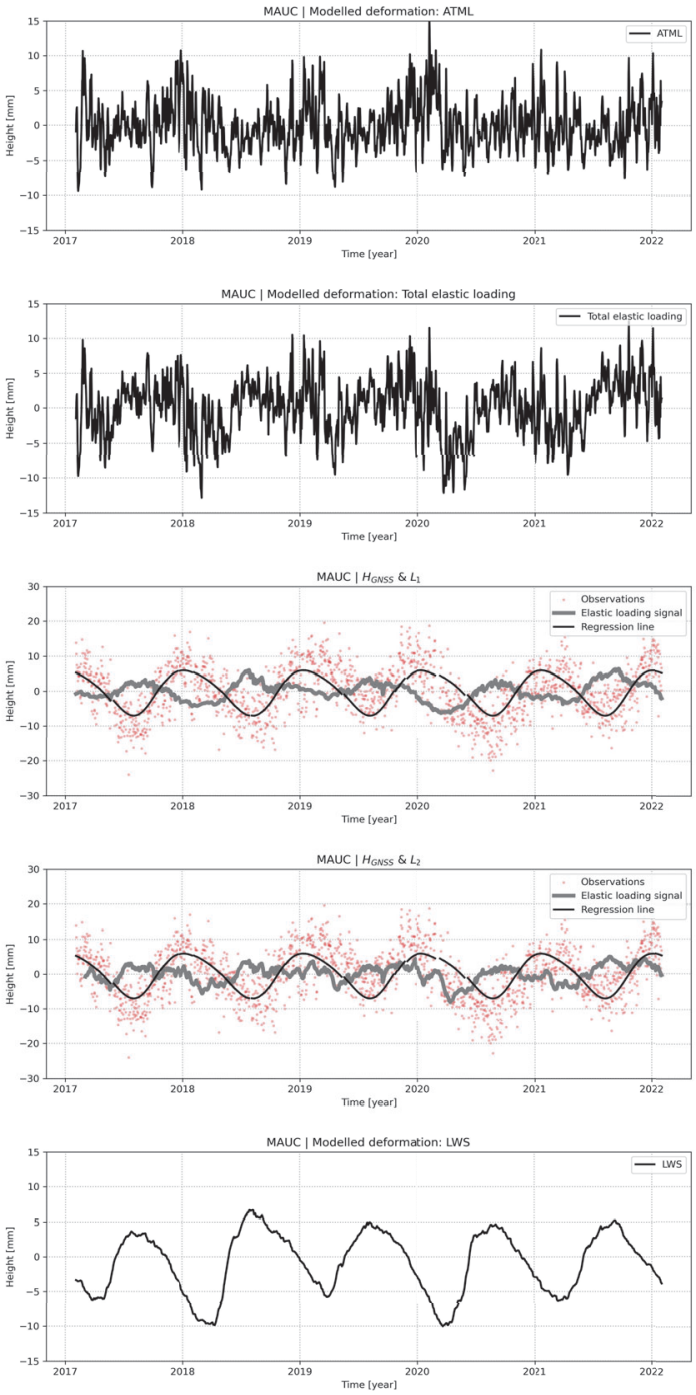

Figure B8: The graphs show the modelled deformation effects for MAUC from above: ATML; Total hydrological deformation + ATML; Total hydrological deformation together with GPS observations, and the regression line derived from the GPS observations; Total hydrological deformation + ATML together with GPS observations, and the regression line derived from the GPS observations; LWS GEOS-FPIT.

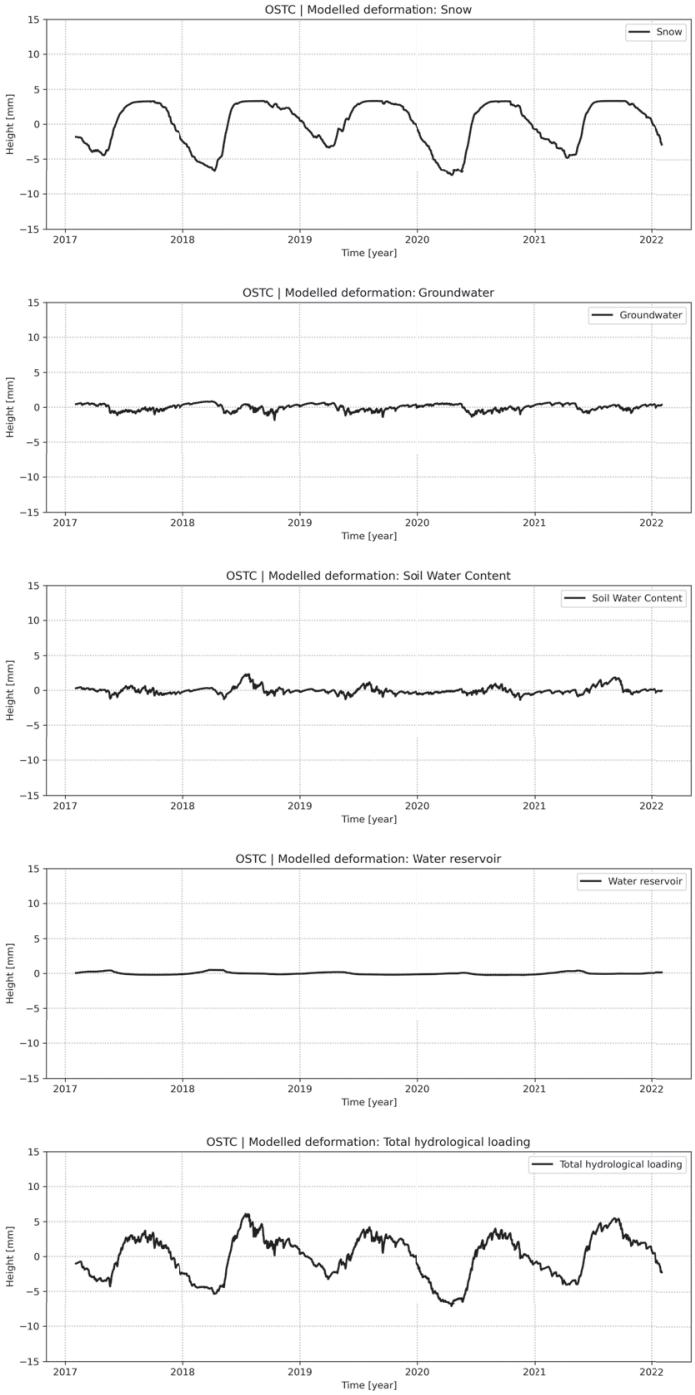

Figure B9: The graphs show the modelled deformation effects for OSTC from above: SWE, GWT, SMC, Water reservoir, and Total hydrological deformation.

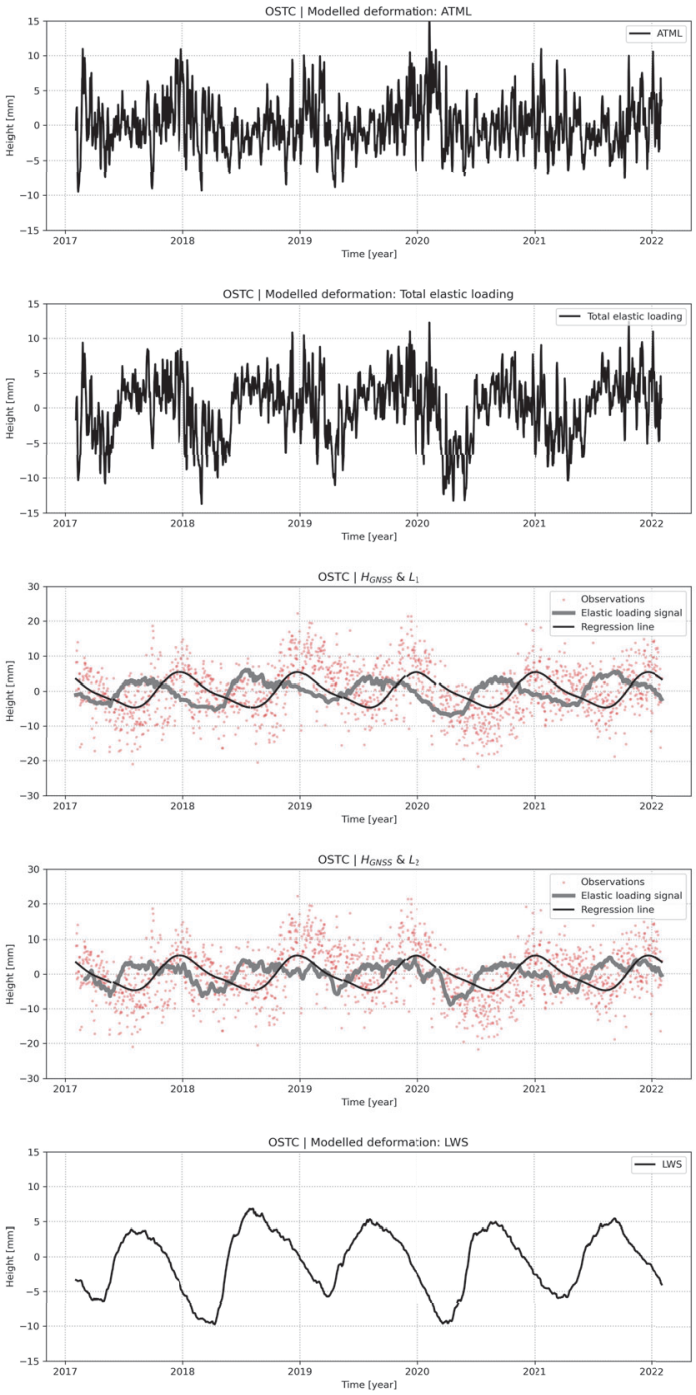

Figure B10: The graphs show the modelled deformation effects for OSTC from above: ATML; Total hydrological deformation + ATML; Total hydrological deformation together with GPS observations, and the regression line derived from the GPS observations; Total hydrological deformation + ATML together with GPS observations, and the regression line derived from the GPS observations; LWS GEOS-FPIT.

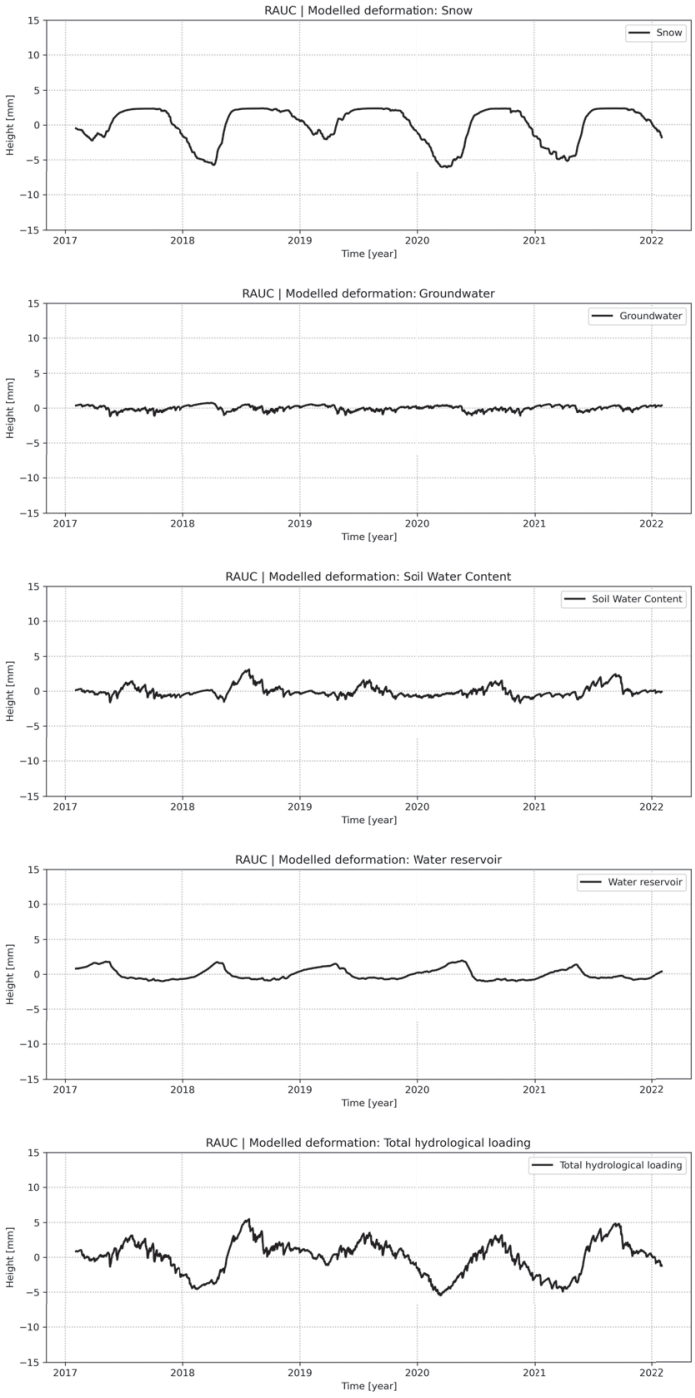

Figure B11: The graphs show the modelled deformation effects for RAUC from above: SWE, GWT, SMC, Water reservoir, and Total hydrological deformation.

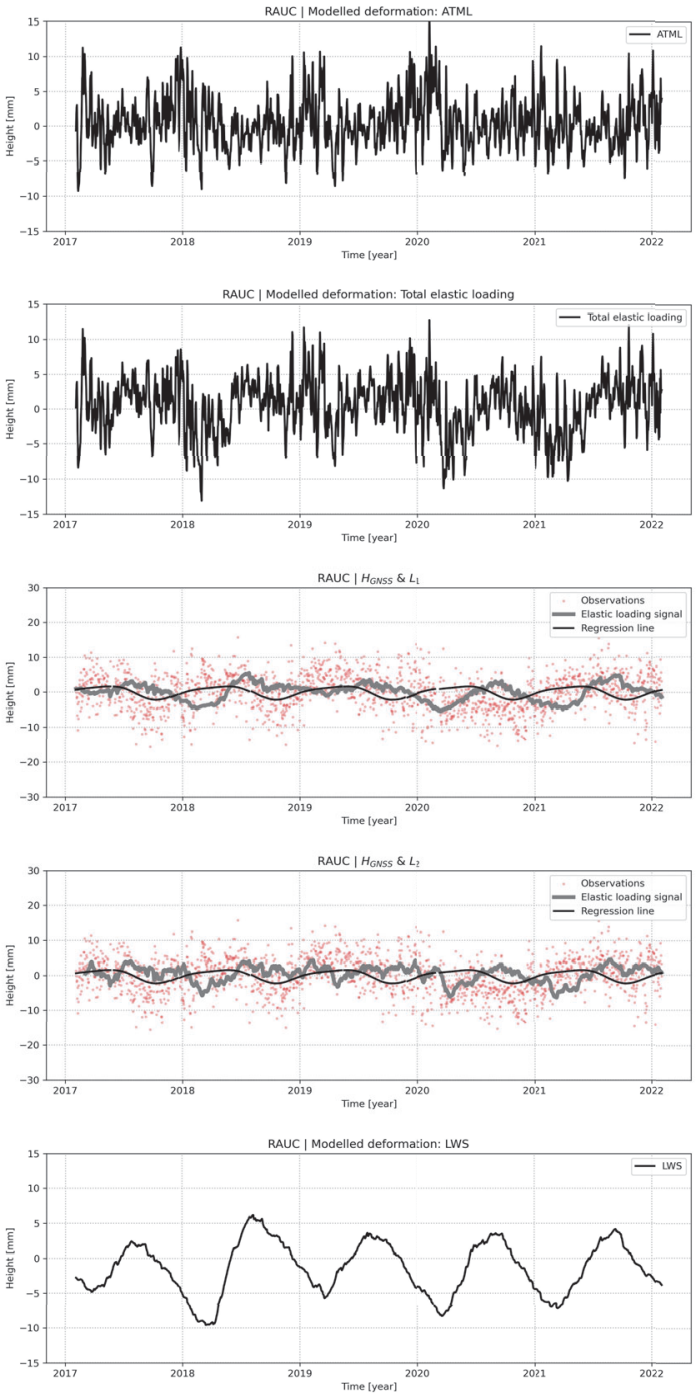

Figure B12: The graphs show the modelled deformation effects for RAUC from above: ATML; Total hydrological deformation + ATML; Total hydrological deformation together with GPS observations, and the regression line derived from the GPS observations; Total hydrological deformation + ATML together with GPS observations, and the regression line derived from the GPS observations; LWS GEOS-FPIT.

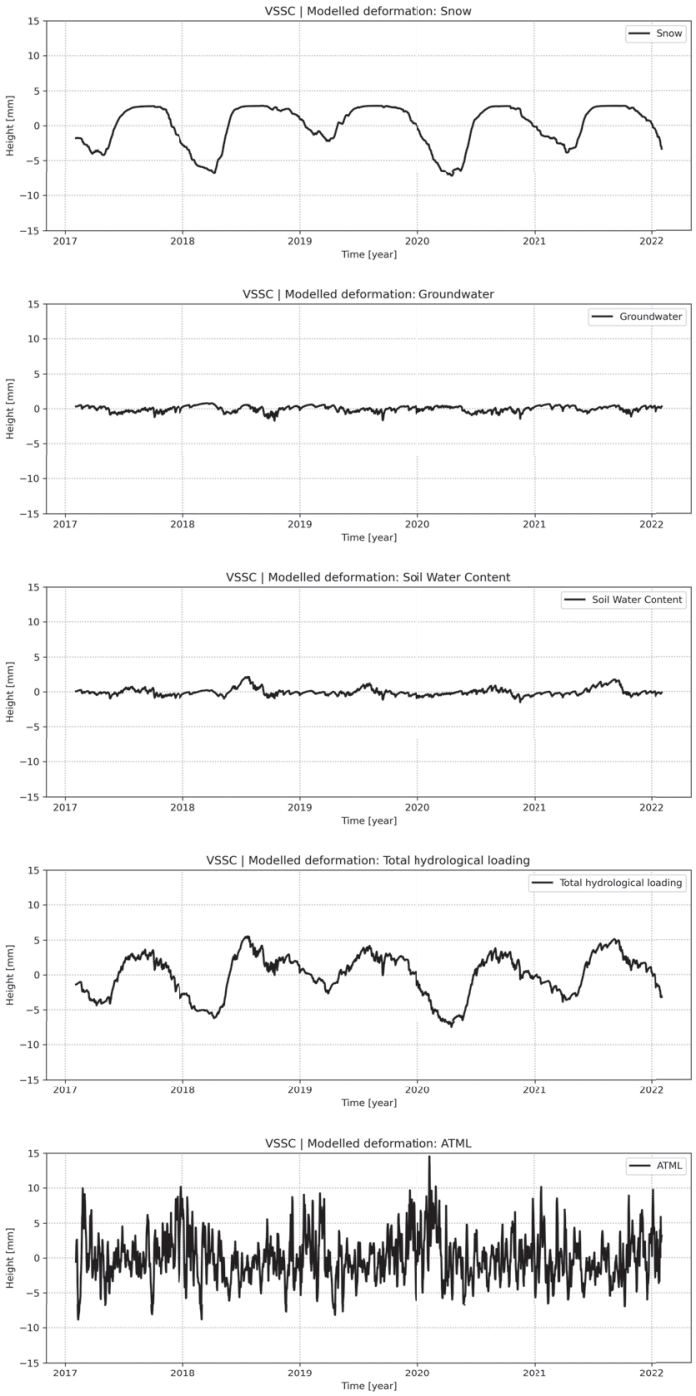

Figure B13: The graphs show the modelled deformation effects for VSSC from above: SWE, GWT, SMC, Total hydrological deformation, and ATML.

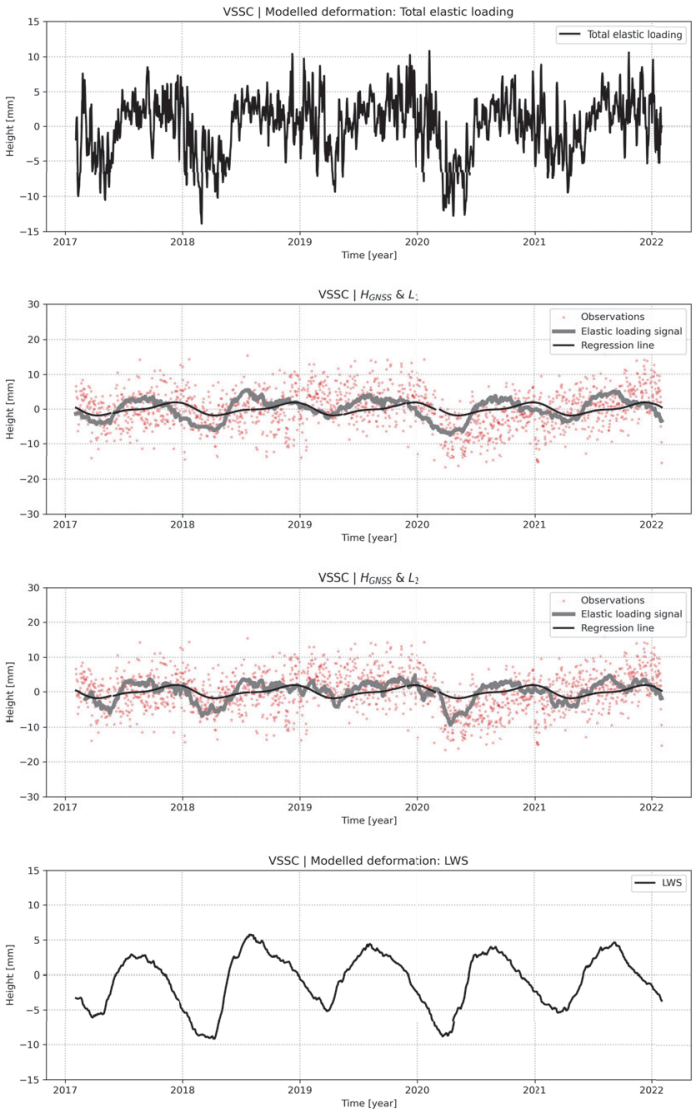

Figure B14: The graphs show the modelled deformation effects for DGLS from above: Total hydrological deformation + ATML; Total hydrological deformation together with GPS observations, and the regression line derived from the GPS observations; Total hydrological deformation + ATML together with GPS observations, and the regression line derived from the GPS observations; LWS GEOS-FPIT.

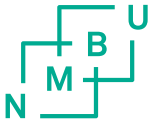

Norges miljø- og biovitenskapelige universitet
Noregs miljø- og biovitskapelege universitet
Norwegian University of Life Sciences

Postboks 5003
NO-1432 Ås
Norway